INFORMATION TO USERS

This manuscript has been reproduced from the microfilm master. UMI films the text directly from the original or copy submitted. Thus, some thesis and dissertation copies are in typewriter face, while others may be from any type of computer printer.

The quality of this reproduction is dependent upon the quality of the copy submitted. Broken or indistinct print, colored or poor quality illustrations and photographs, print bleedthrough, substandard margins, and improper alignment can adversely affect reproduction.

In the unlikely event that the author did not send UMI a complete manuscript and there are missing pages, these will be noted. Also, if unauthorized copyright material had to be removed, a note will indicate the deletion.

Oversize materials (e.g., maps, drawings, charts) are reproduced by sectioning the original, beginning at the upper left-hand corner and continuing from left to right in equal sections with small overlaps.

ProQuest Information and Learning
300 North Zeeb Road, Ann Arbor, MI 48106-1346 USA
800-521-0600

UMI®

Dissertation

Mesopause Region Thermal and Dynamical Studies Based on Simultaneous Temperature, Zonal and Meridional Wind Measurements with an Upgraded Sodium Fluorescence Lidar

Submitted by
James Patrick Sherman
Department of Physics

In partial fulfillment of the requirements
for the degree of Doctor of Philosophy
Colorado State University
Fort Collins, Colorado
Fall 2002

Colorado State University

July 25, 2002

WE HEREBY RECOMMEND THAT THE DISSERTATION PREPARED UNDER OUR SUPERVISION BY JAMES SHERMAN ENTITLED MESOPAUSE REGION THERMAL AND DYNAMICAL STUDIES BASED ON SIMULTANEOUS TEMPERATURE, ZONAL, AND MERIDIONAL WIND MEASUREMENTS WITH AN UPGRADED SODIUM FLUORESCENCE LIDAR BE ACCEPTED AS FULFILLING IN PART REQUIREMENTS FOR THE DEGREE OF DOCTOR OF PHILOSOPHY.

Committee on Graduate Work

Advisor

Co-Advisor

Department Head

Abstract

Mesopause Region Thermal and Dynamical Studies Based on Simultaneous Temperature, Zonal and Meridional Wind Measurements with an Upgraded Sodium Fluorescence Lidar

Continued hardware upgrades have permitted extension of the Colorado State University (CSU) lidar to a two-beam operation, capable of simultaneously measuring temperature, zonal winds, meridional winds, and sodium density in the mesopause region (80-105km) above Fort Collins, CO. A total of 172 hours of nightly observation and four campaigns over full diurnal (24-hour) cycles have been conducted in this two-beam configuration. The nighttime results, composed of 70 observation hours during the winter period of Jan 26-Feb 15, 2002 and 102 hours during the early summer period of May 22-June 12, 2002 are compared with temperature and wind climatology models and with data compiled from four decades of sparse wind measurements made by tracking metallic chemicals released by rockets (compiled by Larson, 2001). Large winter winds and shears and the resulting instabilities (in the Richardson sense) can be inferred from the data. These winds are larger than those predicted in models (Hedin, Roble) and are comparable to chemical release data (Larson). During the period May 22-June 12, the CSU lidar measured mesopause region temperatures, zonal winds, and meridional winds over four full diurnal cycles (the first such simultaneous measurements covering complete diurnal cycles). These measurements were part of a 232-hour campaign. Harmonic analysis was performed on the resulting temperature and wind measurements and the resulting

amplitudes and phases of the 12 and 24-hour oscillations were compared with those from the Global-Scale Wave Model (GWSM00) created (1995) and upgraded by Hagan.

James Sherman
Department of Physics
Colorado State University
Fort Collins, CO 80523
Fall, 2002

ACKNOWLEDGMENTS

Often it takes a step backward and some reflection before one gains a true appreciation of the contributions of others. I would like to thank my fellow CSU lidar group members, Phil Acott, Kam Arnold, Takuya Kawahara, Tao Li, Joe Vance, Biff Williams, Lifang Xu, and Titus Yuan. Your contributions helped make this thesis possible. I would also like to thank Loren Caldwell for reviving an old version of the laser-locking program. My advisor, Chiao-Yao She, has been not only an advisor but also a great example of dedication and humility, from whom I have learned much more than lidar. My co-advisor, David Krueger, whose endless energy and quest for detail I have grown to appreciate and hopefully emulate. I thank my committee members, John Harton, Steve Lundeen, Richard Johnson, and Wayne Schubert, for their helpful advice on how to make this thesis better. I thank my sons J.J and Nikolaus, for not complaining following the numerous empty promises to spend more time with them. Finally, I thank my wife Laura, for her endless support and patience during this long journey

TABLE OF CONTENTS

LIST OF FIGURES

List of Tables

Chapter 1-Introduction

1.1) Research Objectives

The mesopause region of the atmosphere is located approximately 80-110 km above the earth's surface, forming the boundary between the mesosphere and thermosphere (Fig. 1.1). The mesopause is the coldest region in the earth's atmosphere. It is also the most experimentally inaccessible region. The lack of past experimental data in the mesopause region prompted scientists to refer to it as the 'ignorosphere'.

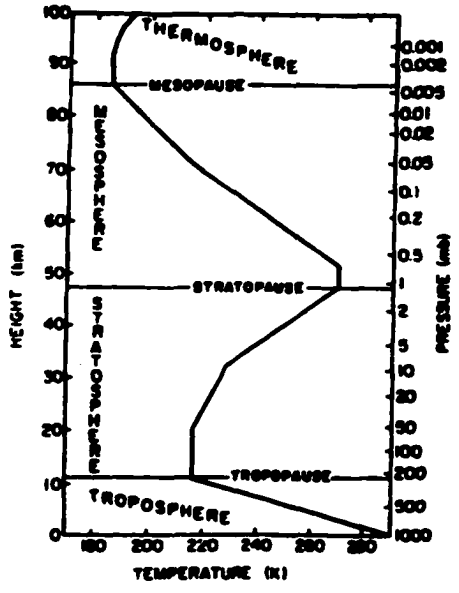

Figure 1.1 Mean mid-latitude vertical temperature structure of earth's atmosphere from 0-100km. (Hagan)

The Colorado State University (CSU) sodium fluorescence lidar has been measuring nightly temperatures and sodium (Na) densities in the mesopause region above Fort Collins, CO (40.5°N, 105°W) since 1989. These studies have provided to the geophysical community significant information (She, et. al 2000) on mesopause temperature climatology, as well as other interesting information concerning the region's counter-intuitive thermal structure. In 1994, a narrowband Faraday filter was developed (H. Chen, 1996) to reject intense solar background levels, extending measurement capability to include daylight hours. The lidar transmitter was upgraded in 1997 (White,

1999) to accurately measure one horizontal wind component. Continued hardware upgrades (discussed in chapters four and five) permitted the extension (January, 2002) to two-beam mode, capable of simultaneously measuring temperature, both horizontal wind components, and sodium density in the mesopause region (80-105km). Capabilities unique to the sodium fluorescence lidar (Fig. 1.2) permit the measurement of important geophysical parameters such as Brunt-Vaisala frequency, wind shears, and Richardson number (section 2.2).

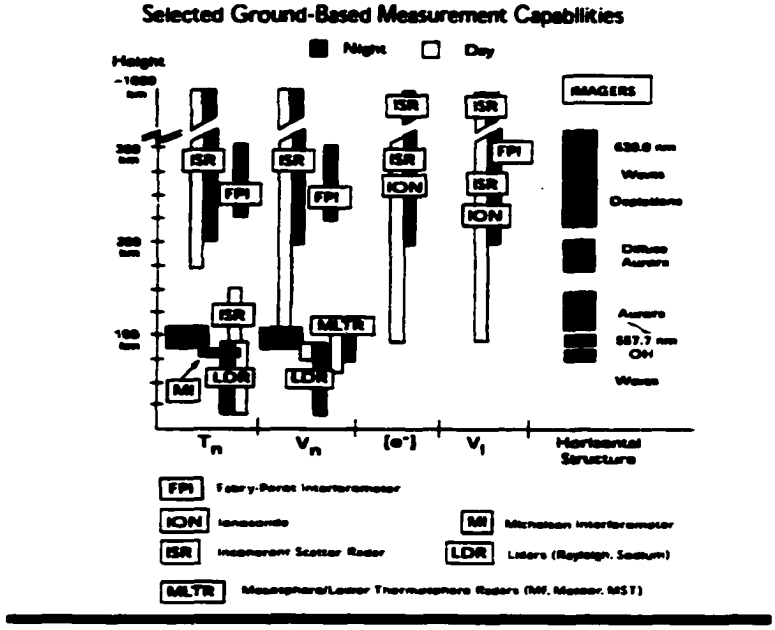

Figure 1.2 Altitude (vertical axis) and time (blue or white) coverage of ground-based instrumentation in the CEDAR (Coupling, Energetics, and Dynamics of Atmospheric Regions) database. The labels on the horizontal axis denote atmospheric parameters measured by the instruments: T_n (neutral temperatures), V_n (neutral winds), e^- (electron densities), and V_i (ion densities) (http://cedarweb.hao.ucar.edu/docs/CEDAR.pdf)

From these three quantities, static and dynamic stability of the mesopause region can be assessed. Preliminary studies have revealed the presence of large winds and shears (larger than predicted by models) in the winter mesopause region above Fort Collins. Results will be presented in sections 7.1-7.3 and compared with the TIME-GCM model (Roble, 1999) and with four decades of sparse wind measurements made by tracking metallic vapors released by rockets (Larson, 2001). Continued improvements in Faraday filter

stability (Yuan) have resulted (May, 2002) in simultaneous measurements of temperature and both horizontal wind components over full diurnal (24-hour) cycles. This has significance in the study of solar atmospheric tides (section 2.2), which along with planetary waves dominate global-scale dynamics of the mesopause region. Four diurnal cycles are included in a 232 hour data campaign, covering the period May 22-June 12, 2002. Results are discussed and compared to the Global-Scale Wave Model (Hagan, 1995) in section 7.4.

1.2) The Na Fluorescence Lidar Measurement

The CSU Na fluorescence lidar utilizes an abundance of sodium atoms in the mesopause region as a tracer. These atoms are produced by the steady influx of meteors into the earth's atmosphere. Meteors heat and burn when encountering the earth's atmosphere, leaving behind a trail of neutral Na atoms in the mesopause region. After the sodium atoms diffuse and mix with the background atmosphere, atomic densities of $10^9 - 10^{10}\,\text{atoms}/\text{m}^3$ are common. The concentration is highest at around 91km and is mostly contained between 85-100km. Concentration is also strongly temperature-dependent, with a maximum in November and a minimum in June. The Na D_2 transition possesses a large differential back-scattering cross-section ($9.6 \cdot 10^{-17}\,\text{m}^2/\text{sr}$ at 589.1nm), which is 14 orders of magnitude stronger than that for Rayleigh scattering, permitting mesopause region measurements using a modest lidar power-aperture product. (She, 1990) Narrowband laser light at 589.158 nm is resonantly-scattered by the Na atoms in the mesopause. The portion of light scattered directly backward (θ=180°) is collected by the lidar telescope, detected by a photomultiplier tube (PMT), counted, and then stored on a personal computer (PC) for later processing. Doppler-broadening of the induced fluorescence spectrum is used to obtain temperature data and Doppler-shift is used to determine line-of-sight (radial) winds. The lidar also measures Na density. Details of the lidar measurement and the conversion of Na fluorescence to mesopause region temperature and wind profiles will be the subject of chapters 3-6.

1.3) Introduction to the Mesopause Region

Due to improved instrumentation and the efforts of the geophysical community, considerable observational data in the mesopause region has been collected during the last 20 years. The data has revealed many interesting and unexpected results, including:

1) A strong coupling exists between lower and upper atmosphere. The regions are coupled by gravity (buoyancy) waves, tides, and planetary waves. Waves originate in the lower atmosphere and propagate upwards with increasing amplitude. Near the mesopause region, the waves often interact non-linearly with mean winds and with other waves, depositing energy and momentum in the upper atmosphere (Lindzen, 1981) and modifying the chemistry of the region. These waves dominate mesopause region climatology and are believed to be responsible for the mesopause temperature anomaly (Waltersheid, 1995), in which summer pole is much colder than winter pole. The physical details of these interactions are the subject of much current research.

2) The mesopause region is extremely sensitive to thermal, chemical, and dynamical forcing originating at lower levels, suggesting that this atmospheric regime may provide quantitative early evidence of atmospheric global change. An example of the region's sensitivity is revealed by models (Roble et. al, 1988), which suggest that a doubling of CO_2 and CH_4 can produce temperature reductions (due to CO_2 radiative cooling at 15μm) of 5-10°C in the mesosphere and 10-20°C in the lower thermosphere, as compared to less than 1°C changes near the earth's surface.

There also exists an inherent coupling between long-term thermal and dynamical changes in the mesopause region. Long-term thermal changes drive dynamical changes by altering vertical and horizontal temperature gradients and hence horizontal winds. (eq. 2.2.3) The resulting changes in mean circulation modify the filtering of gravity waves, whose momentum deposition strongly influences temperature structure (Lindzen, 1981). Due to strong thermal and dynamical coupling in the mesopause region, significantly more scientific information is obtained if temperatures and winds are simultaneously measured. Fluorescence lidar is the only ground-based instrument capable of simultaneous temperature and wind measurements over extended time periods in the region (Fig. 1.2).

Decades of observations at multiple locations (Fig. 1.3) are necessary to determine thermal and dynamical trends and to separate solar influences (She et.al, 2001) from anthropogenic influences and natural processes such as volcanoes (She, et. al, 1998). These observations must be conducted, to the extent possible, over full 24-hour cycles in order to separate tidal and mean-field components (chapter 2). NASA and NSF have launched an ambitious program, combining data from the TIMED (Thermosphere, Ionosphere, Mesosphere, Energetics and Dynamics) satellite (launched on December 7, 2001) with measurements from a globally-spaced chain of ground-based instruments (Fig. 1.3). The TIMED satellite employs spectrometers, radiometers, and a Doppler Fabry-Perot Interferometer to measure temperatures, winds, and densities (among other things) in the region 60-180km above earth's surface. The satellite conducts these measurements from a circular orbit 625km above earth, providing global-scale horizontal coverage. Ground-based instruments such as the CSU lidar complement satellite observation by providing excellent vertical resolution and local-time coverage, which is necessary for a complete study of solar migrating atmospheric tides.

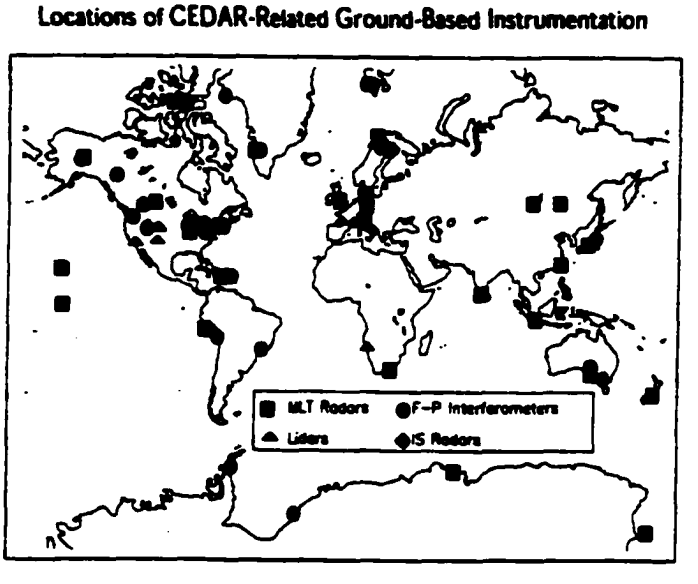

Figure 1.3 Geographical distribution of CEDAR ground-based instrumentation. (http://cedarweb.hao.ucar.edu/docs/CEDAR.pdf)

1.4) Thesis Structure

Chapter 2 discusses basic thermal and dynamical structure of the mesopause region in terms of a mean circulation and tidal perturbations. The emphasis will be on simple models and concepts, which will facilitate understanding of lidar data presented in chapter 7.

Chapter 3 introduces Na spectroscopy at frequencies near the D_2 transition used by the CSU Na fluorescence lidar. This spectroscopy is used to derive atmospheric parameters from returned fluorescence.

Chapter 4 provides an overview of the CSU lidar transmitter, receiver, and processing electronics.

Chapter 5 introduces lidar modifications leading to this thesis, which have resulted in simultaneous mesopause region temperature and vector wind profiles in the mesopause region over diurnal cycles.

Chapter 6 outlines the procedure used in the data analysis for converting returned fluorescence photon counts into temperature and wind profiles. Vertical and time profiles of temperature, zonal, and meridional winds are then presented.

Chapter 7 presents the results of four months of temperature and vector wind measurements in the mesopause region above Fort Collins, CO, beginning in January 2002. This data includes 172 nightly hours of nightly observation and four campaigns covering full diurnal (24-hour) cycles. Results will be compared to those deduced from four decades of rocket wind measurements and with global circulation and wave models.

Chapter 8 summarizes the current state of CSU lidar research and what lies ahead.

Appendix A details spectroscopy used to calibrate the Na lidar measurement. The calibration experiments include characterization of the laser pulse lineshape and cw spectroscopy used to determine the relative transmission function of the Faraday filter used in daytime lidar measurements and that of the iodine vapor cell used for correcting instrument-induced wind bias. Algorithms for the software used in these measurements are also presented.

Appendix B provides a table with the dates and UT hours of all data used in this dissertation.

Chapter 2-Thermal and Dynamical Structure of the Mesopause Region

This chapter presents an overview of the thermal and dynamical structure of the mesopause region. Simplified models will be used, whenever possible, to promote a qualitative understanding of the data obtained by the CSU Na fluorescence lidar. This data is presented in chapter 7. References are provided for more complete and authoritative accounts of the theory.

Some of the ways in which atmospheric data are represented, including notation used in this chapter and in chapter 7, are briefly touched upon in section 2.1. Basic accounts of zonal mean thermal and dynamical atmospheric structure will then be given in section 2.2. Perturbations to the mean mesopause structure are dominated by waves propagating upward from the lower atmosphere. Whether these waves propagate upward or are confined to the source region is determined by the stability of the atmospheric region with respect to small perturbations. Basic criteria for static and dynamic stability are presented in section 2.3. In section 2.4, a brief introduction to internal gravity waves will be given to facilitate a simple understanding of atmospheric tides, which are global scale internal gravity waves forced by periodic solar heating and modified by the earth's sphericity. Some basic parameters of atmospheric tides measurable by lidar and other ground-based instrumentation will be introduced.

2.1) Representation of Atmospheric Field Variables

Many representations exist which describe atmospheric field variables such as temperature, velocity, density, and pressure. Which representation is used depends on convenience and the phenomena under investigation. For example, it is conventional in describing upper atmospheric tides to express the field variable X (which can represent any atmospheric variable) by the sum of a zonal mean component and a disturbance component

$$X(\lambda,\varphi,z,t) = \overline{X}(\phi,z,t) + X'(\lambda,\phi,z,t) \qquad \text{(eq.2.1.1)}$$

where $\overline{X}$ is the zonal mean value, averaged over all longitudes. λ is longitude. ϕ is latitude, z is altitude, and t is time. The quantity X′ is the local deviation of the variable X from the zonal mean value.

Other representations will also be used to describe atmospheric variables in this thesis. Monthly and seasonal averages at a single location are often used. These averages can in turn be averaged over many years to obtain means for each month or season. This representation is used for long-term climatology studies. Another representation is harmonic analysis, which will be applied to tidal measurements over complete diurnal (24-hour) cycles.

A brief aside concerning notation is now in order. It is conventional in atmospheric science to use a coordinate system fixed with respect to the rotating earth. The unit vectors i,j,k are in the directions of increasing longitude (east), latitude (north), and altitude, respectively. The wind components in this coordinate system are zonal wind (given the symbol u), which is positive to the east, meridional wind (v), which is positive to the north, and vertical wind (w), which is positive in the direction of increasing altitude. The symbols ϕ and λ refer to latitudinal and longitudinal angle, respectively.

2.2) Zonal Mean Structure of the Atmosphere

2.2.1) Zonal Mean Thermal Structure

The global mean (averaged over all latitudes, longitudes, and seasons) vertical temperature distribution (Fig. 2.1(a)) can be approximated by radiative equilibrium models (Andrews, 1987). Temperature decreases with height in the troposphere due to IR emission by water vapor and clouds. It then increases in the stratosphere due to absorption of solar UV radiation by ozone. In the mesosphere, temperature again decreases due to substantially-reduced ozone concentrations, reaching a minimum at the mesopause. In the thermosphere, temperature increases sharply due to increased photo-ionization of atmospheric ozone and oxygen by solar XUV radiation

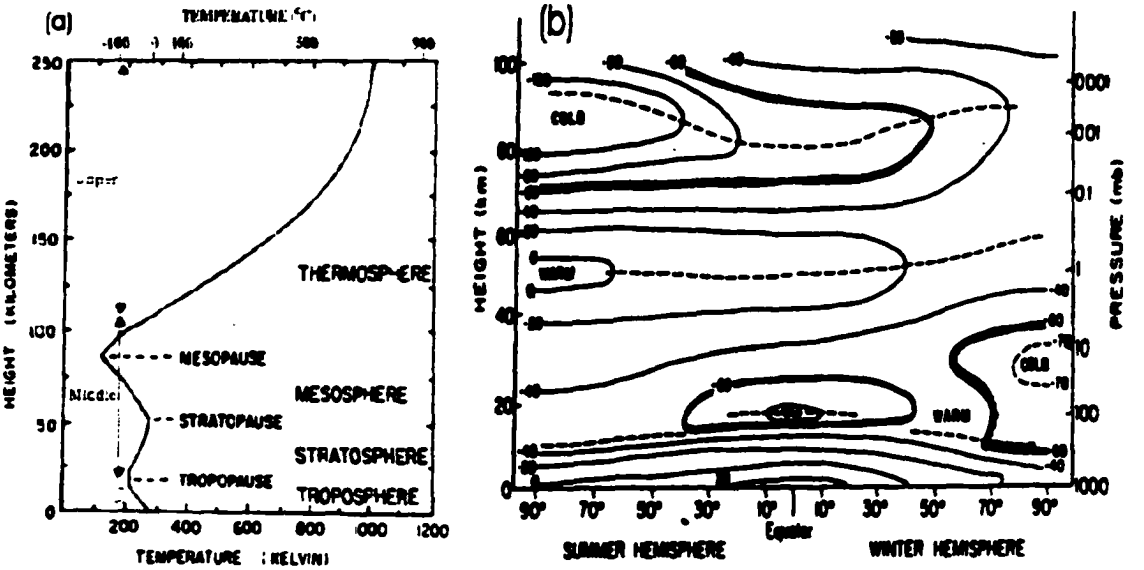

Figure 2.1 (a) Global mean T(z), in °C (top) and K (bottom), averaged over all months, latitudes, and longitudes. (b) Zonal mean $T(z, \phi)$, in °C, which is broken down into summer and winter seasons (reproduced from Andrews, 1987).

The zonal mean temperature distribution is formed by averaging over all longitudes at a given height z and latitude ϕ (Fig. 2.1b). This distribution is determined by the balance between net radiative heating (radiative heating-radiative cooling) and the dynamical heating and cooling produced by air motions, which transport energy and momentum. (Andrews, 1987). At solstice, maximum solar heating occurs at the summer pole, which receives 24 hours of sunlight. Minimum solar heating occurs at the winter pole, which receives no sunlight. At equinox, all latitudes receive 12 hours of sunlight. The equatorial region experiences more solar heating, however, due to the fact that the sun is directly overhead at this latitude. With the exception of the winter stratosphere and the summer and winter mesopause region, the zonal-mean temperature profile follows the net radiative heating distribution. It can be seen from Fig. 2.1(b) that the winter-latitude mesopause is much warmer than the summer-latitude mesopause. Thus, the thermal structure of the mesopause region must be dominated by dynamical, not radiative, processes. This, in fact, has been confirmed. Waves generated in the lower atmosphere propagate upward, increasing in amplitude until they break in the mesopause region, much like the breaking of water waves on an ocean beach. The breaking waves deposit

energy and momentum, altering the thermal structure of the mesosphere and lower thermosphere (Lindzen, 1981). This will be discussed in section 2.3.

2.2.2) Zonal Mean Dynamical Structure

Atmospheric motion can, in principle, be derived by applying Newton's 2nd Law to a parcel of air. An air parcel of unit mass moving with respect to the rotating earth experiences an acceleration

$$\frac{\overrightarrow{dV}}{dt} = \frac{-\nabla P}{\rho} - 2\vec{\Omega}\times\vec{V} + \vec{F}_{\text{friction}} + \vec{g} \qquad \text{(eq. 2.2.1)}$$

where P=pressure (Newtons/m^2)

ρ = mass density (kg/m^3)

Ω =rotation rate of the earth (7.3×10^{-5} rad/sec)

$\vec{F}_{\text{friction}}$ =combined effects of dissipative processes (Newtons/kg)

$\vec{g}$ = gravitational acceleration, incorporating the vertical component of the centrifugal force (m/s^2)

$\vec{V}$ =velocity of the air parcel (m/s)

Terms on the right-hand side of eq. 2.2.1 represent the pressure gradient force, Coriolis force, frictional forces, and gravity. It is shown (Holton, 1972) that to a very good approximation[1], earth's atmosphere is in hydrostatic balance. Pressure decreases with height in such a way that the vertical component of the pressure gradient force is balanced by gravity and no net vertical force exists in an equilibrium atmosphere. This assumption would not hold for small-scale frictional processes, which would disrupt local equilibrium. The small error is due to neglecting the vertical component of the Coriolis term. Vertical velocities for synoptic scale systems (systems with a horizontal extent $\geq 10^3$ km and vertical extent ≥ 10 km) are typically on the order of a few cm/s (Houghton, 1986). Thus, large-scale atmospheric motion for an atmosphere in hydrostatic equilibrium

[1] To one part in 10,000 for horizontal velocities on the order of 10m/s and vertical motions on the order of 1 cm/s

is largely horizontal. This is not meant to underestimate the importance of vertical motion, for it is the vertical atmospheric motion which transports energy and momentum between atmospheric layers and drives much of dynamic meteorology.

For the atmosphere in hydrostatic equilibrium, we focus on the horizontal velocity components. A common approximation applied to eq.2.2.1 for large scale flows is the geostrophic approximation. If dissipative processes are negligible, the steady-state velocity distribution is in geostrophic balance. This means that the horizontal component of the pressure gradient force is balanced by the Coriolis force. The geostrophic velocities (i.e mean winds) are given by (Holton, 1972)

$$u_g = \frac{-1}{f\rho}\cdot\left(\frac{\partial P}{a\partial\phi}\right)_z \qquad \text{(eq. 2.2.2)}$$

$$v_g = \frac{1}{f\rho}\cdot\left(\frac{\partial P}{a\cos(\phi)\partial\lambda}\right)_z$$

where u_g = zonal geostrophic velocity (positive to the east) (m/s)

v_g = meridional geostrophic velocity (positive to the north) (m/s)

a = radius of earth ($6.37\cdot10^6$ m)

$f=2\Omega\cdot\sin(\phi)$ is the Coriolis parameter (rad/s)

ϕ = latitude

λ = longitude

ρ = mass density of atmosphere (kg/m^3)

The subscript z means that the derivatives are evaluated at constant z.

By assuming an ideal gas in hydrostatic equilibrium, eq. 2.2.2 can be used to derive the thermal wind equations (Andrews, 1987)

$$\frac{\partial u_g}{\partial\zeta} = \frac{-R}{Hf}\cdot\left(\frac{\partial T}{a\partial\phi}\right)_\zeta \qquad \text{(eq. 2.2.3)}$$

$$\frac{\partial v_g}{\partial \zeta} = \frac{R}{Hf} \cdot \left(\frac{\partial T}{a\cos(\phi)\partial \lambda} \right)_\zeta$$

where

$\zeta = H \ln(\frac{P_0}{P})$ is a measure of altitude (km) in log-pressure coordinates[2]

T=temperature (K)

P =Pressure (N/m^2)

$P_0 = 1.01 \cdot 10^5 N/m^2$ = 1atm is the atmospheric pressure at earth's surface.

H=scale height of the atmosphere = $RT_0 / M_{atm} g$ is the increase in altitude necessary in an isothermal atmosphere necessary to reduce pressure by 1/e (H = 6km for T_0=200K, which is a typical mesopause region temperature)

M_{atm} =mean molecular weight of the atmosphere (0.0288 kg / mol for dry air)

R = universal gas constant = 8.3143 Joules / (mol•K)

g=acceleration due to gravity = $9.5 m/s^2$ at mesopause heights.

The thermal wind equations relate vertical (since changes in physical height are roughly equal to changes in log-pressure height at mesopause altitudes) shear of the geostrophic wind to horizontal temperature gradients. These equations (eq.2.2.3) can be integrated to yield horizontal velocity profiles $u_g(\zeta)$ and $v_g(\zeta)$, given the temperature profile and the horizontal wind components at a reference height.

The thermal wind equations show strong agreement with observed zonal-mean zonal winds from the tropopause up to around 80km for extra-tropical flows (Lieberman, 1999). They also reproduce many of the observed features of zonal-mean zonal circulation in the extra-tropical mesopause region, although quantitative agreement is poor (Lieberman, 1999). That approximate thermal wind balance holds from the

[2] ζ is a pseudo-height, whose changes are related to physical height changes dz by $d\zeta = (T_0/T)dz \sim dz$ for T approximately equal to reference temp T_0 (Schubert, 2002). From 80-100km, the difference in magnitude between z and ζ is < 5%(Andrews, 1987).

tropopause altitudes up to ~80km is not surprising. Dissipative forces are small in these regions so the mean flow is expected to be approximately geostrophic. Frictional forces are no longer negligible in the mesopause region due to turbulence generated by breaking gravity waves (more appropriately termed buoyancy waves). This turbulence acts as a drag on large-scale flow and makes the flow ageostrophic. The flow is ageostrophic at low latitudes because the Coriolis force approaches zero and thus can no longer balance the pressure gradient force. For simplicity and due to the extra-tropical location of the CSU lidar, geostrophic balance and the resulting thermal wind equations are believed to be valid.

Geostrophic balance may be violated on a time scale of the perturbation to mean flow if the Coriolis term in eq.2.2.1 is not large enough. Under this condition the acceleration (inertial) term is no longer negligible in comparison with the Coriolis and pressure gradient terms. Validity of the geostrophic approximation is often quantified by the Rossby number, defined as the ratio of the acceleration term in eq.2.2.1 to the Coriolis term.

$$Ro = \frac{\Delta u / \Delta t}{2\Omega u \sin(\phi)} \qquad \text{(eq. 2.2.4)}$$

where u is the zonal velocity (it can be replaced by v for meridional velocity). In principle, the pressure gradient force can be used in place of the Coriolis force (since they are of roughly equal magnitudes for geostrophic flow) but it is much more difficult to determine. A Rossby number much less than one indicates approximate geostrophic motion. Consider the example of a semi-diurnal tide (period=12 hours) of typical amplitude 15 m/s propagating through the mid-latitude mesopause region. At ϕ=45°, the Coriolis acceleration would be $1.5 \cdot 10^{-3} m/s^2$. The Rossby number for this motion is

$$Ro = \frac{30 m/s / 6 hours}{1.5 \cdot 10^{-3} m/s^2} = 0.92$$

This example shows that the acceleration term can have magnitudes as large as the Coriolis term, resulting in ageostrophic flow for the duration considered. The point of this example is that caution must be used when applying the geostrophic approximation.

especially when dealing with perturbations, whose velocities often change on a time-scale much shorter than that of the mean wind.

Now, let's use the geostrophic wind equation (eq.2.2.2) and resulting thermal wind equation (eq.2.2.3) to deduce some basic features of observed zonal-mean circulation. Pressure gradients result from variations in heating. Above the troposphere, the variations are primarily latitudinal. As a result, isobars are directed approximately along lines of latitude. At a given height, air will thus flow from latitudes of higher temperature toward latitudes of lower temperature. The Coriolis force deflects moving air to the right in the northern hemisphere and to the left in the southern hemisphere[3]. Eventually, geostrophic balance is achieved and motion is parallel to the isobars (Fig. 2.2). Since isobars are along lines of constant latitude, zonal mean meridional circulation is much less than zonal-mean zonal circulation.

Note from Fig. 2.2 that in the presence of frictional forces ($\bar{F}_{Drag} \neq 0$), the velocity is reduced. The drag force counteracts the Coriolis force so that the pressure gradient force is not balanced. Motion now has a component perpendicular to the isobars. The resulting motion is thus ageostrophic. These frictional forces, produced by gravity wave breaking in the mesopause region, produce a small meridional circulation from summer pole toward winter pole (Fig. 2.2). This circulation, and the resulting mass pile-up and compressional heating in winter polar regions (Fig. 2.2), is believed to cause the mesopause temperature anomaly, in which summer mesopause is much colder than winter mesopause (Lindzen, 1981). Some of these basic features are observed in the CSU lidar data and will be discussed in chapter 7.

[3] To help understand this, consider the example of an observer rolling a ball outward from the center of a rotating merry-go-round. The ball appears to curve to the right (left) for the case of counterclockwise (clockwise) rotation. For the case of the rotating earth, the sense of rotation is counterclockwise (clockwise) in the northern (southern) hemisphere.

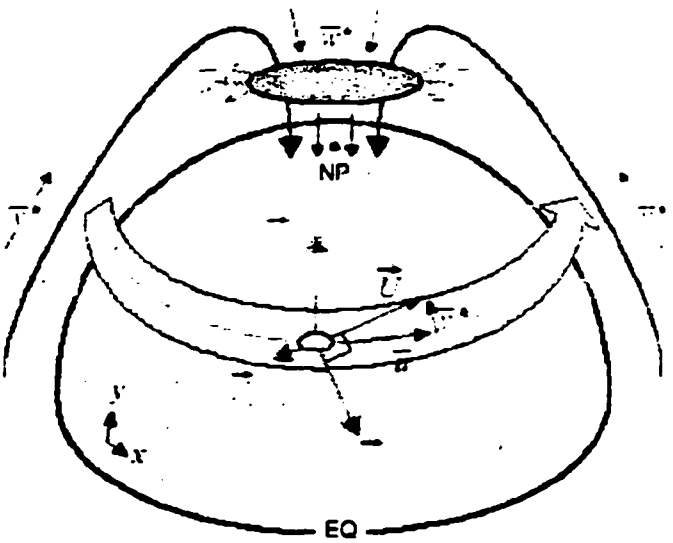

Figure 2.2 Forces on a moving air parcel. Meridional circulation near the north pole is shown for the case of winter in the northern hemisphere.

2.3) Atmospheric Stability

The standard method for deriving atmospheric stability criteria is to consider a parcel of air displaced by a small amount from its equilibrium position (a small perturbation). Will the perturbation be damped or will it grow to provide a mechanism for mixing and smoothing of wind and temperature profiles? Two types of atmospheric stability are static stability and dynamic stability, each of which will be outlined here.

2.3.1) Static Stability:

In this regime we neglect de-stabilizing wind shears. Consider an atmosphere at rest except for movement of an air parcel, (Dutton, 1986 p.70) displaced vertically from its equilibrium position by a small amount Δz. During the motion, the entropy of the parcel is assumed to be constant. Archimedes principle states that the net vertical force (buoyancy) acting on the parcel will be

$$F = (m_a - m_p)g \qquad \text{(eq. 2.3.1)}$$

where g=gravitational force per unit mass

m_p =mass of the parcel

m_a =mass of the displaced air

Invoking the conditions of an ideal gas in hydrostatic equilibrium results in the following differential equation

$$\frac{d^2}{dt^2}\Delta z + N^2 \cdot \Delta z = 0 \qquad \text{(eq. 2.3.2)}$$

where $N^2 = \frac{g}{T}\left(\frac{dT}{dz} + \frac{g}{c_p}\right) \equiv \frac{g}{T}\left(\frac{dT}{dz} + \Gamma_d\right)$ $rad^2/\sec^2$ is the square of the Brunt-Vaisala (or buoyancy) frequency (N~0.022rad/sec for T=200K and dT/dz=0)

T= temperature (K)

c_p =specific heat at constant pressure = 1005Joules / K•kg for earth's atmosphere (Houghton, 1986)

$\Gamma_d = \frac{g}{c_p}$ is the dry adiabatic lapse rate ~10K/km

For constant N, eq.2.3.2 is the harmonic oscillator equation. If $dT/dZ < -\Gamma_d$, then $N^2 < 0$ and Δz will grow without bound. The atmosphere is in this case statically unstable. Physically, this represents the case where an upwardly displaced parcel is less dense than its surroundings and will continue to rise. If $N^2 > 0$, the displaced parcel possesses a higher density than the surrounding air and will feel a restoring force. The atmosphere is then statically-stable. It is shown (Dutton, 1986 p.72) that the oscillation amplitude is proportional to 1/N so that greater stability implies smaller oscillations. A common example of this is air pollution associated with temperature inversions. The stable atmosphere prevents the pollution from rising to higher altitudes. Typical oscillation periods are 500 sec in the troposphere and 270-300 seconds in the mesopause region.

2.3.2 Dynamic Stability: Concept of Richardson Number

It is necessary to include the de-stabilizing effect of wind shears in establishing a criteria for dynamic stability. Dutton (1986, P.78) uses energy arguments to derive the Richardson number Ri, which is the measure of dynamic instability.

$$Ri = \frac{N^2}{\left(\frac{du}{dz}\right)^2 + \left(\frac{dv}{dz}\right)^2} = \frac{\frac{1}{T}\left(\frac{dT}{dz} + \frac{g}{c_p}\right)}{\left(\frac{du}{dz}\right)^2 + \left(\frac{dv}{dz}\right)^2} \qquad \text{(eq. 2.3.3)}$$

If Ri > 1/4, the atmosphere is dynamically-stable. If Ri < 1/4, the atmosphere can be unstable. This is a necessary but not sufficient condition for dynamic instability (Dutton, 1986). The Richardson number is thus a ratio of the stabilizing effect of buoyancy divided by the de-stabilizing effect of wind shears. The unique capability of the CSU lidar to simultaneously measure temperature and both horizontal wind components permits experimental probing of both static and dynamic stability conditions in the mesopause region. Long-term measurements can provide valuable insights into mesopause region instabilities and their influence on the dynamics of the region. Stability measurement results will be presented and discussed in chapter 7.

Summarizing this section, we note that static stability implies atmospheric ability to restore equilibrium against vertical motion while dynamic stability represents the ability to restore equilibrium against vertical shears of horizontal winds. Conditions often exist (chapter 7) where the atmosphere is dynamically unstable (Ri<1/4) but statically stable ($N^2 > 0$)

2.4) Atmospheric Waves

Atmospheric waves, usually forced in the lower atmosphere, propagate upward with increasing amplitude. The waves are observed as perturbations to atmospheric field variables (temperature, winds, pressure, density). They often reach maximum amplitudes

in the MLT (Mesosphere Lower Thermosphere) region, where they interact with each other and with the background atmosphere to significantly influence region meteorology. Atmospheric wave motions exist on a variety of temporal and spatial scales. Typical scales, along with common wave sources, are summarized in table 2.1.

Table 2.1 Typical scales and sources of atmospheric waves (Compiled from various sources, including Forbes, 1995)

Wave type	Typical Period	Typical Horizontal Scale	Common Sources
Gravity (buoyancy)	270sec-3hrs	10-1000km	Airflow over topography, Weather systems
Tidal	24 hrs (diurnal) 12 hrs (semi-diurnal) 8 hrs (terdiurnal) 6 hrs (quardiurnal)	global	Periodic solar absorption by Water vapor (troposphere), Ozone(stratosphere, mesosphere), Nitrogen and Oxygen (lower thermosphere)
Planetary	2,5,10,16 days (resonance modes)	global	Airflow over topography, Weather systems

Gravity waves propagate upward from the troposphere. In the absence of frictional forces, wave amplitudes increase exponentially with height to conserve energy[4]. Gravity waves are also affected by the mean wind distribution. Waves whose phase velocities are equal to the background wind velocity experience critical absorption (Fuller-Rowell, 1995). The mean wind thus acts as a filter in determining which gravity waves will continue propagating upward. Wave amplitudes can become large enough to force local temperature gradients to exceed the lapse rate (Fuller-Rowell, 1995), making the wave unstable (see section 2.3). This instability results in wave 'breaking', much like an ocean

[4] Similar to acoustic waves, atmospheric waves have kinetic energy density $U \sim \rho V^2$, where V is horizontal velocity. To conserve energy density, the amplitude varies as $V \sim \rho^{-1/2}$. Because atmospheric density varies on the order of exp(-z/H), velocities must grow exponentially with height in the absence of dissipative processes.

wave breaking on a beach. The breaking wave deposits energy and momentum, which accelerates the mean wind in the direction of the wave phase velocity (Lindzen, 1981). Since phase velocities of waves transmitted by the 'mean-wind filter' into the mesosphere are opposite the background wind (Fritts, 1995), a drag force is created. This drag force slows the mean wind and often reverses mean flow. It is believed to cause the mesopause seasonal temperature anomaly (Lindzen, 1981) discussed in section 2.1.

Tidal and planetary waves are global-scale waves, modified to account for motion with respect to the rotating spherical earth. Solar atmospheric tides are excited by periodic absorption of solar radiation by atmospheric molecules (Fig. 2.4(c)), connected with the apparent motion of the sun around the earth. Migrating tides have phases which propagate westward, synchronized with the diurnal (24-hour period) motion of the sun. The phases of non-migrating tides, as well as planetary waves, are not linked to the motion of the sun.

Solar atmospheric tides modulate the background temperature and wind fields at sub-harmonics of a solar day (table 2.1). The dominant components are the diurnal tide (24-hour period) and the semi-diurnal tide (12-hour period). Typical amplitudes of 10-20 m/s often exceed background wind amplitudes. Other harmonics (8-hour, 6-hour) do exist but are typically too small to be accurately measured. By modulating the background wind distribution, tides modulate filtering of gravity waves. This coupling is not yet understood and is the subject of much current research (Fritts, 1995). The remainder of this section will focus on basic tidal theory, with emphasis on quantities measurable with the CSU lidar. The goal is to provide sufficient theory to interpret experimental data. Before proceeding, it is important to note a subtle feature of atmospheric tidal measurements from a single location. With data from one station, we only evaluate local oscillations with periods of 24-hours/s (where s=1,2,3..) These oscillations typically contain contributions from migrating tides but can be contaminated by other local atmospheric variations of the same period. By comparing measured phases with those of calculated migrating tides, light can be shed as to the extent that observed oscillations are tidal in nature. While single-site tidal measurements are marginally useful, they are greatly

enhanced when combined with those measured simultaneously from other locations or from satellites. This approach is used in collaborative CEDAR/TIMED tidal studies. This subtle point will be further discussed in section 7.4.

2.4.1) Basic Tidal Theory

Theory presented follows the authoritative work of Forbes (1995). The interested reader is referred to this comprehensive treatment for greater detail. The dynamical equations governing atmospheric motion are non-linear with a variety of dissipative terms. These equations can only be solved numerically unless background wind distributions, meridional and zonal temperature gradients, and dissipative terms are neglected. Nevertheless, solving the simple equations provides insight into many tidal wave phenomena.

The method of perturbations is used to decompose atmospheric variables (wind components, temperature) into a zonal-mean state (averaged over longitude) and a perturbation component

$$(u, v, w, T) = (\overline{u}, \overline{v}, \overline{w}, \overline{T}) + (u', v', w', T') \qquad \text{(eq. 2.4.1)}$$

For tidal and planetary-wave motion, we assume the perturbations to be longitudinally-propagating waves of the form

$$(u', v', w', T') = (\hat{u}, \hat{v}, \hat{w}, \hat{T}) \exp(i(s\lambda - \sigma t)) \qquad \text{(eq.2.4.2)}$$

where s represents the zonal wavenumber, equal to the number of maxima of the sinusoidal oscillation in longitude, and σ represents the angular frequency of the oscillation. In the simplified case, separable solutions exist and the problem is thereby reduced to an eigenvalue problem. Forbes converts the resulting differential equation to dimensionless form, with solutions for the horizontal winds given by

$$\hat{u}(\phi, z) = \frac{\sigma}{4\Omega^2 a} \sum_n U_n(\phi) G_n(z) \qquad \text{(eq. 2.4.3)}$$

$$\hat{v}(\phi, z) = \frac{-i\sigma}{4\Omega^2 a} \sum_n U_n(\phi) G_n(z)$$

where $U_n(\phi) = \left(\frac{1}{f^2 - \sin^2(\phi)}\right)\left(\frac{s}{\cos(\phi)} + \frac{\sin(\phi)}{f}\frac{d}{d\phi}\right)\Theta_n(\phi)$

$V_n(\phi) = \left(\frac{1}{f^2 - \sin^2(\phi)}\right)\left(\frac{s \cdot \tan(\phi)}{f} + \frac{d}{d\phi}\right)\Theta_n(\phi)$

$\Theta_n(\phi)$ are Hough functions, which are solutions to LaPlace's Tidal eq.

a = radius of earth

Ω =angular rotation rate of the earth

$f = \sigma / 2\Omega$

and LaPlace's tidal equation is of the form (for a given s)

$$\frac{d}{d\mu}\left[\frac{(1-\mu^2)}{(f^2-\mu^2)}\frac{d\Theta_n}{d\mu}\right] - \frac{1}{f^2-\mu^2}\left[\frac{-s}{f}\frac{(f^2+\mu^2)}{(f^2-\mu^2)} + \frac{s^2}{1-\mu^2}\right]\Theta_n + \left(\frac{(2\Omega a)^2}{gh_n}\right)\Theta_n = 0$$

where $\mu = \sin(\phi)$ (eq.2.4.4)

h_n are the eigenvalues (unit: meters), referred to as atmospheric equivalent depths (for historical reasons)

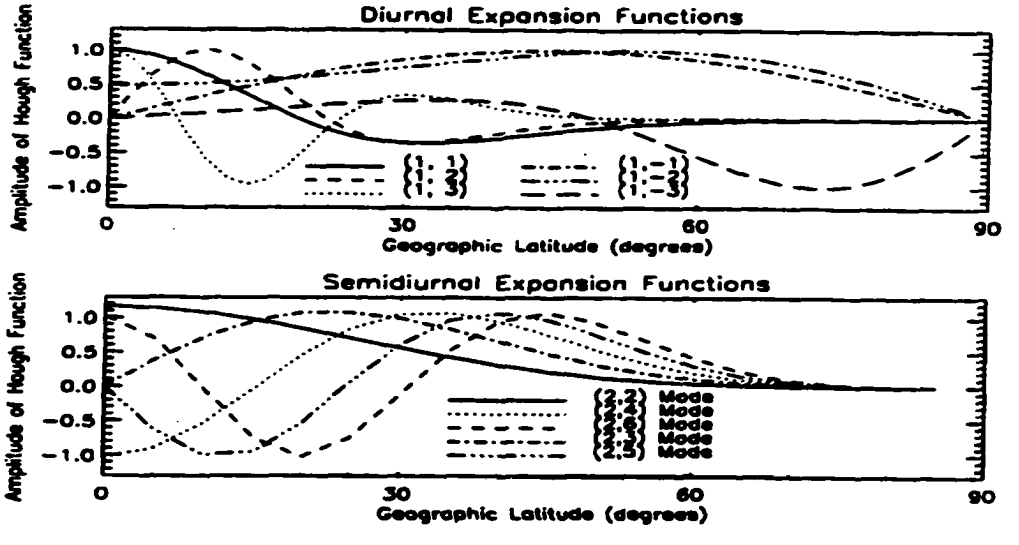

Figure 2.3 Expansion functions (Hough functions) for the diurnal and semi-diurnal tides as a function of latitude ϕ. Each (s, n) pair constitutes a mode. The designation s refers to the number of sinusoidal maxima with longitude (s=1 for diurnal tide and s=2 for semi-diurnal tide). The designation n refers to the number of latitudinal nodes of the Hough function for the mode (s,n) (Forbes, 1995).

The Hough functions form a complete, orthogonal basis set of solutions over ϕ and satisfy the requirement of boundedness at the poles. They are shown in Fig. 2.3 for the prevalent diurnal (s=1, $\sigma = 2\pi/24$ hours) and semi-diurnal (s=2, $\sigma = 2\pi/12$ hours) tides. Each Hough mode is associated with a vertical structure[5]

$$G_n(z) \sim \exp(z/2H)\exp(i\alpha_n z) \qquad \text{(eq.2.4.5a)}$$

and vertical wavelength

$$\lambda_{z,n} = \frac{2\pi}{\alpha_n} = \frac{2\pi}{\sqrt{\left(\frac{N^2}{gh_n}\right) - \frac{1}{4H^2}}} \qquad \text{(eq.2.4.5b)}$$

where h_n are the eigenvalues, referred to as the equivalent atmospheric depths (see eq.2.4.4 and table 2.2))

H = atmospheric scale height (see eq.2.2.3)

$N^2 = \frac{g}{T}\left(\frac{dT}{dz} + \frac{g}{c_p}\right) \equiv \frac{g}{T}\left(\frac{dT}{dz} + \Gamma_d\right)$ =Square of Brunt-Vaisala Frequency (see eq.2.3.2)

It can be seen (from combining eq.2.4.2, eq2.4.3, and eq.2.4.5a) that modes with $\alpha_n^2 > 0$ consist of waves propagating upward from the source with increasing amplitude

$$G_n(z) \sim \exp(z/2H) \cdot \exp(i(s\lambda + \alpha_n z - \sigma t)) \qquad \text{(eq. 2.4.6)}$$

Vertical wavelengths (eq.2.4.5(b)) can be significantly altered by temperature gradients (which change the value of N^2), often causing lower-order modes with longer wavelengths to become evanescent in the mesopause region while modes with shorter wavelengths continue to propagate upward, amplified, into the lower thermosphere. These wavelengths change seasonally and and irregularly as a result of dissipative

[5] The positive root of α_n is chosen for westward-propagating waves in order to satisfy the radiation condition (Forbes, 1995) that the vertical component of group velocity is positive as $z \to \infty$.

processes which alter local temperature gradients. Vertical wavelengths for an isothermal atmosphere ($\frac{dT}{dz}=0$) for diurnal and semi-diurnal modes are given in table 2.2.

Table 2.2: Prominent tidal modes, with vertical wavelength values given for an isothermal atmosphere at T=256K. The symmetry refers to whether the Hough function for that mode is symmetric or asymmetric with respect to the equator. Propagating modes have $\alpha_n^2>0$. Trapped modes have $\alpha_n^2<0$ and are evanescent. The indices s and n refer to the number of longitudinal maxima and the number of latitudinal nodes, respectively. (Forbes, 1995)

Wave	(s,n)	$h_n(km)$	$\lambda_z(km)$	Additional Descriptors
Diurnal tide	(1,1)	0.6909	27.9	1st symmetric propagating
Diurnal tide	(1,2)	0.2384	15.9	1st asymmetric propagating
Diurnal tide	(1,3)	0.1203	11.2	2nd symmetric propagating
Diurnal tide	(1,-1)	803.356		1st asymmetric trapped
Diurnal tide	(1,-2)	-12.2703		1st symmetric trapped
Diurnal tide	(1,-3)	-1.7581		2nd asymmetric trapped
Semidiurnal tide	(2,2)	7.8519	311.0	1st symmetric propagating
Semidiurnal tide	(2,3)	3.6665	81.4	1st asymmetric propagating
Semidiurnal tide	(2,4)	2.1098	53.8	2nd symmetric propagating
Semidiurnal tide	(2,5)	1.3671	41.0	2nd asymmetric propagating
Semidiurnal tide	(2,6)	0.9565	33.4	3rd symmetric propagating

Thus, for each value of σ (diurnal, semi-diurnal, etc), and s, a family of solutions exists. Each solution is denoted by n and possesses eigenvalue h_n. The atmospheric response to forcing at frequency σ is a linear superposition of these modes. Each mode is usually referenced as (s, n), where n is the number of meridional nodes of the mode (Fig. 2.3). All diurnal tidal modes have s=1 and all semi-diurnal tides have s=2. Negative indices for n indicate modes trapped near the height of excitation $\alpha_n^2<0$. Positive indices for n indicate propagating modes. Since the Hough functions form a complete, orthogonal basis set over ϕ, the thermal forcing J (heating per unit mass) at frequency σ can also be expanded in this basis as

$$J^{\sigma}(\varphi,z)=\sum_{n}\Theta_{n,s}(\phi)J_{n}(z) \qquad \text{(eq. 2.4.7)}$$

The heating depends on ϕ due to the influence of solar angle from zenith, which depends on latitude. Latitude and altitude dependence also arises from the variable distribution of O_3 and H_2O in the atmosphere. Longitudinal dependence, which accounts for non-migrating tidal contributions, is smaller and may be included in numerical models. Most of the atmospheric heating is coupled into the modes (Figs. 2.3 and 2.4(b)) which best overlap the latitudinal heating distribution. For diurnal tides, the (1,1) propagating mode receives the greatest thermal input while the (2,2) propagating mode receives the greatest input of all semi-diurnal modes. This is due to maximum amplitudes of these modes at low latitudes, where solar forcing is on average highest. Overlap varies with season as the solar angle varies.

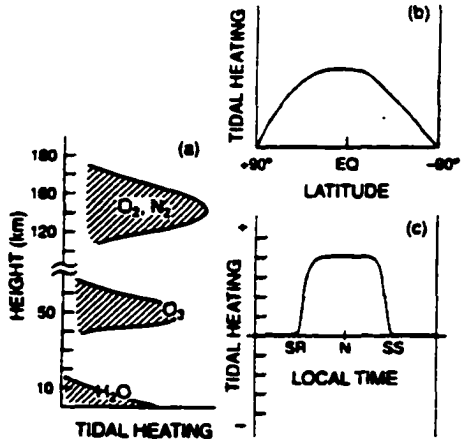

Figure 2.4 Tidal heating (thermal forcing) as a function of altitude (with rough distributions of absorbing molecules) (a), latitude (b), and local time (c). The symbols SR and SS in (c) refer to sunrise and sunset, respectively. (From Forbes, 1995)

More complete atmospheric models include mean-wind distributions, latitudinal and longitudinal temperature gradients, and dissipative processes. The equations of motion are no longer separable into latitude and altitude parts and numerical approaches must be invoked. One consequence of inseparability is mode-coupling. In this context, mode-coupling refers to the generation of tidal modes which are not forced directly by thermal excitation, but which arise due to the inseparability of the governing equations. One example is the semi-diurnal tide. Most of the heating goes into the (2,2) mode. Through

interactions of this mode with the mean atmosphere, the (2,2) mode is coupled to the (2,4) mode, enhancing the response of this mode. Mean-wind interactions reduce the amplitude of the (2,3) mode response. For the case of the diurnal tide, coupling of the dominant (1,1) propagating mode with trapped modes gives rise to latitudinal broadening of the response, which introduces some diurnal characterization into higher latitude temperature and wind profiles.

2.4.2) Implications of the Theory:

It can be seen from Fig. 2.3 that diurnal propagating modes (n>0) have amplitudes concentrated at low latitudes and that trapped modes (n<0) have amplitudes concentrated at higher latitudes. Because the mesopause region has few absorbing molecules to excite (Fig. 2.4(a)), propagating diurnal tides exert the most influence at latitudes less than 30°. Expansion functions for propagating semi-diurnal modes, on the other hand, have large amplitudes between 30-60° latitudes, becoming more concentrated at higher latitudes with increasing mode number n. This explains why temperature and wind measurements at latitudes greater than 30° are primarily semi-diurnal in character.

It is necessary when analyzing experimental data to investigate the tidal phase structures. We wish to determine how the phase of westward-propagating tides varies with height and longitude. From eq. 2.4.6, the points of constant phase are given by

$$s\lambda + \alpha z - \sigma t = C' \qquad \text{(eq. 2.4.8)}$$

where C' is a constant. Recall that $\alpha > 0$ and $\sigma < 0$ for migrating (westward-propagating) tides. At a fixed longitude λ, we see that

$$z(t) = \frac{\sigma}{\alpha} t + C'' \qquad \text{(eq. 2.4.9)}$$

Migrating tidal phases propagate downward with time. It is shown (Forbes, 1995) that upward energy propagation, which is consistent with a wave source at lower altitude, implies downward phase progression. The slope of lines of constant phase thus indicates

whether the source is above or below the mesopause. The slope is also used to estimate the vertical wavelength, viz

$$v_{phase,z} = \frac{\sigma}{\alpha} = \frac{2\pi/T}{2\pi/\lambda_z} = \frac{\lambda_z}{T}, \qquad \text{(eq. 2.4.10)}$$

where T=24hours/N (N=1,2...)

To see how the phase progresses with longitude, we hold t fixed in equation 2.4.8. This results in

$$z(\lambda) = \frac{-\alpha}{s} \cdot \lambda + C'' \qquad \text{(eq. 2.4.11)}$$

The contours of constant phase thus tilt backward with increasing height as λ is increased.

Ground-based tidal measurements are used in conjunction with satellite coverage. Satellite observations provide excellent horizontal coverage to determine zonal wavenumbers and horizontal phase velocities. These measurements do not, however, provide good local-time coverage. Lidar measurements provide excellent temporal and vertical coverage and are used to obtain temporal and vertical phase structure. A single lidar, however, provides no horizontal coverage. When used together, these measurements can provide significant information on the propagation characteristics of tides and other atmospheric waves.

Chapter 3 - Basic Theory of the Sodium Fluorescence Lidar Temperature/Wind Measurement

The basic lidar principle is simple. Laser pulses are directed upward into the atmosphere, where they interact with molecules of interest and are scattered. Details of this interaction define the type of lidar. The portion of light scattered directly backward is collected by a telescope. Collected photons are converted to electrical pulses and then sorted into range bins based on the round-trip transit time of the scattered photons. This provides high-resolution altitude profiles of the scattered photon counts. Light back-scattered from molecules at altitude z will return at time t=2z/c, relative to the emission of the laser pulse. In order to reduce statistical noise, all photons scattered from the pre-determined height interval $z_1 \le z \le z_2$ are counted and stored in a range bin of size $\Delta z = \frac{c}{2}(t_2 - t_1)$, where c is the speed of light. Vertical profiles thus have range resolution Δz. The properties of the back-scattered light provide information about the scattering molecules, including concentration, temperature, pressure, and velocity. Information so obtained depends on the type of lidar used and assumptions of the problem in question.

Sodium (Na) fluorescence lidar utilizes the abundance of neutral Na atoms ($(10^9 - 10^{10})/m^3$) deposited in the mesopause region by the ablation of meteors entering earth's atmosphere. The narrowband transmitter is tuned to selected frequencies in the thermally-broadened Na D_2 transition. Photons are resonantly absorbed by the Na atoms and are spontaneously re-radiated. This process is called laser-induced fluorescence, or resonant scattering. Spectral properties of the backscattered photons are strongly dependent on temperature and collective velocity of the Na atoms (wind). This chapter discusses the fluorescence spectra of Na atoms probed by a narrow-bandwidth laser and how the induced fluorescence is used to obtain high-resolution vertical profiles of temperature and winds in the mesopause region.

3.1) Basic Principles of the Temperature and Wind Measurements

Consider sodium atoms in a dilute gas of atmosphere. (Atmospheric pressure in the mesopause region is on the order of 0.01mB). In the laboratory reference frame, a given atom will have a velocity

$$\vec{V} = \vec{V}_{wind} + \vec{V}_T \qquad \text{(eq.3.1.1)}$$

where $\vec{V}_{wind}$ represents collective velocity of the gas (wind) and $\vec{V}_T$ is the thermal velocity of the atom with respect to the gases' center of mass. For simplicity, I will present the basic theory of fluorescence lidar temperature and wind measurements for a generic atomic system with two energy levels, E_0 and E_1, and a single resonance frequency $\nu_0 = (E_1 - E_0)/h$, where h is Planck's constant. Consider the one-dimensional case of motion along the axis of the upward-propagating laser beam. In this case, velocities in eq.3.1.1 are really line-of-sight velocities. Consider first the case of a monochromatic laser beam of frequency ν incident upon a gas with $\vec{V}_{wind}$=0. An atom moving with velocity V along the beam axis can only absorb a photon if the Doppler-shifted photon frequency is equal to its resonance frequency ν_0:

$$\nu = \nu_0 + V/\lambda_0 \qquad \text{(eq.3.1.2)}$$

where $\lambda_0 = c/\nu_0$. By convention, V is positive if the atom is moving away from the laser beam. A gas in thermal equilibrium at temperature T possesses a Maxwellian velocity distribution. The probability that a given atom has velocity between V and V+dV is given by

$$P(V)dV = \left(\frac{m}{2\pi kT}\right)^{1/2} \exp\left(\frac{-mV^2}{2kT}\right) dV \qquad \text{(eq.3.1.3)}$$

where m is the atomic mass and k is Boltzmann's constant. This distribution of velocities gives rise to a thermally-broadened, normalized fluorescence lineshape (Yariv, 1989)

$$g(\nu,T) = \left(\frac{D}{\pi T}\right)^{1/2} \exp\left(\frac{-D(\nu-\nu_0)^2}{T}\right) \qquad \text{(eq.3.1.4)}$$

where $D = m\lambda_0 / 2k = 497.6165K \cdot (ns)^2$ for Na atoms. Here, $g(\nu)d\nu$ represents the probability that the transition frequency is between v and v+dv. This is simply the probability that the velocity of a given atom is between $(\nu - \nu_0)\lambda_0$ and $(\nu + d\nu - \nu_0)\lambda_0$. The intensity of the emission line at frequency v is directly proportional to g(v). The lineshape has a full-width-at-half -max (FWHM)

$$\Delta\nu_{doppler} = \nu_0 \left(\frac{8kT\ln(2)}{mc^2} \right)^{1/2} \qquad \text{(eq.3.1.5)}$$

For atmospheric pressures in the mesopause region, other line-broadening mechanisms such as collision-broadening are negligible (Yu, 1994) and Doppler-broadening is the dominant broadening mechanism. The linewidth of the fluorescence induced by a narrow-band laser can thus be used to measure atmospheric temperature.

Now suppose that the gas is moving with collective velocity V_{wind} relative to the ground-based laboratory. This motion is common to each atom and thus introduces no additional broadening. It does, however, shift the resonance frequency of all atoms by V_{wind} / λ_0 (eq.3.1.2). The entire lineshape is then shifted by the same amount, resulting in the Doppler-shifted lineshape

$$g(\nu, T, V_{wind}) = \left(\frac{D}{\pi T} \right)^{1/2} \exp\left(\frac{-D(\nu - \nu_0 - V_{wind}/\lambda_0)^2}{T} \right) \qquad \text{(eq.3.1.6)}$$

Line-of-sight velocities can be deduced from the Doppler shift of the atomic fluorescence spectrum. From here on, the wind subscript will be dropped from velocity, with the understanding that V refers to the line-of-sight wind speed.

Equation (3.1.6) can be applied to a collection of sodium atoms in the mesopause region. The Na atoms are in thermal equilibrium with air molecules and are carried along with the collective molecular motion (wind). We thus assume that the Doppler-broadened and shifted D_2 transition can be used to determine temperature and line-of-sight winds. The Na D_2 transition consists of two groups of lines arising from the hyperfine-splitting of the ground state (Fig. 3.1(a)). Transitions (numbered 4-6) terminating in the higher-energy

ground state form the D_{2a} line and transitions (numbered 1-3) terminating in the lower-energy ground state form the D_{2b} line. The sodium D_2 lineshape is given (She et al, 1992) by the sum of these transitions (eq.3.1.6)

$$g_{na}(\nu,T,V)=\left(\frac{D}{\pi T}\right)^{1/2}\sum_{n=1}^{6}A_n\exp\left(\frac{-D(\nu-\nu_n-V/\lambda_0)^2}{T}\right) \quad \text{(eq.3.1.7)}$$

where the coefficients A_n are relative linestrengths of the hyperfine transitions and are given in table 3.1. The frequency of each transition, relative to the weighted center (weighted by the A_n) of the six transitions, are also given.

Table 3.1 Parameters of Na D_2 Transitions. Frequency is relative to centroid frequency of D_2 transition. Values of relative linestrengths A_n are modified to account for the Hanle effect, which is the backscattering dependence on the orientation of laser beam polarization with respect to the earth's magnetic field. This effect is discussed in detail in previous CSU lidar dissertations (H.Chen, 1997).

Group	Transition (n)	Frequency(GHZ) ν_n	A_n (No Hanle effect included)	A_n (Incuding Hanle effect)
D_{2a}	1	1.0911	5/32	5/34.16
	2	1.0566	5/32	5.5/34.16
	3	1.0408	2/32	2/34.16
D_{2b}	4	-0.6216	14/32	15.68/34.16
	5	-0.6806	5/32	5/34.16
	6	-0.7150	1/32	0.98/34.16

For Na atoms at 200K, each of the six lines possess a Doppler width of 1.06GHZ (eq.3.1.5). The broadening is much larger than the spacing between upper level states and the six lines are thus blurred into two Doppler-broadened lines, which will referenced as D_{2a} and D_{2b}. The Doppler-broadened spectrum is shown for four different temperatures in Fig 3.1(b).

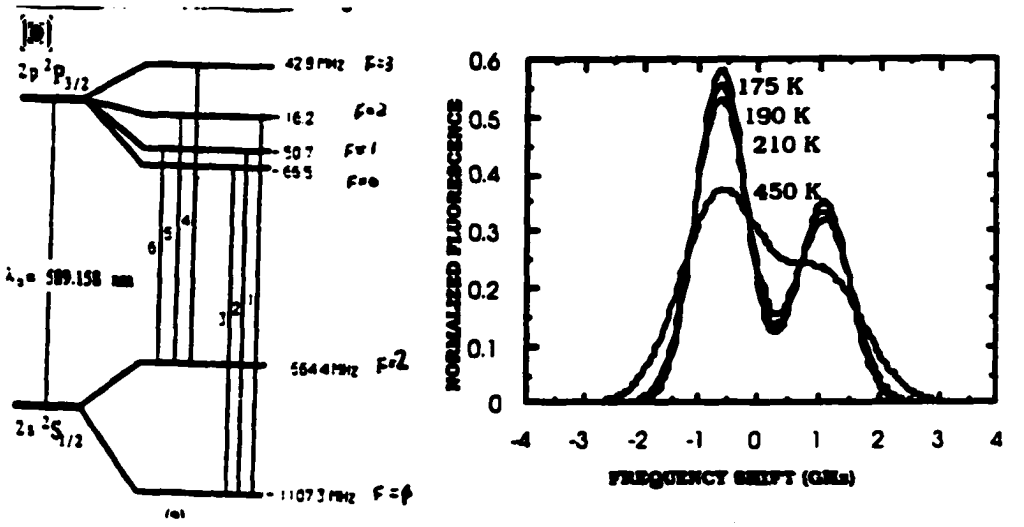

Figure 3.1 Na D_{2a} transitions (1-3) and D_{2b} transitions (4-6) are shown in (a). Due to Doppler broadening, these transitions are blurred into two features. (She, et.al, 1992)

3.2) Experimental Determination of Temperature and Winds

The lidar equation (6.1.1) is used to deduce temperature and line-of-sight velocity from the backscattered photon count profiles. The temperature and velocity dependence is contained in the Na D_2 differential backscattering cross-section, which for isotropic scattering is given by

$$\frac{d\sigma_{na}}{d\Omega}\Big|_{\pi} \equiv \sigma_{na}^{\pi}(v,T,V) = \frac{\sigma_{na}}{4\pi} = \left(\frac{g_2}{g_1}\right)\frac{\lambda^2_0}{2} A_{21} \cdot g_{na}(v,T,V) \qquad \text{(eq.3.2.1)}$$

where A_{21} is the Einstein A coefficient and g_2/g_1 is the degeneracy ratio. The values for the Na D_2 transition are $6.289 \cdot 10^7 s^{-1}$ and 2, respectively. The absorption cross-section for the transition is $\sigma_{na} = 9.5 \cdot 10^{-16} m^2$.

Up to this point, the laser beam has been assumed to be monochromatic. The high-energy, pulsed lasers used in lidar systems possess, at best, a Fourier-limited linewidth. We thus need to account for the effect of laser linewidth on the induced Na fluorescence spectrum. The Na fluorescence spectrum induced by a laser with normalized (to unit

area) lineshape $L(\nu-\nu_L)$ is given by the correlation of the laser lineshape with the Doppler-broadened Na fluorescence lineshape (She, et.al, 1992)

$$g(\nu_L,T,\mathrm{V}) = \mathrm{L}(\nu-\nu_L)\otimes g_{na}(\nu,T,\mathrm{V}) \qquad \text{(eq.3.2.2)}$$

where ν_L is the centroid frequency (i.e the center of "mass") of the pulsed laser spectrum. The frequency v in eq.3.2.1 is now replaced by the pulse centroid frequency ν_L. Note that for a monochromatic laser source, $L(\nu-\nu_L)$ is a delta function and g= g_{na}.

Since the hyperfine energy levels for the sodium atom are known to fractions of a MHz accuracy (Arimondo, et al., 1977), eq.3.2.1 and eq.3.2.2 provide a means for accurate temperature and line-of-sight wind determination from fluorescence induced by a narrow-band laser. Two approaches have been used to pr obe this spectrum. The first approach involves scanning a narrowband laser across the D_2 spectrum and fitting the induced fluorescence to the theoretical function. (eq.3.2.2). This approach was used by Fricke and vonZahn (1985) to measure mesopause temperatures. The second approach, utilized by the CSU lidar group, involves measuring the ratio of induced-fluorescence at selected frequencies possessing high sensitivity to temperature and wind speed. These ratios are then compared to theoretically-computed ratios (derived from eq.3.2.2). From Fig. 3.2(a) and 3.2(b), it can be seen that regions near the D_{2a} peak and near the valley between the peaks possess high temperature-sensitivity but are insensitive to velocity changes. Frequencies on either side of the D_{2a} peak, on the other hand, possess high velocity-sensitivity but are relatively insensitive to temperature changes. It is thus apparent that separate ratios are necessary in order to accurately measure temperature and winds.

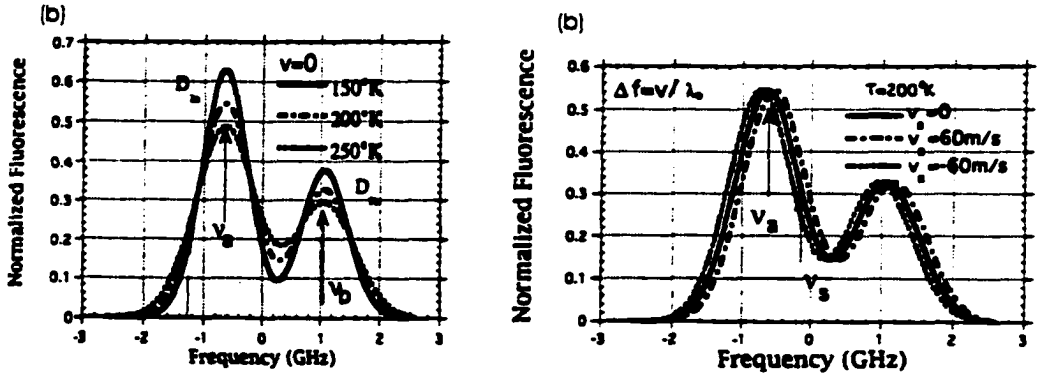

Figure 3.2 Sensitivity of the Na D_2 spectrum to temperature (a) and radial velocity (b) changes. (White, 1999)

A three-frequency lidar was developed (White, 1999) which utilizes the scattered fluorescence intensity at three frequencies to form two ratios, one most sensitive to temperature and the other most sensitive to velocity. For practical reasons (Chapter 4) these frequencies were chosen as the D_{2a} peak and $\pm 630MHZ$ relative to it. These frequencies will be referenced as ν_a, ν_+, and ν_- for the remainder of this thesis. In actuality, they represent the pulsed frequency centroid for each of the three lidar operating frequencies. The measured temperature and velocity-sensitive fluorescence intensity ratios

$$R_T = \frac{g(\nu_+,T,V)+g(\nu_-,T,V)}{2g\ (\nu_a,T,V)} = \frac{\sigma^{\pi}_{na}(\nu_+,T,V)+\sigma^{\pi}_{na}(\nu_-,T,V)}{2\sigma^{\pi}_{na}\ (\nu_a,T,V)} \qquad \text{(eq.3.2.3)}$$

$$R_v = \frac{g(\nu_+,T,V)-g(\nu_-,T,V)}{g(\nu_a,T,V)} = \frac{\sigma^{\pi}_{na}(\nu_+,T,V)-\sigma^{\pi}_{na}(\nu_-,T,V)}{n^{\pi}_{na}(\nu_a,T,V)}$$

are compared to a theoretically-calculated calibration curve using eq.3.2.2. Typical calibration curves are shown in Fig. 3.3.

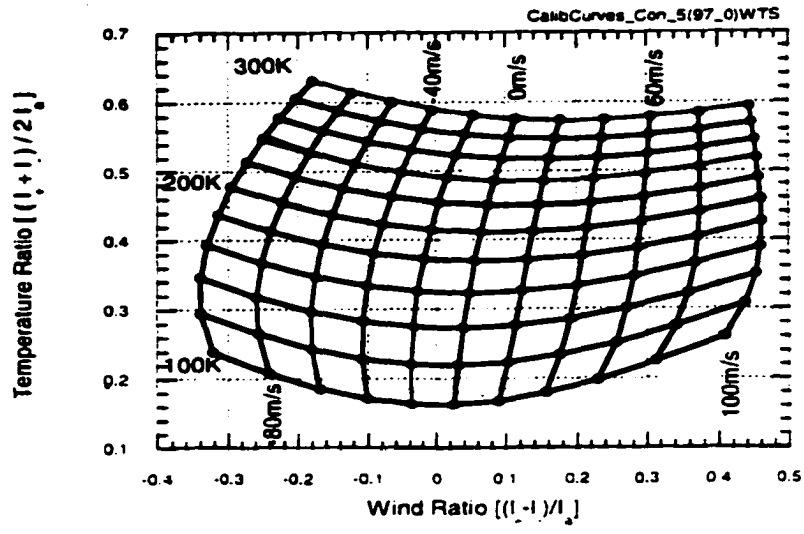

Figure 3.3 Typical 3-frequency lidar calibration curve, derived from eq. (3.2.2) and (3.2.3). Experimentally-measured temperature and wind ratios are compared to the calibration curve to derive temperature and radial winds

Stringent demands are placed on the lidar transmitter in order to accurately measure temperature and winds. The effect of correlation (eq.3.2.2) is to blur the details of the Doppler-broadened lineshape, thereby reducing measurement sensitivity by a factor $\Delta\nu_{doppler}/(\Delta\nu_{doppler}+\Delta\nu_{laser})$, where $\Delta\nu_{laser}$ is the FWHM of the laser lineshape (She, 1990). For the case of Na atoms at 200K($\Delta\nu_{doppler}$ ~1GHz) probed by a pulsed laser with linewidth $\Delta\nu_{laser}$ ~120MHz, this results in a reduction in measurement sensitivity of roughly 10%, relative to a perfectly monochromatic light source. It is thus necessary to use a tunable (to get to all three frequencies), narrowband laser with a linewidth much narrower than the Doppler-broadened Na fluorescence linewidth. The absolute frequency of the pulse centroid must also be accurately measured during data acquistion in order to accurately deduce temperature and winds from the measured fluorescence ratios (eq. 3.2.3). Finally, the pulse lineshape must be stable and well-known, since it is this lineshape which is used in eq.3.2.2 to generate the calibration curves. The requirements of a narrowband, tunable, frequency-stabilized, repeatable laser pulse give rise to the unique CSU Na fluorescence lidar transmitter design, which will be discussed in chapter 4.

Chapter 4-The CSU Lidar System

All lidar systems consist of a transmitter, receiver, and signal-processing electronics. The transmitter in turn can often be divided, for convenience, into cw (continuous-wave) and pulsed subsystems. In the case of the CSU lidar, cw and pulsed-subsystem outputs interact in the pulsed-dye amplifier (PDA) to produce tunable, narrowband, frequency-stabilized lidar output pulses. This chapter presents an overview of each of these subsystems, with emphasis on the functionality of each subsystem. Some of these subsystems have constituted major portions of past and present CSU lidar dissertations. For brevity, the reader will be referred to appropriate works for greater detail. Section 4.1 describes the CSU lidar transmitter. The receiving system is discussed in section 4.2. A brief overview of the lidar operation sequence is presented in section 4.3, along with a typical altitude and frequency-resolved photon count profile obtained during data acquisition.

4.1 CSU Lidar Transmitter.

As stated in chapter 3, accurate temperature and wind measurement place stringent demands on the spectral properties and stability of the output laser pulses. Output pulses for this transmitter (Fig. 4.1) are derived from a tunable, single-mode cw ring dye laser, which seeds a pulsed-dye amplifier (PDA). The PDA is pumped by a Q-switched, 50Hz, frequency-doubled Nd:YAG laser. Various transmitter subsystems are responsible for satisfying the stringent demands required of the output laser pulses. These subsystems and their roles will be discussed here.

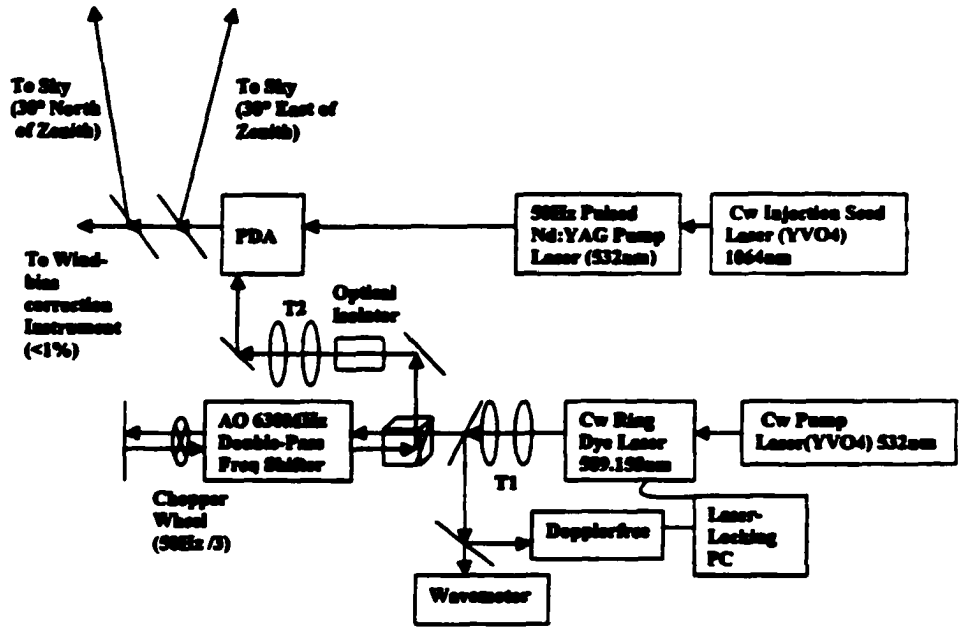

Figure 4.1 CSU Lidar transmitter. Light propagation is denoted by arrows. Beam-turning mirrors and beamsplitters are unlabeled, with the distinction that one arrow (light beam) is incident on beamsplitter and two arrows(beams) leave the beamsplitter. Telescopes are denoted by T. A small amount of transmitted light (<1%) from North beam-steering mirror is used by the wind-bias correction instrument.

CW Subsystem:

The cw seed beam entering the PDA sets the center frequency of the output laser pulse. It is therefore important that seed beam frequencies are accurately-stabilized and can be monitored during data acquisition. The cw seed beam is derived from a tunable, single-mode ring dye laser (Coherent 899-21) pumped by a frequency-doubled (532nm) Nd:YVO_4 laser. The ring laser gain medium consists of 1 gram of Rhodamine 590 dye dissolved in 1200ml of Ethylene glycol. The center operating frequency of the three-frequency transmitter is locked to the largest D_{2a} hyperfine feature of a laboratory Na vapor cell utilizing saturated Doppler-free fluorescence spectroscopy (She, Yu, 1995). Two counter-propagating beams of nearly-equal intensity overlap in the vapor cell (Fig 4.2(a)), which is heated to 70°C and is four inches in length. If the intensity is sufficient to saturate the D_{2a} hyperfine transitions, holes are burned in the fluorescence spectrum (Fig. 4.2(b)), which is measured by a photomultiplier tube (PMT), at each of these

transition frequencies. This method is also referred to as Lamb-dip spectroscopy in the literature. The features are very sharp and permit the cw ring laser to be actively stabilized to the largest D_{2a} hyperfine feature to within 1 MHz over several hours during data acquisition. It was experimentally measured that that this level of frequency accuracy is only possible if cw power entering the Dopplerfree apparatus is $\leq 180\mu W$ (for a beam of 1/e radius of 1mm). As power is increased beyond this amount, saturation broadening broadens the hyperfine features, thereby reducing frequency sensitivity. If the intensity is further increased to about 800μW, the neighboring hyperfine D_{2a} feature, located 16MHz (She and Yu, 1995) away, can saturate to a greater extent than the correct D_{2a} feature, resulting in the ring laser being locked to the wrong peak.

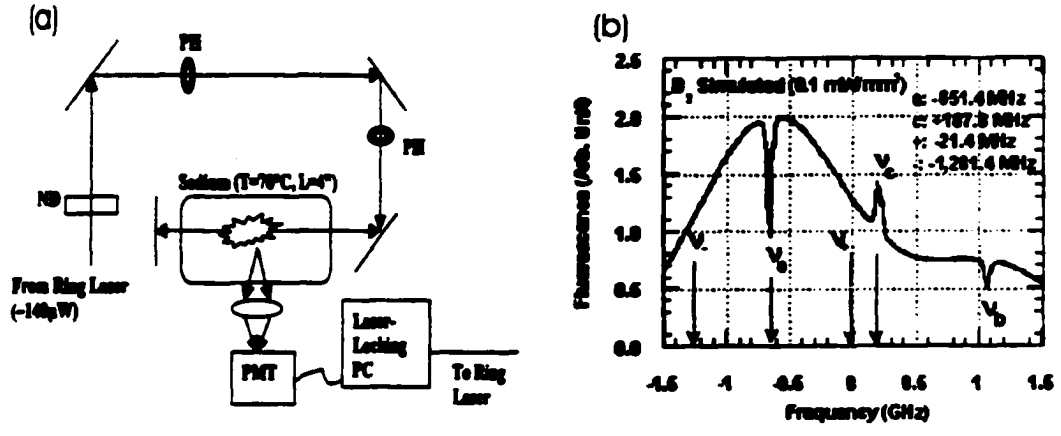

Figure 4.2 (a) Dopplerfree saturation fluorescence spectroscopy apparatus. Counter-propagating beams induce fluorescence, which is focused onto PMT (cathode voltage=-450V). (b) Fluorescence spectrum. The symbols ND and PH denote neutral density filters and alignment pinholes, respectively. Frequency subscripts a, b, c in part (b) denote D_{2a}, D_{2b}, and crossover resonance. The + and - subscripts denote shifted frequencies in three-frequency lidar operation.

The remaining two frequencies are derived from a double-pass 630MHz acousto-optic frequency shifter (Fig. 4.3(a)), referred to as the AO. This method of frequency shifting is much faster and more reproducible than tuning the ring laser and permits rapid (50Hz) cycling between the three lidar operating frequencies (White, 1999). The frequency shifters operate by the principle of Bragg scattering, by which light waves are diffracted from refractive index variations in the acousto-optic crystals. These variations are

produced by 315MHz microwaves, which propagate through the AO crystals. If the light beam is incident at an angle θ_{Bragg} from the moving acoustic wavefronts (Fig.4.3(b)), a strongly-diffracted beam, deviated from the original beam by an angle $2\theta_{Bragg}$, will result. Since the powered crystals function like moving diffraction gratings, the light beam frequency will be shifted by +315MHz or -315MHz, depending on the direction of the acoustic wave relative to the light beam. For the crystals used in the CSU lidar, θ_{Bragg}=1.22°. The diffraction efficiencies of the aging crystals are measured to be between 70% and 80%. (50%-64% double pass).

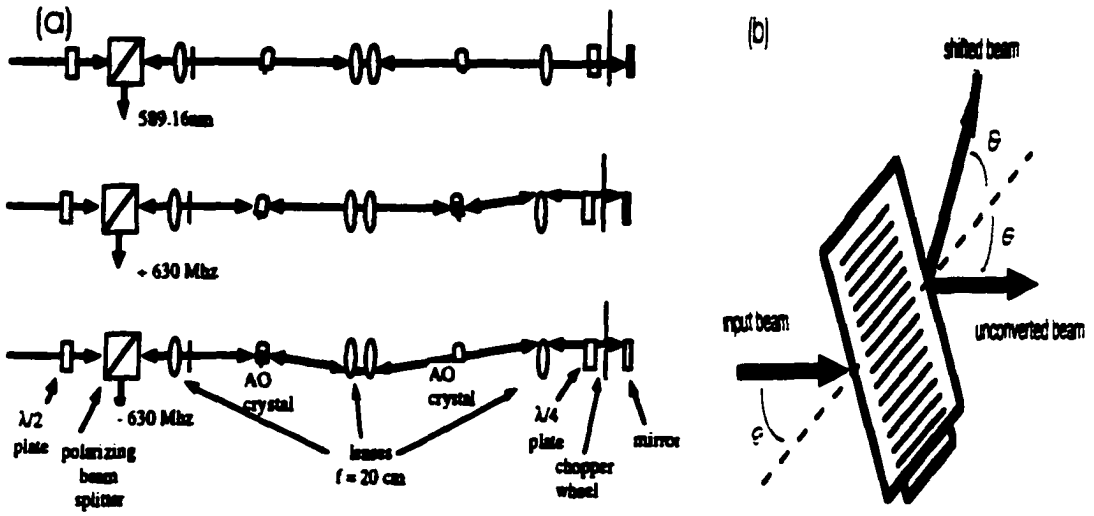

Figure 4.3 (a) Double-Pass 630MHz acousto-optic frequency shifter apparatus. (b) Bragg diffraction of laser beam from moving acoustic wavefronts (wavefronts are denoted by lines). The beam frequency is upshifted in the case of acoustic waves moving toward top of figure and downshifted in the case of acoustic waves moving toward bottom of figure (from White, 1999).

Each three-frequency cycle proceeds as follows (Fig. 4.3(a)): The laser is locked at ν_a. During the first pulse (top picture), both crystals are off and the beam traverses the double-pass frequency shifter (AO) unchanged. During the second pulse (middle picture), only the back crystal is powered and the beam experiences Bragg diffraction and a frequency shift of +315MHz. The beam is reflected from a mirror and returns along the same path, experiencing another +315MHz shift, for a total shift of 630MHz. During the third pulse bottom picture), only the front crystal is powered. The acoustic wave for this crystal propagates away from the laser beam and so, by the same process, this beam

experiences a double-pass shift of -630MHz. A periodic sequence of focusing and collimating 20cm focal length lenses is used to repeatedly focus light into the crystals and so that all three beams will leave the AO and proceed toward the PDA along the same path. A rotating chopper wheel is inserted before the back mirror to block any unconverted light from propagating toward the PDA, thereby preserving spectral purity of the three beams. Chopper wheel electronics also provide synchronization for the lidar by triggering the pulsed Nd:YAG laser flashlamps at 50Hz. This triggers the YAG pulse, to which the range-gating counter electronics are referenced.

Other optical components also perform functions (Fig. 4.1) important to transmitter operation. Mode-matching telescopes match the ring laser output beam to AO input and the AO output beam to PDA input. Mode-matching is critical, as all three beams must leave the AO along the same path and have the proper beam waists in order to be transmitted through the 50μm spatial filter before the first PDA stage (Fig. 4.4).

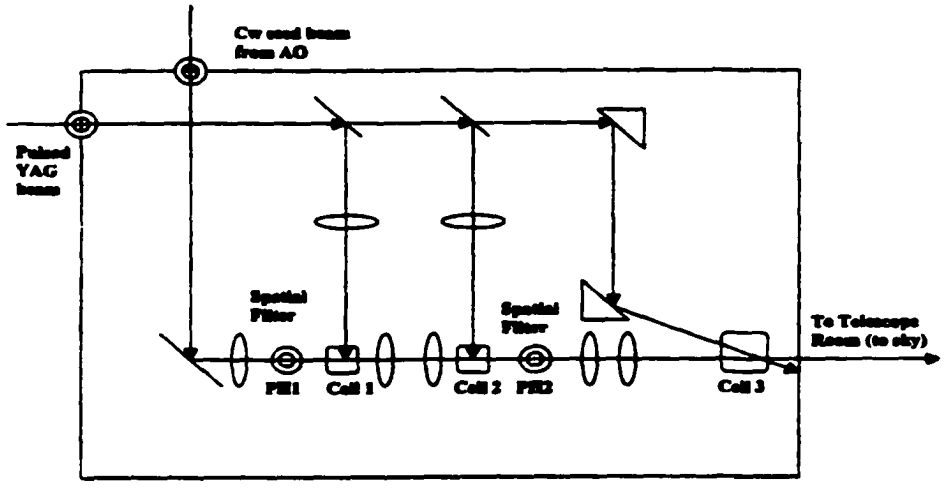

Figure 4.4 Pulsed dye amplifier (PDA). The cw seed beam and Nd:YAG pulsed beam interact in three dye cells (stages), separated by spatial filters. PH1 is a 50μm diameter pinhole and forms the limiting aperature for the three cw beams. PH2 is a 150μm diameter pinhole.

Improved mode-matching has, along with improved frequency locking, significantly reduced transmitter-induced wind bias (chapter 5). An optical isolator is inserted before the PDA in order to decouple the cw system from any broadband light reflected from the

PDA optics. These reflections introduce frequency jitter into the system and could potentially damage transmitter optical components.

Pulsed Subsystem:

The three frequency-stabilized cw beams which alternately enter the PDA satisfy necessary conditions of transmitter tunability and frequency stability. The function of the pulsed subsystem is to assure narrow linewidth and smooth, repeatable PDA lineshapes. The pulsed subsystem consists of a 50Hz, Q-switched, frequency-doubled (532nm) Nd:YAG laser which is injection-seeded by a single-mode cw Nd: YVO_4 laser. The injection seeder is frequency-stabilized at the peak of the YAG gain curve. This narrowband seed light is injected into the YAG cavity when the Q-switch opens. Since its frequency is matched to the YAG gain curve and its power (2.5mW) is orders of magnitude greater than the spontaneous emission, energy is quickly extracted into a narrow bandwidth (120MHz), frequency-repeatable, smooth pulse of roughly 7ns and energy 30mJ. Injection seeding is monitored by two independent methods during data acquisition to assure stable, narrow-linewidth transmitter output pulses. Due to the fact that the PDA dye gain curve is flat over the range of lidar operating frequencies, PDA linewidth is largely determined by the linewidth of the pulsed Nd:YAG laser which pumps it. Wind measurement instabilities were in fact observed during March and April of 2002, due in part to a degraded injection seed laser which has since been replaced.

The beams from the cw and pulsed-subsystems interact in the three-stage pulsed-dye amplifier (PDA), which uses a mixture of Rhodamine 640 (9.16mg for first two stages and 1.9mg for third stage) and Kiton Red 620 (44.3mg for first two stages and 14.3mg for third stage) dyes dissolved in 1000ml methanol (each stage) as gain medium (Fig. 4.4). The resulting PDA pulse is narrowband (120MHz), smooth, and reproducible, with pulse energies of 24mJ for the ν_a beam and 18-20mJ for the two frequency-shifted beams. The full-width beam divergence angle is approximately 1 milli-radian. The pulse is split into two beams, one directed into the atmosphere at 30° east of zenith and the other at an angle 30° north of zenith. Fluorescence introduced by these beams yields temperature,

zonal (east beam) and meridional (north beam) wind profiles of the mesopause region. Horizontal velocities (zonal and meridional) are obtained from

$$V_{radial} = V_{horiz} \sin(30) + V_{vert} \cos(30) \approx V_{horiz} / 2 \qquad \text{(eq.4.1.1)}$$

where the assumption of negligible vertical velocities (section 2.2) on the time-scales of CSU lidar integration was used. A small portion of the output energy transmitted through one of the beamsteering mirrors is used by the wind-bias correction (chapter 5) instrument to correct for small shifts in the pulsed frequency centroid from cw seed beam inputs. These shifts could introduce a 10-15m/s bias (White, 1999) to the radial wind measurement. These biases have been reduced to 1-3 m/s (this thesis) and corrected to $\leq 1 m/s$ using the wind-bias instrument. This instrument is the subject of chapter 5.

One last transmitter requirement introduced in chapter 3 but not yet addressed is that the pulsed lineshape be accurately-measured. This is necessary as it is the pulsed PDA output which induces Na fluorescence and whose spectrum is used in the calibration curves derived from eq. 3.2.2 and eq.3.2.3. Routine measurements of PDA lineshape taken over the past two years reveal that the shape is smooth and reproducible, with a linewidth between 110-120MHz under the conditions of good injection seeding. Due to the correlation of the lineshape with the much wider Na absorption spectrum, small long-term changes of 5-10MHz in the linewidth do not significantly change the calibration curve, introducing temperature errors of <1K and radial velocity errors of <0.5m/s. The details of the PDA lineshape measurement and the software written to process the results are discussed in Appendix A.

4.2) Overview of the Lidar Receiver

Backscattered photons are collected by the lidar receiver (Fig. 4.5) and processed, yielding range-resolved temperature and wind profiles. The photons are collected by a 14-inch diameter Schmidt-Cassegrain telescope. A 3-nm narrow bandpass filter, with 70% transmission at 589nm, is located near the telescope focal plane, reducing background light levels from the moon and stars (and the sun during day-time operation).

The light is then focused into a 1mm diameter, multi-mode fiber and directed toward the receiver electronics, located in the backroom of the lidar laboratory. Light emerging from the fiber is then collimated and directed on an air-cooled (to reduce thermal noise) PMT cathode. Due to low backscattered signal levels, the PMTs operate in photon-counting mode. A 50μs blanking pulse is applied to the first stage of each PMT, synchronized to the exiting transmitter pulse. This turns off the PMT high-voltage gain for light backscattered from air molecules and aerosols in the first 7.5km of atmosphere. This signal is large enough to saturate and possibly damage the PMTs. The sudden application of the high-voltage gain at 7.5km creates PMT ringing, and thus altitude-dependent PMT gain, which is accounted for in the data analysis (Chapter 6) by normalizing the photon counts in each altitude bin by the pmt gain for that altitude.

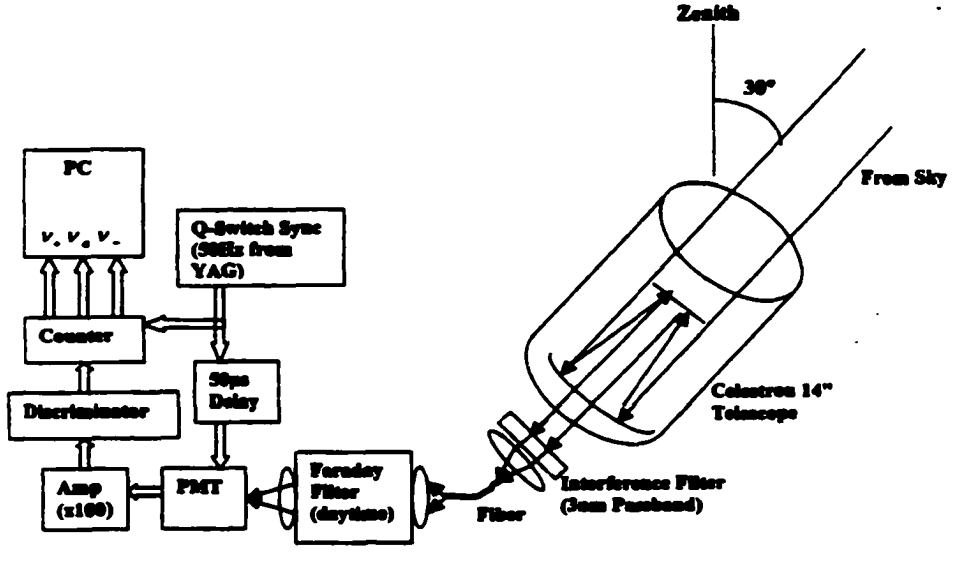

Figure 4.5 Lidar Receiver (figure represents one of the two channels). Telescope 1 points 30° east of zenith to measure zonal winds. Telescope 2 points 30° north of zenith to measure meridional winds.

In photon-counting mode, current pulses produced by the PMTs are amplified by fast preamplifiers (gain=100). These pulses are sent to a discriminator, whose threshold voltage is set to reject most noise pulses while converting photon pulses to TTL logic-level pulses. The logic pulses are sent to the counter board, which sorts pulses by time-of-flight (altitude) binning and by frequency. Range-resolved photon counts for each

frequency are separately summed over the 2-minute file period (2000 laser pulses at each frequency).

A stable, narrowband filter is necessary for daytime lidar operation in order to extract weak, narrowband signal from the large, broadband solar background, which is strong enough to damage the PMTs and their coupling fibers. A dispersive Na atomic vapor filter utilizing the Faraday effect was introduced (H.Chen, 1996), permitting daytime temperature and Na density measurements of the mesopause region. Details of the Faraday filter are the subject of recent CSU lidar dissertations (H.Chen, 1996; S.Chen, 1999), to which the interested reader is referred. The Faraday filter consists of a heated Na vapor cell (T=170°C) in an axial magnetic field (B=1800Gauss) placed between two crossed-polarizers (Fig.4.6(a)).

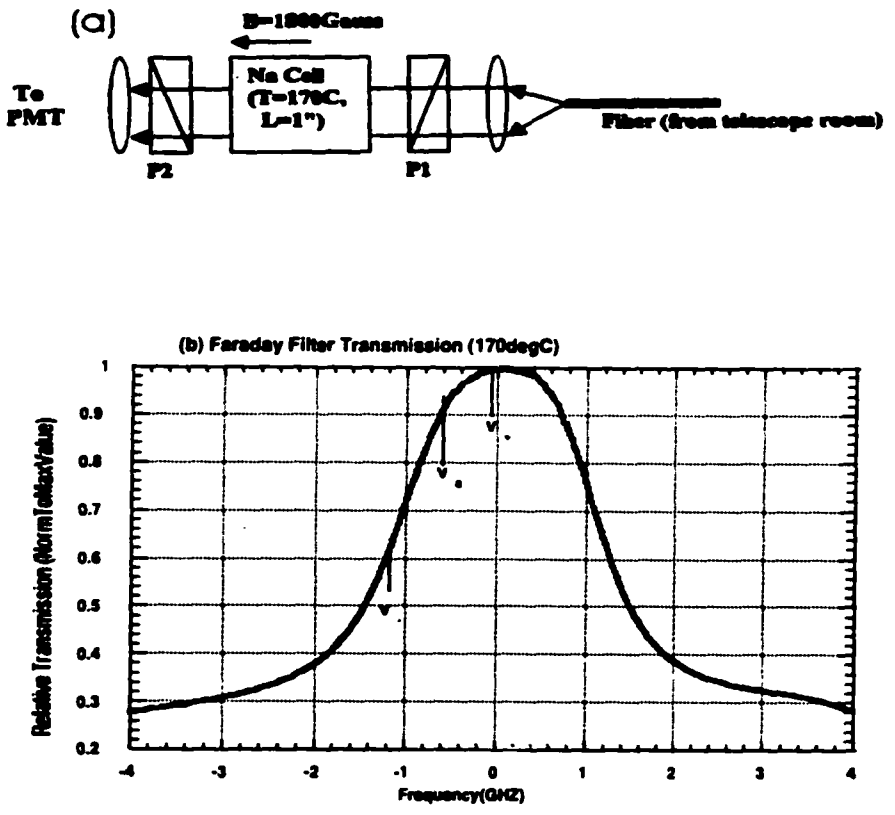

Figure 4.6 (a) Faraday filter apparatus. Symbols P1 and P2 represent the crossed polarizers. (b) Faraday filter transmission spectrum, measured at 170°.

The polarization of a linearly-polarized light wave propagating through a circularly-birefringent medium is rotated by an amount proportional to the difference in refractive index for the two circularly-polarized basis states. This difference is determined by B and by the quantum mechanics of the atomic vapor. The rotation also is proportional to the optical depth, which depends on T and on cell length L (one-inch). For the proper choice of B, T, and L, light near the Doppler-broadened atomic resonances is rotated by 90° and transmitted by the second polarizer. The polarization of the broadband background light is unchanged in propagating through the cell. Background light is thus blocked by the second polarizer. The Faraday filter transmission curve is shown in Fig. 4.6(b). For the current B, T, and L, the filter has a transmission width (FWHM) of 2.5GHz, centered at the center of the Na D_2 transition. Maximum transmission is roughly 25%, due to loss of half of the signal at the first polarizer and losses within the cell and at optical surfaces. Filter calibration spectroscopy is discussed in Appendix A.

4.3) Operation of the Three-Frequency Temperature/Wind Lidar

This section describes the sequence of events constituting each two-minute data file, as well as the role of the lidar operator in maintaining proper system operation.

Each two-minute data acquisition file proceeds as follows: The data acquisition PC has a 'low-hold' output, which must be in a 'high' logic state for counter triggering to occur. Before each two-minute (6000 pulses, 2000 at each frequency) integration period, the laser-locking PC re-acquires lock of the cw ring dye laser to the largest Na D_{2a} Dopplerfree feature. It then sends a signal to the data-acquisition PC, switching 'low-hold' to a 'high' logic state. Counting is initiated when the counters receive the first 'reset' pulse from the AO chopper wheel, synchronous to the first pulse at ν_a (relative to 'low-hold' switching to a 'high' state). This assures proper sequencing of frequencies, as the data-analysis is configured for the operation sequence ν_a, ν_+, ν_-. Each 1/50 second, the AO chopper wheel holes move into position to transmit one of the three cw beams (ν_a, ν_+, or ν_-) on toward the PDA. Power is applied to the appropriate AO crystal if the

frequency is to be shifted. Chopper wheel electronics then trigger the pulsed Nd:YAG flashlamps. A Q-switch synchronization signal (50 Hz TTL) is produced approximately 200μs later, synchronous to laser pulse emission. This signal triggers the range-gating counters, initiating time-of-flight binning (Fig. 4.5). It also triggers the PMT blanking circuitry and the frequency-doubling circuit for the wind-bias correction electronics (Chapter 5). Laser pulses cycled between ν_a, ν_+, and ν_- are directed toward the atmosphere at 50Hz. Backscattered photons are collected by the telescope, converted into pulses, and sorted by frequency and altitude. Pulses for each frequency in each range bin are summed over the two-minute integration period. When 6000 Q-switched trigger signals have been counted, 'Low-hold' switches to a 'Low' logic state, ending data acquisition. Frequency and altitude-resolved profiles are saved to disk at this time while the locking PC re-locks the ring laser to the D_{2a} peak, initiating another two-minute integration period. This process is repeated over the four to 60-hour data acquisition periods. Altitude-resolved photon counts for a typical night file are shown in Fig. 4.7.

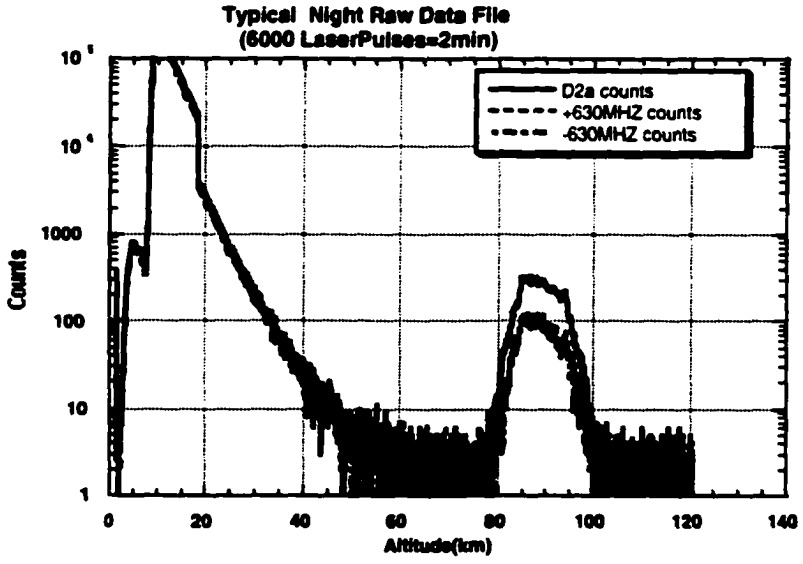

Figure 4.7 Photon counts at the three lidar operating frequencies for a typical spring night file. A log scale is used to show all features. The vertical axis limit was chosen as five (log scale) so as not to obscure sodium signal from 80-105km. Range bin sizes are 750m for lowest 18km of atmosphere and 150m for all other altitudes in figure.

The large spike at 7.5km is due to PMT high-voltage gain being switched on. The ρ / z^2 (where z=altitude and ρ is atmospheric density) Rayleigh scattering is evident from 25-80km. This scattering is proportional to laser pulse energy and is used to normalize lidar returns at the three operating frequencies to pulse energy at that frequency (Chapter 6). Frequency-dependent returns from 80-105km result from resonant backscattering by Na atoms and are used to determine Na density, temperature, and winds. All counts above some reference altitude (120 km), which is too high to contribute to resonant backscattering, are considered background counts. An average of counts above this level is formed and subtracted from the signal at lower altitudes (Chapter 6).

In order to assure proper lidar operation during a given file, laser locking is monitored by the Dopplerfree fluorescence PMT signal sent to the locking PC. The PC applies a feedback voltage to the ring laser to maintain locking to within ± 1.5MHz of the peak voltage. This is accomplished by dithering the ring laser cavity length (and hence frequency) at 230Hz over a 3MHz range, continually finding the peak PMT voltage in this range and re-locking the laser to that point. Laser locking is also monitored by the lidar operator, who must re-lock the ring laser to the D_{2a} peak in the event of a laser mode-hop or other event which would cause the laser to lose lock. The operator also monitors laser power and correct frequency-sorting of the range-gated photon counts. During a typical data-taking campaign, one file every two hours may be discarded due to noise-triggering of the counters. (Such an event can also be detected by post-processing) This results in photons collected during the remainder of the file being placed in incorrect frequency bins. The operator also monitors wind-bias correction signals (using a 500MHz oscilloscope), overlapping the pulses with the gated integrators. This will be discussed in chapter 5.

Chapter 5- Hardware Modifications Leading to Vector Wind Measurements

This chapter describes hardware modifications leading to the implementation of a two off-vertical beam lidar, permitting simultaneous measurement of temperature, zonal and meridional winds. Shortly after the CSU two-frequency temperature lidar was upgraded to include a third frequency used for wind measurements, a systematic 10-15 m/s magnitude vertical wind bias was discovered (White, 1997). The vertical wind measurement is used to calibrate the lidar radial wind measurement (Recall from chapter 2 that vertical winds should be on the order of a few cm/sec for measurements on the timescale of one-hour with power-aperture product of the CSU lidar). As a result, one of the two lidar beams was pointed toward zenith and used solely to measure and correct instrument-induced bias, permitting measurement of only one horizontal wind component. Though an often-used lidar technique, this is hardly an efficient use of lidar resources.

It was determined that this bias resulted from a shift of the pulsed-dye amplifier (PDA) frequency centroid, relative to cw seed beam frequency. An instrument was designed and implemented (White, 1999) to measure instrument-induced radial wind bias so its effect could be eliminated from the wind results. Eight nights of vertical wind measurements demonstrated the promise of this correction scheme, reducing measured vertical velocities to between 0.5-5m/s in magnitude. This early work will be discussed in Section 5.1. Studies were conducted (this thesis) with the purpose of identifying and characterizing instrumental sources of radial wind bias. These efforts, described in Section 5.2, were rewarded with the reduction of radial wind bias (uncorrected) to magnitudes of 1-3m/s under proper operating conditions (which will be discussed in this chapter). In the process, a better understanding of the instrumental radial wind bias sources was obtained.

Despite reduced radial wind bias magnitudes, improvements on the wind-bias correction instrument calibration and stability were necessary before moving the vertical-pointing lidar beam off-axis, thus enabling measurement of both horizontal

wind components. These improvements are discussed in Sections 5.3 and 5.4. The improved wind-bias correction instrument is now used more as a valuable diagnostic tool (as opposed to a tool of necessity) capable of consistently correcting radial wind biases to ≤ 1m/s (≤2m/s for horizontal wind components, from eq.4.1.1). Verification of wind-bias correction performance is provided in Section 5.6, after a discussion (Section 5.5) of sources of uncertainty associated with the wind-bias correction instrument.

At this point, the reader may wonder why so much effort has been devoted to correcting the now small residual radial wind bias. The wind-bias correction instrument also serves as an extremely sensitive indicator of many lidar transmitter problems, which occasionally result in relatively large (5-10m/s) radial wind biases. Because both lidar beams are now pointed off-vertical, such a tool is necessary in order to assure accurate, reliable temperature and horizontal wind measurements.

5.1) Initial Radial Wind-Bias Correction

Vertical velocity measurements derived from three-frequency lidar data revealed a systematic frequency shift in the centroid (i.e center of 'mass') of the PDA output frequency spectrum relative to cw seed beam frequency(White, 1999). The cw ring laser output has a linewidth on the order of 1MHz and can be considered as approximately monochromatic relative to the ~120MHz PDA linewidth. Since the lidar velocity measurement is based on Doppler frequency shift of the laser pulse induced by scattering sodium atoms, any transmitter frequency shift induces a proportional effect on the radial velocity measurement. The magnitude of this effect is given by

$$\Delta\nu = \frac{-V}{c}\nu_0 = \frac{-V}{\lambda_0} \qquad \text{(eq. 5.1.1)}$$

where $\lambda = c/\nu_0$ = 589.158nm is the center wavelength of the cw beam.

Solving for V, the velocity bias is given by

$$V_{bias} = -0.589 \cdot \Delta\nu \qquad \text{(eq. 5.1.2)}$$

where $\Delta\nu$ is in units of MHz and V_{bias} in units of m/s.

White (1999) showed that this shift was consistent with a time-varying phase modulation of the pulse frequency due to non-linear interactions between the cw seed beam and the YAG pump beam in the pulsed dye amplifier. This phenomena is known as pulse-chirping. (Siegman, 1986)

A pulsed-frequency monitor was designed and implemented in 1999 to measure instrument-induced radial velocity bias, so that its effect could be eliminated from lidar wind results. White made eight nights of vertical wind measurements with this arrangement, with the usual (during that time period) -10m/s to -15m/s bias corrected to nightly-averaged values of less than 5m/s, including two nights of less than 1m/s. This data justified the radial wind-bias correction method.

5.2) Characterization of Radial Wind Bias Sources

Efforts to improve the calibration and stability of the wind-bias correction instrument began in 2000. Parallel studies were conducted to determine the instrumental source(s) of this bias. Details of these studies are given in this section. The rationale for these studies was that instrument-induced radial wind bias could possibly be reduced, or even eliminated, if its source(s) was known. At the very least, understanding of the source(s) would help determine what types of error the instrument was capable of measuring.

The first observation was that the cw ring laser beam was not mode-matched to the AO (acousto-optic double pass frequency shifter, described in section 4.2) and that the beam exiting the AO was not mode-matched to the PDA. Lack of optimal mode-matching could possibly have been the result of different beam characteristics possessed by a new cw ring laser, installed in 1999. Mode-matching the ring laser beam to the AO is necessary to maximize the double-pass Bragg diffraction efficiency for both shifted beams. This is necessary in order for all three cw beams to

saturate the PDA, reducing wind-bias correction instrument errors (section 5.5). Mode-matching the AO output beam to the PDA is critical, as all three beams must leave the AO along the same path and possess the proper beam waist sizes (i.e Gaussian beam radius at the focus) in order to be transmitted through the 50μm diameter spatial filter pinhole, located at the focus of the front lens preceding the first PDA dye cell (Fig. 4.4). This requires a collimated beam, of waist size ~1mm, incident at the PDA entrance. Mode-matching telescopes were designed to achieve both functions and inserted in the transmitter. Another objective in the telescope design was to produce a larger and more collimated beam (~1mm waist size) incident on the sodium dopperfree fluorescence spectroscopy cell, resulting in more complete spatial overlap of the counter-propagating beams (section 4.2) and improved Dopplerfree spectrum, to which the ring laser is locked. The result was an increase (by a factor of three) of cw power transmitted through the pinhole and reduction in uncorrected vertical wind (radial wind bias) from 10-15m/s magnitudes down to approximately 4m/s. It should be noted that even with proper mode-matching, additional wind biases of a few m/s are introduced by imprecise nightly alignment of all three beams entering the PDA. Preliminary results seem to indicate that the wind-bias correction instrument is capable of correcting biases introduced by small alignment errors or beam drifts, which are common in long data runs.

The possible contribution of ring laser-locking errors to radial-wind bias was also studied. Decreased locking sensitivity due to power broadening of the Dopplerfree features (She and Yu, 1995) was realized and corrected (section 4.2), further reducing radial wind-bias magnitudes to 1-3m/s (2-6m/s for the horizontal wind components, by eq.4.1.1).

Other determined sources of wind-bias include poor YAG laser seeding and old or defective YAG laser flashlamps. Poor YAG laser seeding results in an erratic and broadened YAG laser output. The magnitude of increased radial wind-bias introduced by a 10-15MHz increase in PDA linewidth (from nominal 110-120MHz) was measured to be only ~0.5m/s but the resulting frequency instability proved difficult for the wind-bias correction instrument to correct. These problems surfaced

in conjunction with a degraded YAG seed laser, which was recently replaced. A degraded set of flashlamps installed in March resulted in a 4-6m/s increase in radial wind bias, which changed from hour-to-hour. Thermal effects in YAG rods (which are enhanced by aging or defective flashlamps) induce thermal focusing and birefringence (Sherman, 1998), which modify the YAG pump beam mode and polarization. Since this beam interacts with the cw seed beam in the PDA dye cells, changes in the YAG laser output result in changes in the PDA output. This additional 4-6m/s magnitude wind bias disappeared with the insertion of new flashlamps. The wind-bias correction instrument corrected for most of this (to within an additional 1m/s) increased radial wind-bias (section 5.6).

The result of these studies was to reduce the radial wind bias from 10-15m/s in magnitude to 1-3m/s (2-6m/s horizontal wind bias), under conditions of proper beam alignment and YAG performance. The bias is also much less variable than in the past. The role of the wind bias correction instrument now shifted from a tool of necessity to a diagnostic tool used to correct small radial wind biases but equally important, used to monitor operating conditions of the lidar transmitter. The improvements made to the monitor will be discussed next.

5.3) Calibration Spectroscopy of the Pulsed-Frequency Monitor

The transmission spectrum (relative) of iodine near 589nm (measured by scanning a tunable cw single frequency laser) is used to measure shifts of the PDA output beam frequency centroid, relative to the cw seed beam. The operating frequencies of the CSU Na lidar are located between two strong I_2 absorption lines. The I_2 cw transmission curve in this vicinity is shown in Fig. 5.1(a). The zero of frequency on this scale corresponds to the largest hyperfine peak of the Dopplerfree D_{2a} spectrum, to which the laser transmitter is locked. As can be seen from the figure, the D_{2a} peak (ν_a=0) lies on the opposite side of the transmission peak than the downshifted beam frequency (ν_- = -630MHz).

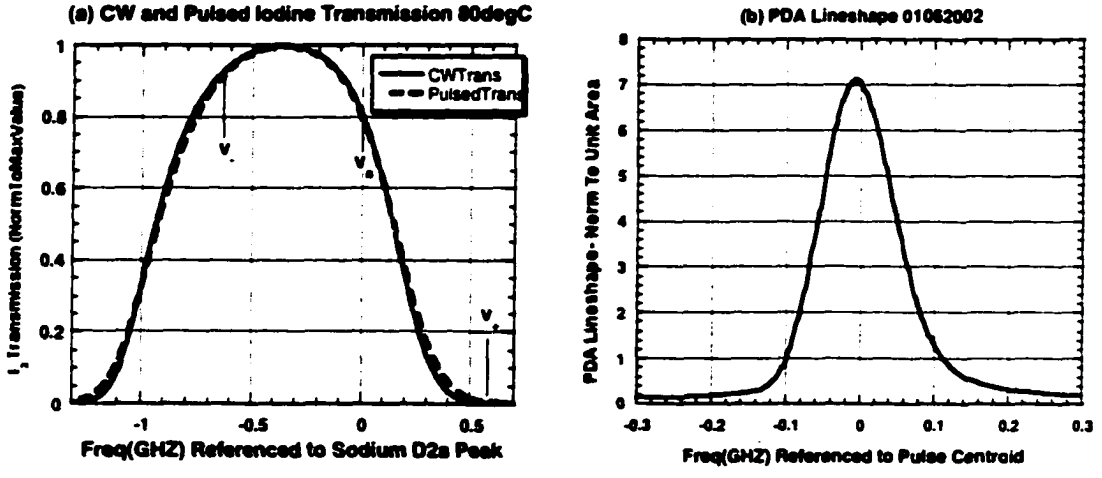

Figure 5.1 (a) Iodine transmission at 80°C for a cw beam and for a pulsed beam with frequency lineshape (b). The transmission for the pulsed beam is obtained by correlation of the iodine cw beam transmission with the PDA lineshape.

A positive shift in transmitter frequency will result in higher transmission at ν_+ and lower transmission at ν_- (and vice versa for a negative shift in transmitter frequency). The I_2 transmission at the up-shifted beam frequency (ν_+=+630MHz) is too close to zero to be used directly but is used to subtract broadband optical noise common to all three frequencies, as will be discussed later in this section. This transmission spectrum can be used, with proper calibration, to measure the PDA centroid frequency shift, relative to the cw seed beam frequency.

In this section, I will show why the simple cw iodine transmission shown in Fig. 5.1(a) is insufficient for accurate measurement of the pulsed frequency centroid shift. I will then show how the cw transmission curve is modified to obtain I_2 transmission for the pulsed beam. Finally, the pulsed beam transmission spectrum will be used to produce a calibration curve, which permits experimental measurement of PDA pulse frequency centroid shift, relative to the cw seed frequency. The reader is referred to Appendix A for experimental details of the spectroscopy used to generate the calibration curves.

The cw I_2 transmission spectrum, while used in the wind-bias correction monitor calibration, does not account for the finite (110-120MHZ FWHM) bandwidth and asymmetry in the frequency spectrum of the PDA (pulsed dye amplifier) output. The reader may at this point wonder why the monitor isn't calibrated directly by simply scanning the PDA pulse frequency over the I_2 transmission curve to obtain the I_2 transmission for the pulsed beam. Although pulse linewidth and asymmetry are reasonably stable (to within 10%) over years of measurements (provided that good YAG seed laser frequency stability exists, a condition which will be discussed in section 5.4), the absolute centroid frequency of the PDA pulse is the unknown measured by the monitor. Hence it can't be used directly to calibrate the wind-bias correction instrument.

Instead, the PDA frequency spectrum is measured, with the zero of frequency set to its centroid. Results of a typical measurement are shown in Fig. 5.1(b). A correlation of the two spectra then produces the transmission of I_2 for the asymmetric, finite-bandwidth pulsed-dye amplifier beam.

$$T_{pulsed}(\nu) = L_{pda}(\nu) \otimes T_{cw}(\nu) \qquad \text{eq 5.3.1}$$

where

$L_{pda}(\nu)$= the pulsed-dye amplifer lineshape (normalized to unit area)

$T_{cw}(\nu)$= the cw I_2 transmission (normalized to maximum transmission).

The cw and pulsed iodine transmission functions are plotted together in Fig. 5.1(a) and have been normalized to one at peak transmission. The widths of the two functions are very similar, as would be expected when correlating a 120MHz function with a 1.1GHz function. The pulsed spectrum, however, is narrower near the transmission peak and wider in the low transmission regions, than the cw spectrum. The two functions also differ more near ν_- than near ν_a. This is due to the asymmetry of the PDA frequency spectrum. This asymmetry, along with finite PDA

bandwidth, necessitates the use of the pulsed I_2 transmission function for accurate wind-bias correction instrument calibration.

The pulsed I_2 transmission curve is next used to calibrate the frequency monitor. Looking at Fig. 5.1(a), it can be seen that the I_2 transmission sensitivity to small frequency shifts is much greater (at the 80°C operating temperature of cell) at the un-shifted (ν_a) and downshifted (ν_-) operating frequencies than at the up-shifted (ν_+) operating frequency, for which it is very near zero. A ratio involving un-shifted and downshifted beam transmissions is thus used for calibration. The up-shifted beam transmission, while alone not very useful, can be used to account for broadband optical noise common to all three operating frequencies of the CSU lidar. This noise is known as amplified spontaneous emission (ASE) and represents a small, variable (1-2%) portion of the PDA output power on a typical night. To account for this, the ratio

$$R = \frac{(Neg - Pos) - (Peak - Pos)}{(Neg - Pos) + (Peak - Pos)} = \frac{Neg - Peak}{Neg + Peak - 2 \cdot Pos} \qquad \text{(eq. 5.3.2)}$$

was chosen where

Neg= I_2 pulsed transmission for the down-shifted beam (frequency center at ν_- = -630MHz)

Peak= I_2 pulsed transmission for the un-shifted beam (frequency center at $\nu_a = 0$)

Pos= I_2 pulsed transmission for the up-shifted beam (frequency center at ν_+ = +630MHz)

To generate the calibration curve, we start by using eq. 5.3.2 to calculate R for zero frequency shift of the PDA pulse frequency centroid, relative to cw seed frequency (using the spectrum shown in Fig. 5.1(b). This corresponds to the PDA pulses being centered at -630MHz, 0MHz, and +630MHz for the down-shifted, un-shifted, and

up-shifted beam respectively. All three pulsed beam frequency centroids are then shifted in 2MHz steps, from a frequency shift of -100MHz to one of +100MHz. R is calculated for each step. This procedure generates a curve for $R(v_{shift})$, where v_{shift} is the frequency shift of the PDA pulse frequency centroid, relative to the cw seed beam. The curve is then fit to a third order polynomial

$$v_{shift} = c0 + c1 \cdot R + c2 \cdot R^2 + c3 \cdot R^3 \qquad \text{(eq. 5.3.3)}$$

A typical curve is shown in Fig. 5.2. For this curve, the polynomial coefficients were c0=-0.0642, c1=0.8942, c2=-0.7672, c3=-0.2665. It can be seen from this curve that v_{shift} is a monotonically-increasing function of R. Thus, by measuring the ratio of normalized pulsed-beam transmission through the I_2 cell at the three lidar operating frequencies, the shift of the pulsed beam frequency centroid, relative to cw seed frequency, can be determined from eq.5.3.3. This shift is then used to subtract off the instrument-induced radial wind bias by eq. 5.1.2.

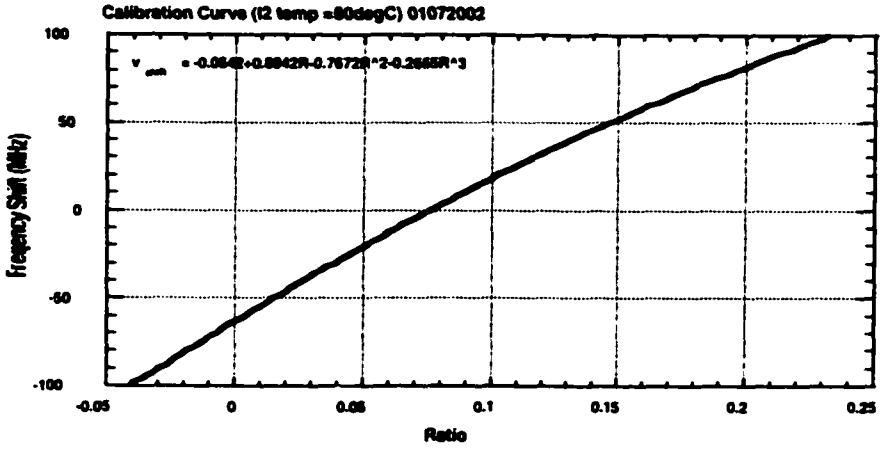

Figure 5.2 Wind-bias correction instrument calibration curve for January, 2002. The curve is derived from eq. 5.3.3.

At this point, the reader may be questioning the validity of assuming that the pulse centroids for all three lidar frequencies are shifted by the same amount. This

assumption has two requirements, which are to a large degree satisfied in practice and will be further discussed in section 5.5:

1)The cw seed frequencies are located at precisely -630MHz, 0, and +630MHz, relative to the transmitter locking point ν_a.

2) The PDA lineshape is the same for all three operating frequencies.

5.4) Experimental Design and Modifications to the Wind-Bias Correction Instrument

Careful experimental design is necessary to isolate the frequency-dependent iodine transmission, from which the PDA centroid frequency shift, relative to the cw seed frequency, is obtained. The wind bias correction instrument is shown in Fig.5.3. The instrument is composed of three sections: the optical section, the electronics section, and the data-acquisition section, which reads in and processes the electrical signals to yield the pulse-centroid frequency shift. Each of these sections will now be discussed.

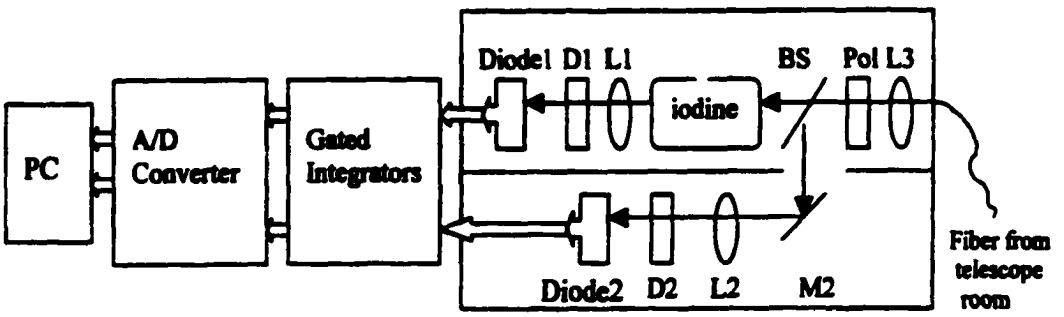

Figure 5.3 Wind-bias correction instrument. A small portion of light transmitted through one beam-steering mirror is collected by a fiber and used by the instrument. In the figure, 1=iodine channel and 2= power-normalization channel, L= lens, D= diffuser, M= mirror, Pol =polarizer, and BS= beamsplitter (where the equals sign means 'represents'). Propagation of light is represented by thin black lines with arrows. Propagation of electrical signals is represented by thick white lines with arrows.

5.4.1 Optical Section:

The small amount of light transmitted by one of the lidar transmitter beam-steering mirrors is used to measure pulsed beam centroid frequency shift. This leakage light is focused into a multi-mode fiber of diameter 1mm, length=10m, and numerical aperture NA=0.116. A diffuser was inserted before the focusing lens to reduce large (up to 50%) pulse-to-pulse fluctuations in light coupled into the fiber. These fluctuations result from random movement of the pulsed beam's center of energy, most likely caused by excessive turbulence in the final dye cell of the pulsed dye amplifier. The diffuser smoothes the beam intensity profile and reduces pulse-to-pulse fiber coupling fluctuations to less than 15% peak-to-peak (as compared to fluctuations of up to 50% without diffusers), resulting in improved measurement stability. Light is coupled by the fiber into the frequency monitor, where it is collimated and split into two channels:

Channel 1: (iodine channel) This channel contains the iodine cell and thus yields the frequency-dependent transmission information.

Channel 2: (power-normalization channel) This channel is used to normalize the iodine channel signal to laser power, which is different for each of the three lidar operating frequencies (Due to imperfect Bragg diffraction efficiency of the acousto-optic frequency-shifting crystals-section 4.1)

A polarizer is inserted before the beam-splitter to eliminate potential changes in splitting ratio due to small changes in polarization of the beam emerging from the multi-mode fiber (White, 1999).

Both beams are focused onto small active area ($0.125mm^2$) fast photodiodes. A diffuser is placed in front of each diode in order to produce large, uniform-intensity beam profiles, thereby minimizing beam-pointing variations incident on the small photodiodes. The inclusion of these diffusers has resulted in elimination of nightly optical alignment of the instrument and reduced pulse-to-pulse fluctuations in diode

voltages to less than 10% (as compared to 15% with only the diffuser in front of the fiber present).

5.4.2) Electronics Section:

The voltages produced by the amplified photodiodes are (Fig. 5.3):

$$V_{diode.1}(\nu_i) = P_0(\nu_i) \cdot T_{bs} \cdot T_{optics.1} \cdot T_{I2}(\nu_i) \cdot \Re_{diode.1} + V_{db1} \quad \text{(eq.5.4}$$

$$V_{diode.2}(\nu_i) = P_0(\nu_i) \cdot R_{bs} \cdot T_{optics.2} \cdot \Re_{diode.2} + V_{db2}$$

$$_{bs} \cdot T_{optics.2} \cdot \Re_{diode.2} + V_{db2}$$

where

$P_0(\nu_i)$=power incident on beam-splitter at frequency $\nu_i(\nu_i = \nu_a, \nu_+, \nu_-)$

T_{bs} / R_{bs}=fractional transmission/reflection of the beamsplitter

$$T_{optics.1} = T_{cellwindows} \cdot T_{Lens1} \cdot T_{diffuser.1}$$

$$T_{optics.2} = R_{Mirror2} \cdot T_{Lens2} \cdot T_{diffuser.2}$$

$\Re_{diode}$=Responsivity and gain of photodiode (amps/watt *Diode resistance * gain)

$T_{I2}(\nu_i)$=Iodine cell transmission at frequency $\nu_i(\nu_i = \nu_a, \nu_+, \nu_-)$

V_{db} = Diode bias voltage (subscripts 1,2 denote diode 1, 2)

With the exception of $T_{I2}(\nu_i)$ and $P_0(\nu_i)$, all of the terms in eq.5.4.1 are frequency-independent over the relatively small (1.26 GHZ) range of CSU lidar operating frequencies. The voltages produced by the two diodes are background-subtracted and power-normalized by the PC software and ratios of the I_2 channel signals at the three operating frequencies are then taken in order to isolate $T_{I2}(\nu_i)$. This will be discussed in the data-acquisition part of this section.

The amplified diode pulses of FWHM ~7ns and amplitudes adjusted by neutral density filters (ND's) to between 200-400mV for both channels are routed along coaxial cables to gated integrators. The pulses are AC-coupled to the integrators by RC high-pass filters (10KHz cutoff frequency) to eliminate undesired dc and low-frequency noise introduced by the AC line voltage and diode circuitry. The filters are internal to the gated integrators (Stanford Research Systems-Model SR245) and are selected via a front-panel switch. The gated integrators integrate the area under the pulse to produce DC voltages

$$V_i = \frac{1}{T} \cdot \int_0^T v_i(t)dt + V_{i,offset} \qquad \text{(eq. 5.4.2)}$$

where

i signifies $v_i (v_i = v_a, v_+, v_-)$

T=integration time of gated integrator (user-adjusted to ~20-25ns)

$V_{i,offset}$ is the offset voltage induced at frequency v_i by the integrator (not to be confused with the photodiode offset voltage)

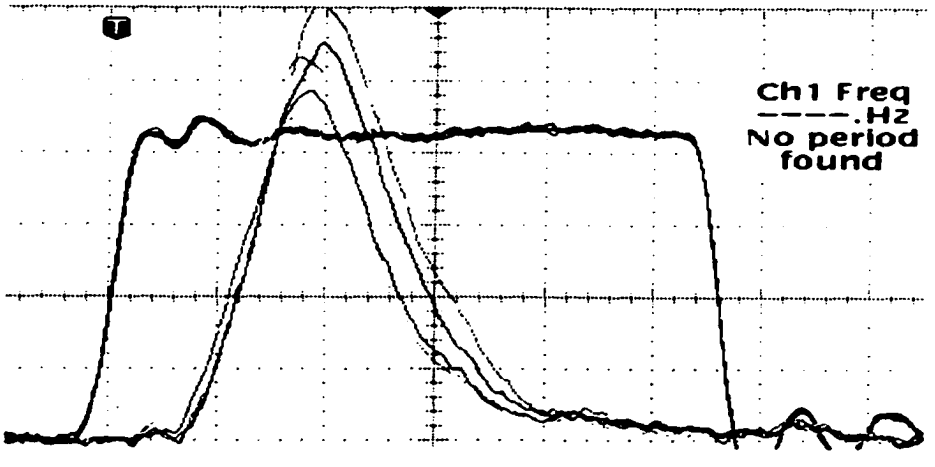

Figure 5.4 Oscilloscope image of integrator gate overlap with pulses from fast photodiode. The oscilloscope settings are 4ns/div (horizontal) and 50mV/div(vertical). The integration time in figure is thus ~23s.

The integrated pulse is proportional to the intensity of the pulse incident on the photodiode (and much easier to measure than the peak height of a nanosecond-scale pulse). Each integrator is triggered by the Q-Switch Sync pulse and has an adjustable delay time (of the gate with respect to trigger pulse) used to overlap the gate with the fast photodiode pulse (Fig 5.4). The gated integrators are also triggered once between arriving light pulses so that the computer (PC) can read the integrator offset voltage $V_{i,offset}$ (with no light present) and subtract it from the total signal V_i. The DC voltages from the integrators are then digitized by an A/D converter, read by the computer and software-processed. It should be noted that the integrators, while providing a simple means of measuring fast pulses, can introduce complications and errors, which will be discussed in section 5.5.

5.4.3) Data-Processing Section:

Twelve voltages are alternately read by the PC and processed. These consist of the pulse voltages at each of the three operating frequencies for both channels (six total) and the associated background voltages read between pulses. From these, we determine the frequency-dependent $T_{I2}(\nu_i)$ in eq. 5.4.1, and compare this to the calibration curve to obtain the PDA centroid frequency shift, relative to the cw seed frequency.

The offset voltages are accounted for by subtracting the measured background-level signals from each of the six integrated pulse voltages. This is performed by software on a pulse-to-pulse basis. The six background-subtracted, integrated voltages are then summed and averaged over each two-minute file (2000 pulses for each frequency). To eliminate effects due to frequency-dependent laser power, the three iodine channel signals are each divided by the corresponding power-normalization channel voltage. The 12 signals have thus been reduced to three background-subtracted, power-normalized voltages (at ν_i=0, +630MHz, -630MHz). To eliminate the effects of all frequency-independent terms in eq. 5.4.1 (beamsplitter and lens

transmission), which are different for the two channels, some ratio of the three signals is necessary. Equation 5.4.1 is then reduced to

$$\frac{T_{I2}(\nu_i)}{T_{I2}(\nu_j)} = \frac{\overline{(V_{diode,1}(\nu_i) - V_{offset,1}(\nu_i))} \Big/ \overline{(V_{diode,2}(\nu_i) - V_{offset,2}(\nu))}}{\overline{(V_{diode,1}(\nu_j) - V_{offset,1}(\nu_j))} \Big/ \overline{(V_{diode,2}(\nu_j) - V_{offset,2}(\nu_j))}} \qquad \text{(eq.5.4.3)}$$

The bars over the quantities symbolize file-averaged quantities. It is thus seen that any ratio will, in principle, isolate the frequency-dependent I_2 transmission. For practical reasons discussed in section 5.3, the ratio

$$R = \frac{T_{I2}(\nu_-) - T_{I2}(\nu_a)}{T_{I2}(\nu_-) + T_{I2}(\nu_a) - 2 * T_{I2}(\nu_+)} \qquad \text{(eq.5.4.4)}$$

was chosen. This ratio is then compared to the calibration curve, which produces a file-averaged shift of the PDA frequency centroid, relative to the cw seed frequency. This shift is then combined with those computed from other two-minute files to form an average frequency shift over the lidar integration period (usually one-hour). The average frequency shift is converted to an instrument-induced radial wind bias (eq. 5.1.2), which the analysis program subtracts from the radial wind profile computed for the integration period, producing a corrected wind profile.

5.5) Lidar Wind Measurement Error Sources and Uncertainties

Due to the experimental complexity of the lidar temperature and wind measurement and associated radial wind-bias correction, many sources of uncertainty exist. Major sources include photon noise, uncertainties associated with wind-bias correction instrument calibration, and laser-locking uncertainties. While many of these uncertainties can be quantified, it is extremely difficult to determine the composite effect of all sources. The most accurate method, used periodically by the CSU lidar group, is the vertical wind measurement. As stated in chapter 2, the hourly-averaged vertical wind is only a few cm/s. Measurement of the vertical wind is used to

estimate composite radial wind measurement error. These measurements have revealed that, after wind-bias correction, vertical wind-bias (i.e the composite radial velocity error) is much smaller than the sum of the uncertainties. This indicates that many of these uncertainties must either cancel one another or else that the uncertainties have been calculated pessimistically. Sources of uncertainty in the wind-bias correction instrument are discussed first. Other sources of uncertainty present in lidar wind measurements will then be summarized. Vertical wind measurements and associated wind-bias correction will be discussed in section 5.6. Temperature measurement uncertainty is dominated by photon noise. Estimates will be given for this in section 5.7.

5.5.1 Wind-Bias Correction Instrument Uncertainties

Uncertainties in the wind-bias correction instrument arise primarily from the calibration curve used to generate the ratios and to a lesser extent, the electronics used to convert fast laser pulses to ratios. The uncertainties are discussed in this section.

Two possible types of errors exist in calibration curves generated by the spectroscopy discussed in section 5.3:

1) Errors in the functions and fundamental assumptions used to generate the calibration curve.

2) The generated curves are correct but experimental conditions (laser parameters, cell temperature) have changed since the calibration curve was measured, resulting in an incorrect calibration curve.

Since the I_2 pulsed transmission curve closely resembles the I_2cw transmission curve, one might expect that errors in the cw curve would affect the calibration much more than errors in the much narrower PDA lineshape measurement. Errors in the cw curve result primarily from two sources:

1) Long-term temperature drift of the I_2 cell.

2) Errors in frequency-scaling the measured I_2 cw transmission spectrum

Cell temperature determines the I_2 transmission spectrum. Resistance measurements from a thermistor located near the cell wall indicate negligible fluctuations during a given night but long-term temperature drifts of ± 0.3degC over time intervals on the order of months. As a result, the cw transmission spectrum of I_2 is measured monthly and a new calibration curve formed. Curves measured from 10/01 through 5/02 are plotted together in Fig. 5.5(a).

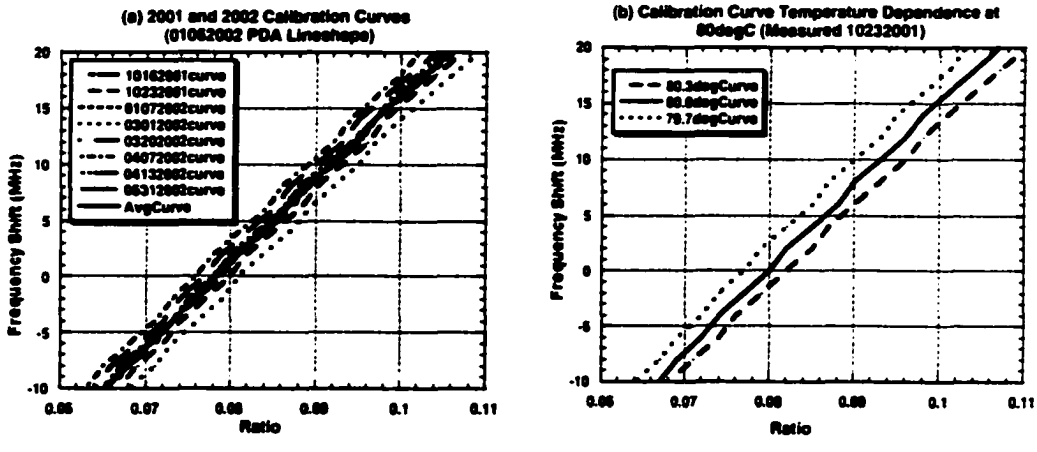

Figure 5.5 (a) Wind-bias instrument calibration curves, measured approximately monthly, from 10/01 through 5/02 for iodine cell temperature of 80°C. All curves use the same PDA lineshape in the figure to isolate the dependence on cw transmission spectrum changes. (b)Sensitivity of the calibration curve at 80°C to small (± 0.3°C) iodine cell temperature changes. (measured on 10/23/01).

The curves in the figure are all generated using the same PDA lineshape to isolate sensitivity of the calibration to cw I_2 transmission parameters. A typical value of the 'Ratio' variable (eq. 5.3.2) is between 0.080 and 0.090. Comparison of the curves plotted in Fig. 5.5(a) reveals a maximum deviation of ± 2MHz from the mean curve. From eq. 5.1.2, this translates into a maximum radial wind error of ± 1.2m/s

PDA lineshape measurements were taken at cw powers similar to those used on a typical night (Fig. 5.6). From the figure, it can be seen that lineshape for the upshifted beam (60mW) is narrower than the other two lineshapes, which are nearly identical. This effect is known as saturation broadening and occurs because the un-shifted and down-shifted beams are saturating the PDA gain medium to a higher degree than the up-shifted beam (Yariv, 1989). This assumption is verified by noting that, for the typical cw input powers given above, the PDA output powers are roughly 1.25W, 1.0W, and 1.0W for the three frequencies on a typical night. This variation in output power is much smaller than the variation in cw input power. Thus, we assume that all three frequencies need to saturate the gain medium.

Now we want to test the accuracy of the use of the same PDA lineshape for all three frequencies in generating the calibration curve. Use of the un-shifted and down-shifted lineshapes produced calibration curves whose radial velocities differ by less than 0.5m/s. Use of the up-shifted beam pda lineshape introduced a change in the calibration curve of 1m/s. In practice, the actual error introduced by using the same lineshape for all three beams is probably less than this, due to the fact that up-shifted beam power is closer to 70mW at the beginning of a typical night. This assumption could possibly introduce larger errors toward the end of a long data campaign, during which cw ring laser power sags considerably.

The reader may wonder why a single lineshape is used in the calibration curve rather than the 'correct' lineshape for each of the three operating frequencies. This approach, while more correct, poses numerous practical difficulties. It would involve computing calibration curves for the wide range of cw input powers present in long data campaigns. Different calibration curves would be required to analyze various parts of the data set. Furthermore, the PDA input power at each of the three operating frequencies would need to be recorded periodically in order to use the correct calibration curve for that time period. These practical difficulties only add to the already labor-intensive task of accurately measuring temperature and winds. Thus, we typically use the lineshape for the unshifted beam, which changes very little over the typical range of un-shifted cw powers (100-140mW) as can be seen from figure

5.6. This assumption is valid if all three cw input beams saturate the PDA dye gain medium.

Electronics-Induced Uncertainty:

It has been a long-standing struggle to achieve performance stability of the wind-bias correction instrument. Pulsed signals from the iodine and normalization diodes were initially sent to the gated boxcar integrators via 10KHz high-pass filters internal to the integrators. The integrator outputs are then digitized by a National Instruments A/D boards, and subsequently read by wind-bias correction instrument software (section 5.4). The performance stability for the wind-bias correction was less than expected. It was felt that there may exist high-frequency noise (> 1 MHz) in the pulsed output from the diodes, since the pulse width is in the order of 7 ns. An external high-pass filter with RC time constant 23ns was then introduced. However, this introduced un-wanted ringing to the pulse, resulting in wind-bias correction being extremely sensitive to setting of the integrator gate (relative to the pulse). Several high-pass filters were placed at the inputs to the gated integrators without success.

It was recently discovered that the 10KHz high-pass filter internally provided by the gated integrator does reject nearly all diode noise, while transmitting the pulse signal faithfully and free of ringing. Furthermore, the lack of performance stability was found to result from a peculiarity associated with the multiplexer design of the National Instruments A/D boards.

The A/D board acquires voltages from pre-selected channels (programmed by software) in a sequential order. The channels are coupled to the A/D converter by a multiplexer, which alternately transmits the pre-selected signals for digitization and subsequent reading by software. A problem peculiar to this board involves discharge of the signal just digitized into the channel about to be digitized (due to multiplexer capacitor discharge), causing an incorrect digitization of the second channel and introducing errors and instability into the wind bias correction. The solution is to

digitize and read in a 'dummy channel', which has only a 50-ohm terminator attached to its input, in between reading integrated iodine and power-normalization channel voltages. The signal from the iodine channel, which had previously leaked into the normalization channel (after being digitized), now leaks into the dummy channel, (whose voltage is read and discarded by the wind-bias correction instrument software) rather than leaking into the normalization channel. This change, combined with insertion of the internal 10KHz high-pass filters at the integrator inputs, has resulted in much greater stability of the wind-bias correction. Vertical wind measurements (section 5.6) have revealed radial wind bias correction to within 1m/s for several nights, permitting the lidar to return to two-beam configuration.

5.5.2) Laser-Locking Uncertainties

A magnified view of the Na Dopplerfree spectrum in the vicinity of the D_{2a} locking point is shown (for typical input power of 140μW) in Fig. 5.7.

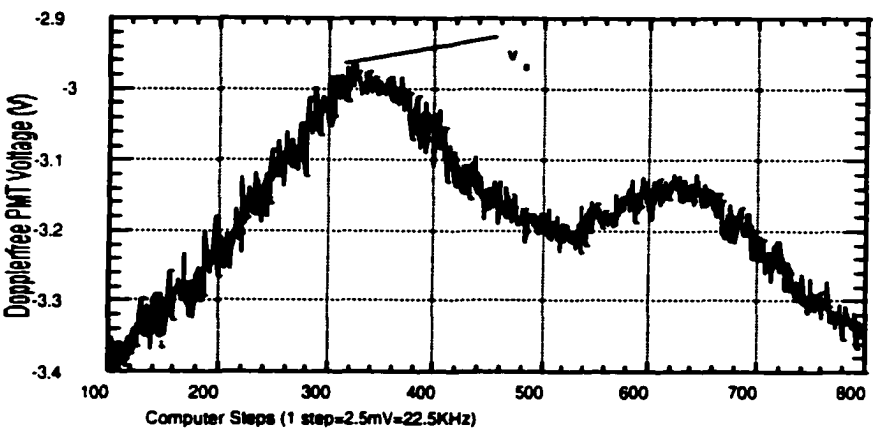

Figure 5.7 Sodium Dopplerfree saturation fluorescence spectroscopy signal near the D_{2a} peak, to which the ring laser is locked. The computer scans the laser, using a 12-bit Digital-to-Analong (D/A) converter with 2.5mV step size (resolution). The spectrum is shown for typical power of 140μW entering the Dopplerfree.

The ring laser is locked to the larger peak during lidar operation. In the figure, the horizontal axis is in units of D/A steps (from the PC which scans and locks the laser to the peak). Each step is equal to 2.5mV (equivalent to 55KHz). This is the resolution of the 12-bit board and is the smallest step size that the D/A output can generate.

The figure is typical of most scans. To calculate locking uncertainty, first note that the peak is located near step 325. If one arbitrarily assumes that the laser could be locked at any position within ~20mV of the peak value (due to noise spikes of amplitudes typically seen in the Dopplerfree spectrum), then the laser could be locked anywhere between steps 300 and 355 for a given file. This gives a full-width of 55steps*(55KHz / step) ≈ 3MHz. Thus we have

$$\nu_{lock} = \nu_{peak} \pm 1.5MHz$$

Now we take into account the fact that the laser is dithered over a 3MHz range. Suppose that the laser is locked at step 355, located 1.5MHz to the right of the peak. To this 1.5MHz locking error, we would need to add $\frac{\nu_{dither}}{2} = 1.5\text{MHz}$. Thus, the largest excursion from the peak would be

$$\nu_{lock} = \nu_{peak} + 1.5\text{MHz} + 1.5\text{MHz} = \nu_{peak} + 3.0\text{MHz} \equiv \nu_{peak} + \Delta\nu_{lock}$$

From this, we obtain the maximum rms locking error of

$$\Delta\nu_{lcok,rms} = 3.0\text{MHz} * 0.707 \approx 2.1\text{MHz}$$

From eq. 5.1.2, this leads to an rms locking uncertainty of 1.25m/s (radial velocity) for a given file. Small spikes seem to occur at random locations near the peak. When hourly averaging of the velocity profiles (~28 per hour) is applied, we obtain an hourly-averaged rms locking uncertainty of $\frac{1.25m/s}{\sqrt{28\,files}} \approx 0.24m/s$.

5.5.3) Photon Noise

Photon noise induced by the process of PMT photon-counting is random and obeys a Poisson distribution. Wind uncertainty due to photon noise is proportional to $N^{-1/2}$, where N is the number of photons counted by the PMT during the integration period. Plots of horizontal wind uncertainty due to photon noise for typical winter and summer night and day conditions are presented in Fig. 5.8. Plots are given for uncertainties associated with integration periods of 6-12 hours (solid lines) and those associated with one-hour integration periods (dashed lines). It can be seen from the figure that uncertainties due to photon noise vary with altitude, season, and even more significantly, from day to night (due to presence of Faraday filter during daytime operation). Photon noise is the dominant source of wind uncertainty for altitudes outside of 85-95km for nighttime measurements and for all altitudes during daytime measurements. It will be shown in section 5.6 that the frequency monitor does not correct for photon noise-induced errors.

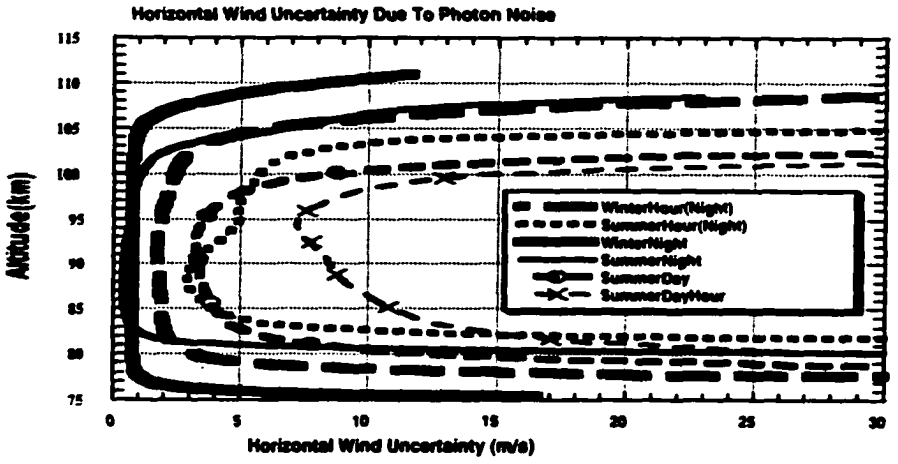

Figure 5.8 Horizontal wind uncertainty due to photon noise for data integrated over a full night (6-11 hours), a full day (6-14 hours) and over one hour. Plots are shown for summer and winter.

The above-mentioned sources are the major sources of uncertainty in the Na lidar wind measurement. Other possible sources have been considered and determined to be negligible in comparison to the above-mentioned sources. A summary of the error

sources is given in Table 5.1. The error due to PDA lineshape changes assumes proper operation of the YAG pump laser. The error due to cw I_2 transmission changes is an upper bound due to timescales on the order of one month or more (since the frequency monitor calibration was last performed).

Table 5.1 Sources of Uncertainty in the Lidar Wind Measurement

Source	Estimate of Resulting Horizontal Wind Uncertainty
Photon noise (1-hour integration time at 90km)	2 m/s (Winter night), 3-5m/s (Summer night), 7-10m/s (Summer day)
Laser locking	0.5m/s (for one-hour integration)
Wind-bias correction instrument calibration curve	2.4 m/s (CW I2 transmission uncert.) 1.0 m/s (PDA lineshape changes) 1.0 m/s (Use of same PDA lineshape for all three frequencies)
Wind-bias correction instrument electronics	<1.0 m/s

Note: Magnitude of horizontal uncertainty is two times radial wind uncertainty for a beam pointed 30° off zenith (eq.4.1.1).

5.6) Vertical Wind Measurements-Assessment of Radial Wind-Bias Correction:

Several nights of vertical wind measurements were performed in Spring 2002, to assess the performance of the wind-bias correction instrument and to measure the composite error in the radial wind measurement. The results from three of these nights, each representing different transmitter conditions, are presented in Fig.5.9.

Solid lines in these graphs represent measured vertical winds before wind-bias correction and the dashed lines represent vertical wind measurements after wind-bias correction. Night 2095 (the 95th UT night of 2002) represents a night with large radial wind bias. Measurements on this night and on night 2098 were both made with a degraded set of YAG laser flashlamps. The wind-bias correction instrument was able to correct for this bias, as seen in Fig. 5.9, to better than 1m/s magnitude. On night 2098, the ring laser was intentionally locked to a neighboring Dopplerfree peak, located -16MHz from the correct locking point, for three hours to test whether the wind-bias correction instrument could correct for incorrect laser locking. The radial bias for this night was approximately 3m/s, with 10m/s bias resulting from the locking error of -16MHz (eq. 5.2.1) and roughly -7m/s bias resulting largely from the degraded flashlamps (-7m/s+10m/s=3m/s). The instrument was able to correct for the locking error (Fig. 5.9). Night 2123 represents a more typical night, characterized by a small (~-1m/s) radial wind bias. This is slightly less than that observed on most nights. The wind-bias correction instrument corrected this small bias for altitudes below 95km but actually introduced more error above 95km. Wind-bias correction would normally not be used on a night similar to this (i.e on a night where the measured radial wind bias is $\leq$1.5m/s) since the combined uncertainties due to photon noise and wind-bias correction instrument uncertainties are at least this amount.

One interesting (and perhaps obvious) feature of Fig. 5.9 is that the wind-bias correction instrument does not correct for velocity errors above ~101km on these nights. Photon noise begins to increase at these altitudes (Fig. 5.8). The instrument cannot correct for uncertainties due to photon noise. It should also be noted that on occasional nights (mostly before recent improvements in wind-bias correction instrument electronics, discussed in section 5.5.1), the instrument only corrected vertical winds to ~1.5m/s magnitudes. From this evidence, the uncertainty in radial wind measurements is placed at < 1m/s for most nights (<1.5 m/s for all nights), resulting in horizontal wind uncertainties of <3m/s. This estimate is for altitudes where uncertainty due to photon noise is not greater than 3 m/s. From Fig. 5.8, it is

seen that limiting altitudes depend on season and are usually located between 100-105km (upper) and 78-83km (lower).

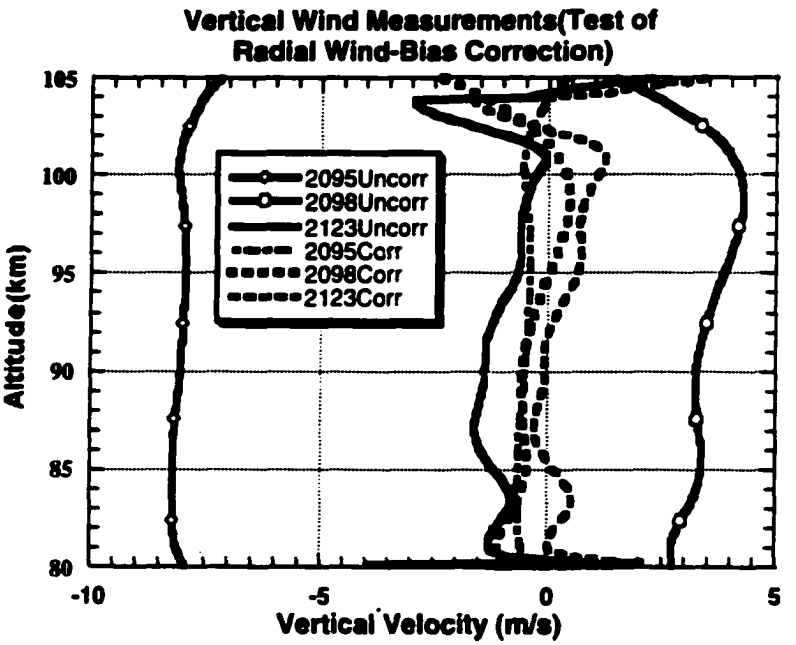

Figure 5.9 Three nights of vertical wind measurements to test wind bias correction (UT nights 95, 98, and 123 of the year 2002). The solid lines denote nightly-averaged uncorrected vertical velocities (formed by averaging the hourly-averaged profiles). The dashed lines are the same vertical velocities, modified by wind-bias correction.

5.7) Uncertainties in the Lidar Temperature Measurement

Uncertainties in the CSU lidar temperature measurement are dominated by photon noise (Fig.5.10), especially at the high and low altitude extremes of the 80-105km range. As with wind uncertainties, temperature uncertainties are greatest during daytime and larger in summer than in winter. A much smaller error source is imprecise frequency locking, which produces a temperature uncertainty of ~0.025 K /MHz locking error.

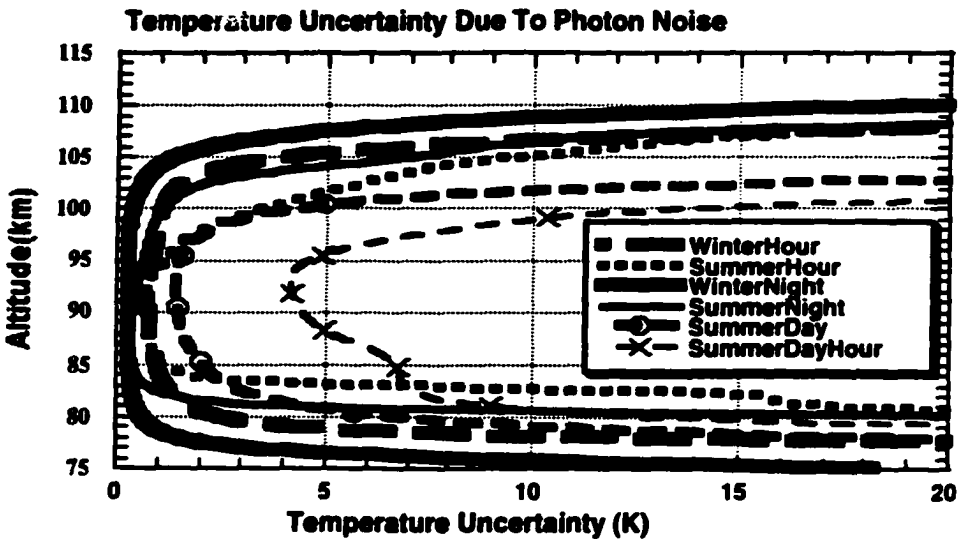

Figure 5.10 Temperature uncertainty due to photon noise for data integrated over a full night (6-11 hours), a full day (6-14 hours) and over one hour. Plots are shown for summer and winter.

Chapter 6-Lidar Data Analysis

Conversion of integrated photon count profiles to temperature and horizontal velocity profiles involves a significant amount of processing. This chapter describes the process. Atmospheric information is obtained by inversion of the lidar equation, which is introduced in section 6.1. Section 6.2 describes the inversion method by which temperature, radial velocity (and then horizontal winds via eq.4.1.1) and sodium density profiles are derived from the backscattered lidar returns. Some pre-processing and bad-file elimination is necessary before inverting the lidar data. These steps are outlined in section 6.3, which also briefly describes the algorithm used in the data analysis program. Program outputs are altitude-resolved temperature, radial velocity, and sodium density profiles from 70-120km. Poor signal to noise ratios at the lower and upper bounds of this range lead to accurate temperature and radial wind (to within 3K and 5m/s) measurements only from 80-105km for most months (Figs.5.8 and 5.10). Altitude and time profiles of temperature, zonal, and meridional winds are presented in section 6.4. These include vertical and time profiles for all winter night hours used in sections 7.1 to 7.3, as well as time profiles at 85km, 91km, and 97km from four summer data sets covering complete diurnal cycles. Harmonic analysis was performed on these results (and on data from several other partial diurnal cycles during the same period) and the results compared with the Global Scale Wave Model. This is discussed in section 7.4.

6.1) The Lidar Equation

The lidar equation relates the number of photons backscattered from a source at altitude z to properties of the scattering atoms and the lidar system. For Na resonant backscattering, the number of photons backscattered and counted from sources located at heights z-Δz/2 to z+Δz/2 due to Na excitation by a laser pulse of energy E is given by

$$N_{na}(z,\nu_L,T,V) = \eta\left(\frac{E(\nu_L)}{h\nu_L}\right)T_{air}^{\,2}T_{na}^{\,2}\left(\sigma_{na}^{\pi}(\nu_L,T,V)\rho_{na}(z,t)\Delta z\frac{A_R}{z^2}\right) \quad \text{(eq.6.1.1)}$$

where η=lidar system efficiency

E=laser pulse energy, centered at frequency ν_L (Joule)

$h = 6.626 \cdot 10^{-34}\ Joule \cdot \sec$ is Planck's constant

ν_L =centroid frequency of the laser pulse

T_{air} =one-way transmission of the atmosphere to height 70km (which marks the beginning of the sodium layer)

$T_{na}(\nu_L, z) = \exp(-\int_{z_L}^{z} \rho_s(z', t)\sigma_{na}(\nu_L, T, V)dz')$ is the one-way transmission from the bottom height z_L of sodium layer (taken to be 70km) to the height z

$\sigma_{na}^{\pi}(\nu_L, T, V)$ =differential Na backscattering cross-section $(m^2 \cdot Sr^{-1})$

$\sigma_{na}(\nu_L, T, V)$ =total Na absorption cross-section (m^2)

Δz=size of range bin centered at altitude z (m)

A_R =area of receiving telescope (m^2)

$\rho_{na}(z, t)$ =sodium density at altitude z (m^{-3})

In eq.6.1.1, the background and noise counts are assumed to have been subtracted by the method described in section 6.3.

In order to intuitively understand the form of eq.6.1.1, it is instructive to look at each of the terms. System efficiency η arises primarily from optical losses induced by non-perfect interference filter transmission (70%), fiber-coupling losses, and the quantum efficiency of the PMT's (15-20%). The first bracketed term is the number of photons in the laser pulse. The term T_{air}^2 represents the attenuation of the beam on the way up to and down from the Na layer. T_{na}^2 accounts for roundtrip attenuation

resulting from Na absorption from sources between altitudes z_L to z. The second bracketed term represents the probability that an upward propagating photon will be resonantly backscattered by Na sources in the range bin Δz centered at altitude z.

In order to obtain atmospheric information via eq.(6.1.1), we will need to make use of the Rayleigh-scattered photons from air molecules (size << λ_L) at heights 20-40km. Transmission of the atmosphere below these altitudes is highly variable and complicated by Mie scattering from aerosols and particulates with sizes comparable to laser wavelength λ_L. Fortunately, ratios can be constructed which cancel out this scattering. The number of collected and counted Rayleigh-backscattered photons from air molecules at height z is given by

$$N_{ray}(z,\nu_L)=\eta\left(\frac{E(\nu_L)}{h\nu_L}\right)T^2{}_{air<20km}\left(\sigma^{\pi}_{ray}\rho_{air}(z,t)\Delta z\frac{A_R}{z^2}\right)\exp(-2\int_{20km}^{z}\sigma_{ray}\rho_{air}(z,t)dz')$$

(eq.6.1.2)

where $\rho_{air}(z,t)$=air density at altitude z (m^{-3})

$$\sigma^{\pi}_{ray}=1.5\cdot\frac{\sigma_{ray}}{4\pi}=6.11\cdot10^{-32}m^2\cdot sr^{-1}=\text{Rayleigh back-scattering cross-section}$$

and $T^2{}_{air<20km}$ =the round-trip transmission through the complicated (by the presence of aerosols) lowest 20km of atmosphere.

The broadband Rayleigh cross-section is independent of frequency over the narrow (1.26GHz) range of Na lidar operating frequencies. The derivation of atmospheric parameters can be greatly simplified if the exponential in eq.6.1.2 can be approximated as one. We make this approximation by setting $\rho_{air}(z,t)$=0 for z>20km. In practice, the small contribution to the integral above 20km is negligible when ratios are taken at the three lidar operating frequencies.

6.2) Inverting the Lidar Equation to Obtain Temperature and Wind Profiles

Equation 6.1.1 contains many frequency-independent terms as well as frequency-dependent laser power which can be eliminated by suitable use of ratios, resulting in experimentally-determined temperature and wind ratios (eq.3.2.3). These ratios can be compared to the theoretically-generated calibration curve to obtain temperature and radial velocity profiles. The first simplification to eq.6.1.1 requires knowledge of Rayleigh-scattered returns at some reference altitude z_{ref} (or summed over a range of altitudes). In the CSU lidar data analysis, 30km is chosen as the reference height. This value was chosen because it is high enough not to be contaminated by aerosol scattering yet low enough that the Rayleigh return is non-negligible. Rayleigh-backscattered photon counts (eq.6.1.2) can be used to normalize N_{na} to the laser power viz

$$\eta T_{air}^{\,2}\left(\frac{E(\nu_L)}{h\nu_L}\right)\left(\frac{A_R\Delta z}{4\pi}\right)=\frac{z_{ref}^{\,2}\cdot N_{ray}(z_{ref},\nu_L)}{\rho_{air}(z_{ref},t)\sigma_{ray}} \qquad \text{(eq.6.2.1)}$$

Substituting eq.(6.2.1) into the lidar equation 6.1.1 results in the equation

$$\frac{N_{na}(z,\nu_L,T,V)}{N_{ray}(z_{ref},\nu_L)T_{na}^{\,2}}=\sigma^{\pi}{}_{na}(\nu_L,T,V)\left(\frac{z_{ref}^{\,2}\,\rho_{na}(z,t)}{z^2\rho_{air}(z_{ref},t)\sigma_{ray}}\right) \qquad \text{(eq.6.2.2)}$$

The bracketed term on the right-hand side of eq.6.2.2 has no frequency dependence and cancels out when inserting $\sigma^{\pi}{}_{na}$ into the temperature and velocity ratios R_T and R_v (eq.3.2.3), resulting in

$$R_T=\frac{\sigma^{\pi}_{na}(\nu_+)+\sigma^{\pi}_{na}(\nu_-)}{2\sigma^{\pi}_{na}(\nu_a)}=\frac{\dfrac{N_{na}(\nu_+)}{N_{ray}(z_{ref},\nu_+)T_{na}^{\,2}(\nu_+)}+\dfrac{N_{na}(\nu_-)}{N_{ray}(z_{ref},\nu_-)T_{na}^{\,2}(\nu_-)}}{2\cdot\dfrac{N_{na}(\nu_a)}{N_{ray}(z_{ref},\nu_a)T_{na}^{\,2}(\nu_a)}}$$

$$R_V = \frac{\sigma_{na}^{\pi}(\nu_+) - \sigma_{na}^{\pi}(\nu_-)}{\sigma_{na}^{\pi}(\nu_a)} = \frac{\dfrac{N_{na}(\nu_+)}{N_{ray}(z_{ref},\nu_+)T_{na}^{\,2}(\nu_+)} - \dfrac{N_{na}(\nu_-)}{N_{ray}(z_{ref},\nu_-)T_{na}^{\,2}(\nu_-)}}{\dfrac{N_{na}(\nu_a)}{N_{ray}(z_{ref},\nu_a)T_{na}^{\,2}(\nu_a)}} \qquad \text{(eq.6.2.3)}$$

Temperature and radial winds at altitude z can thus be solved iteratively, given backscattered sodium counts at altitude z, Rayleigh-scattered returns from some reference height z_{ref}, and Na layer transmission from lower bound z_L of the layer up to altitude z. In practice, Rayleigh returns from the altitude range 20-40km are summed rather for use in eq.6.2.3 rather than used from a single reference level.

In order to calculate T and V above the first altitude bin (where $T_{na}=1$ for all three lidar frequencies) of the sodium layer, we need to know sodium density $\rho_{na}(z,t)$ for all bins leading up to the calculated bin (so that $T_{na}(z)$ can be determined, via eq.6.1.1. Equation 6.2.2 can be solved for $\rho_{na}(z,t)$ using one of the three lidar operating frequencies

$$\rho_{na}(z,t) = \frac{N_{na}(z,\nu_L)\rho_{air}(z_{ref},t)\sigma_{ray}z^2}{N_{ray}(z_{ref},\nu_L)\sigma_{na}^{\pi}(\nu_L,T,V)T_{na}^{\,2}(z,\nu_L)z_{ref}^{\,2}} \qquad \text{(eq.6.2.4)}$$

In eq.(6.2.4), N_{na} and N_{ray} are measured, σ_{ray} is known, z_{ref} is chosen as 30km (section 6.2) and we use (Yu,1994) $\rho_{air}(z=30km) \cong 3.8278 \cdot 10^{23}/m^3$ (from the tabulated standard atmosphere-COSPAR,1976)

Equations 6.2.3 and 6.2.4 are solved iteratively to obtain altitude-resolved temperature, radial velocity, and sodium density profiles from 70-120km. The 1st bin of the Na layer is chosen as z=70km. At the first bin, $T_{na}=1$ for all three frequencies (by definition). Temperature and wind ratios are obtained from the Rayleigh-normalized photon counts via eq.(6.2.3). The measured ratios are compared to the ratios from the theoretically-generated calibration curves to obtain T and V for the 1st bin. If the measured ratios fall between grid lines (Fig. 3.3) of the calibration curves,

a Taylor expansion is performed using values at the boundary grid lines. Once T and V are known for the first bin, the backscattering cross-section can be computed via eq.(3.2.1). We then use eq.(6.2.4) to obtain $\rho_{na}(z_{1stbin}, t)$, which is then used to compute the transmission of the Na layer up to the second bin. Once this is known, the measured sodium backscattering from the 2nd range bin and the Rayleigh returns from 20-40km are used to calculate R_T and R_V for the second bin. This process is iterated upward until altitude-resolved profiles of T,V, and ρ_{na} are obtained for the entire sodium layer (70-120km).

6.3) Data-Processing Algorithm

Each two-minute raw data file contains four columns: one containing bin altitudes and one column containing altitude-resolved photon counts at each of the three lidar operating frequencies. Results for a typical 2-minute file are shown in Fig.4.7. Before integrating and processing the data, the analysis program (written by Dr. David Krueger of CSU) performs several tests to eliminate bad files, which could contaminate the data. The remaining files for each integration period are then summed by bin and frequency to form a composite profile, which is processed to yield temperature, wind, and sodium density profiles for the integration period. This section outlines the steps by which these functions are performed.

6.3.1) Pre-Processing and Bad-File Selection:

The counts from the sodium layer (70-120km) and Rayleigh scattering region (20-40km) are summed for each frequency. Several diagnostic tests are performed on the sums, including trend tests, ratio tests, and minimum count tests. Trend tests compare layer counts (and Rayleigh counts) at each frequency to mean counts of the three files on either side and discard files whose counts differ by more than some reasonable predefined amount (usually around 20%) from the mean. Ratio tests compute layer temperature and velocity ratios, eliminating any files producing physically-unrealistic values. Minimum count tests eliminate files not meeting a minimum acceptable signal level, avoiding contamination of the data from files with

poor signal-to-noise characteristics. Tests can also be invoked to assure that background counts do not exceed user-defined values. The criteria used in these tests are contained in a user-defined criteria file, which is read by the analysis program. Tests to be performed are set by flags in the analysis program. These tests assure that bad files, which can arise from clouds, loss of laser-frequency locking, a stray trigger pulse, or other error-inducing mechanisms, do not contaminate temperature, wind, and density data.

6.3.2) Integration and Background Subtraction:

Files satisfying all diagnostic criteria for the integration period are summed (integrated) by range bin (150m bin size for mesopause altitudes) and frequency to form a composite vertical profile of photon counts at each of the three operating frequencies. The analysis program computes hourly-averaged (one-hour integration period) and nightly-averaged (one night integration period, although during daytime operation this refers to integration over the day) profiles. The first processing step on each composite profile involves background-subtraction. Average background is computed from altitudes (120-150km) located too high to contribute to detected Rayleigh or sodium backscattering. Average background over this height range (per unit altitude bin) is then subtracted from the counts in each altitude bin. This eliminates data contamination from solar, lunar, and electronic background levels.

6.3.3) Rayleigh Normalization:

The data analysis algorithm utilizes Rayleigh scattering from heights 20-40km for three purposes: power normalization, subtraction of small Rayleigh scattering contributions from high altitudes, and sodium density determination.

Power normalization is used to account for differences in transmitter power and transmission through the varied lower 20km of atmosphere between the three operating frequencies. The background-subtracted photon count profiles at each operating frequency are normalized to the corresponding Rayleigh-scattering sum from 20-40km altitudes. The Rayleigh sum is chosen as a normalizing factor rather

than the scattering from a single altitude in order to minimize uncertainty introduced by the normalization process.

Rayleigh returns from 25-35km are then used in conjunction with a theoretical relative Rayleigh scattering profile computed using $\rho_{air}(z)$ from the 1976 U.S Standard Atmosphere. Measured Rayleigh returns are first fit to the theoretical Rayleigh formula $\frac{A_0}{z^2}\exp(-A_1 z)$ to determine the fitting parameters A_0 and A_1. The value $N^{Rav}(z_{ref} = 30km)$ is computed from this formula and used to calculate sodium density (section 6.2). The derived relative Rayleigh profile is then normalized to this value and the normalized Rayleigh values at each altitude in the Na layer (70-120km) are subtracted from each bin. This process eliminates small Rayleigh scattering contributions induced to temperature and wind measurements near the bottom of the Na layer.

6.3.4) Smoothing and Calculation of T and V Ratios

Background-subtracted, Rayleigh-normalized profiles at each of the three operating frequencies are then smoothed using a Hanning window with FWHM 49 bins for 3.7km vertical resolution (or 31 bins for 2km resolution). These smoothed photon count profiles used in the ratios R_T and R_V (eq.6.2.3 and 6.2.4) to obtain altitude-resolved temperature, wind, and sodium density profiles for the integration period (hour, night, or user-specified period).

6.3.5) Wind-Bias Correction

The twelve voltages (section 5.4.3) necessary to compute the wind-bias correction ratio (eq.5.3.2) for each two-minute data acquisition period are saved to a tab-delimited text file. The data analysis program uses the twelve values to compute radial wind-bias (via eq. 5.3.2, eq. 5.3.3 and eq.5.12) for each two-minute data file. Biases are then subject to bad file tests, similar to those discussed in section 6.3.1. Files passing all tests are summed and averaged over the integration period to form

an average radial wind-bias. This is subtracted from the average (over integration period) radial velocity.

6.4) Sample of Measured Temperature and Wind Profiles

The CSU lidar capability of simultaneously measuring temperature and both horizontal wind components significantly enhances geophysical information derivable from the data. In addition to nightly, monthly, and seasonal temperature and wind averages used for ongoing climatology studies, atmospheric stability and temperature/wind tidal studies are also suitable topics using lidar-acquired data. This section presents a sample of hourly and nightly-averaged temperature, wind, and sodium density profiles from 80-105km, in addition to time profiles at fixed altitudes.

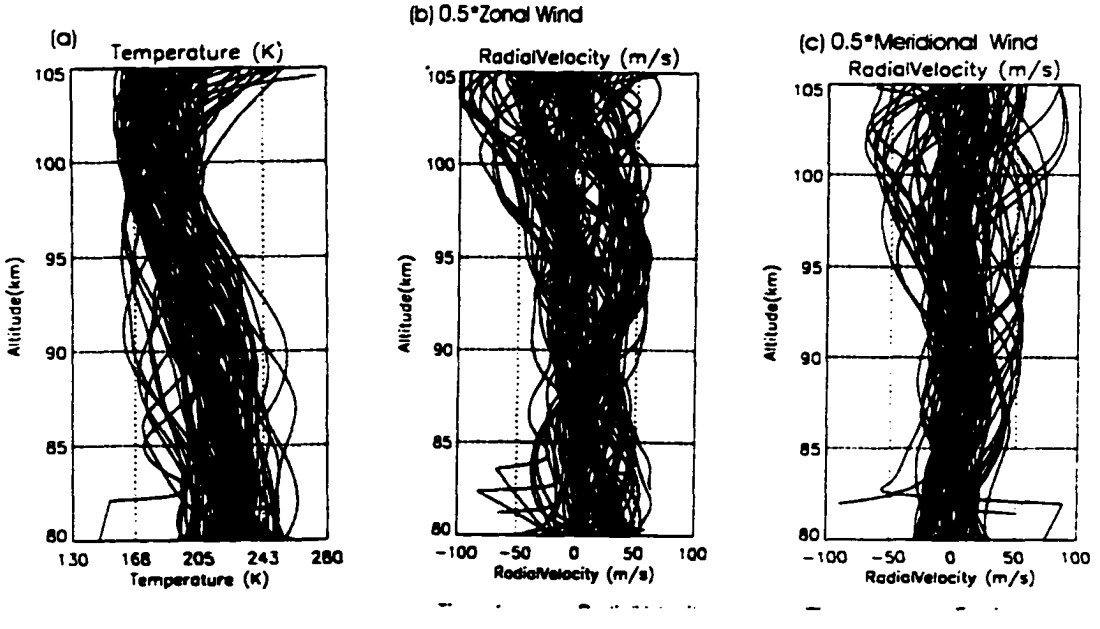

Figure 6.1 Winter 2002 hourly (a) temperature, (b) zonal wind, and (c) meridional wind profiles (70 hours) above Fort Collins, CO. The wind profiles are actually radial velocity measurements and thus need to be multiplied by two to yield the zonal and meridional wind magnitudes. The profiles have 2.1km vertical resolution.

The data analysis program computes (among other things) temperature, wind, and density profiles for each hour. These profiles can be superimposed to form what are

called 'noodle plots'. Temperature and wind noodle plots for 70 winter hours studied in sections 7.1-7.3 are shown in Fig.6.1(a)-(c). These plots clearly demonstrate atmospheric variability. Sodium density measurements, while useful in gravity wave studies, are not studied in this dissertation.

Nightly-averaged (one-night integration period) temperature, wind, and sodium density profiles for representative winter and summer conditions are shown in Fig. 6.2. Since both beams measure temperature and sodium density, large differences between nightly-averaged temperatures and densities derived from the two beam measurements can signify instrumental problems in one of the receiving channels. At 100km, the beams are spaced by ~70km so differences are expected. Nevertheless, both channels are expected to yield similar temperature and density profiles, when integrated over a sufficient time period (one night) to smooth small-scale gravity wave effects.

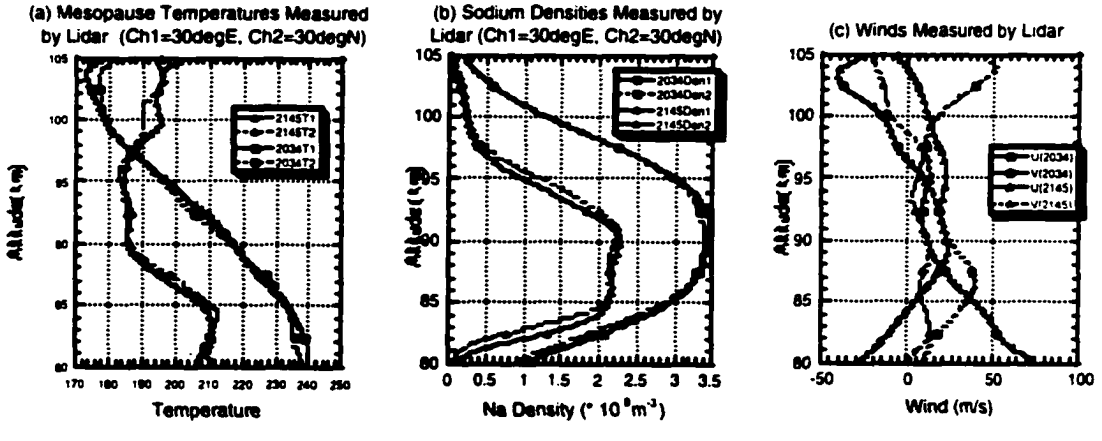

Figure 6.2 Nightly-averaged (a) temperature, (b) sodium density, and (c) horizontal wind (u=zonal, v=meridional) profiles for typical winter (night 2034, denoted by circles) and summer (night 2045, denoted by triangles) 2002 lidar measurements. In the plots, quantities measured by east-pointing ch1 are solid lines and those measured by north-pointing ch2 are dashed lines. The number 2034 denotes the 34th day of the year 2002. In the profiles, channel 1 (2) points 30°East (North) of zenith.

It is seen in Fig. 6.2(b) that temperatures measured by the two lidar channels agree to within a few degrees for both nights, the larger deviations occurring at altitudes with lower signal to noise ratios (Fig. 5.10). Inspection of Fig. 5.10 reveals that these small differences are within photon noise error bars. Measured sodium densities (Fig. 6.2(b)) show similar behavior for both channels. The magnitudes at a given altitude can differ by up to ~25%. However, the measured column sodium abundance (the number of Na atoms in a $1m^2$ cylinder along the beam path extending from 70 to 120km) agrees to within approximately 2% for both nights. Based on Fig. 6.2(a)-(b), we can assume that instrument discrepancies between the two channels most likely contribute very small errors to the wind measurement, as compared to photon noise.

Much useful information is obtained by examining temperatures and winds over long time periods at fixed altitudes. Time profiles are shown at 85km, 91km, 97km, and 103km for all seven winter nights (Fig. 6.3-6.4) studied in sections 7.1 to 7.3. Figures 6.5 to 6.8 contain summer time profiles at 85km, 91km, and 97km for the four days during which measurements were conducted over full diurnal cycles. (Strictly speaking, the day 2145-2146 is missing three hours due to clouds but is nevertheless included). These measurements are part of a 22-day (232-hour) campaign from May 22-June 12, 2002, whose results have been studied and compared (section 7.4) with tidal amplitudes and phases predicted by the Global Scale Wave Model (Hagan, 1995). These profiles reveal the importance of atmospheric waves to thermal and dynamical mesopause structure. Photon noise uncertainties (calculated by lidar analysis program) are plotted as error bars in all profiles (Fig. 6.3- Fig. 6.8). Vertical resolution is 2.1km for winter plots (Fig. 6.3- Fig. 6.4), 3.7km for summer night profiles, and 7.4km for summer daytime profiles (Fig. 6.5 -Fig. 6.8).

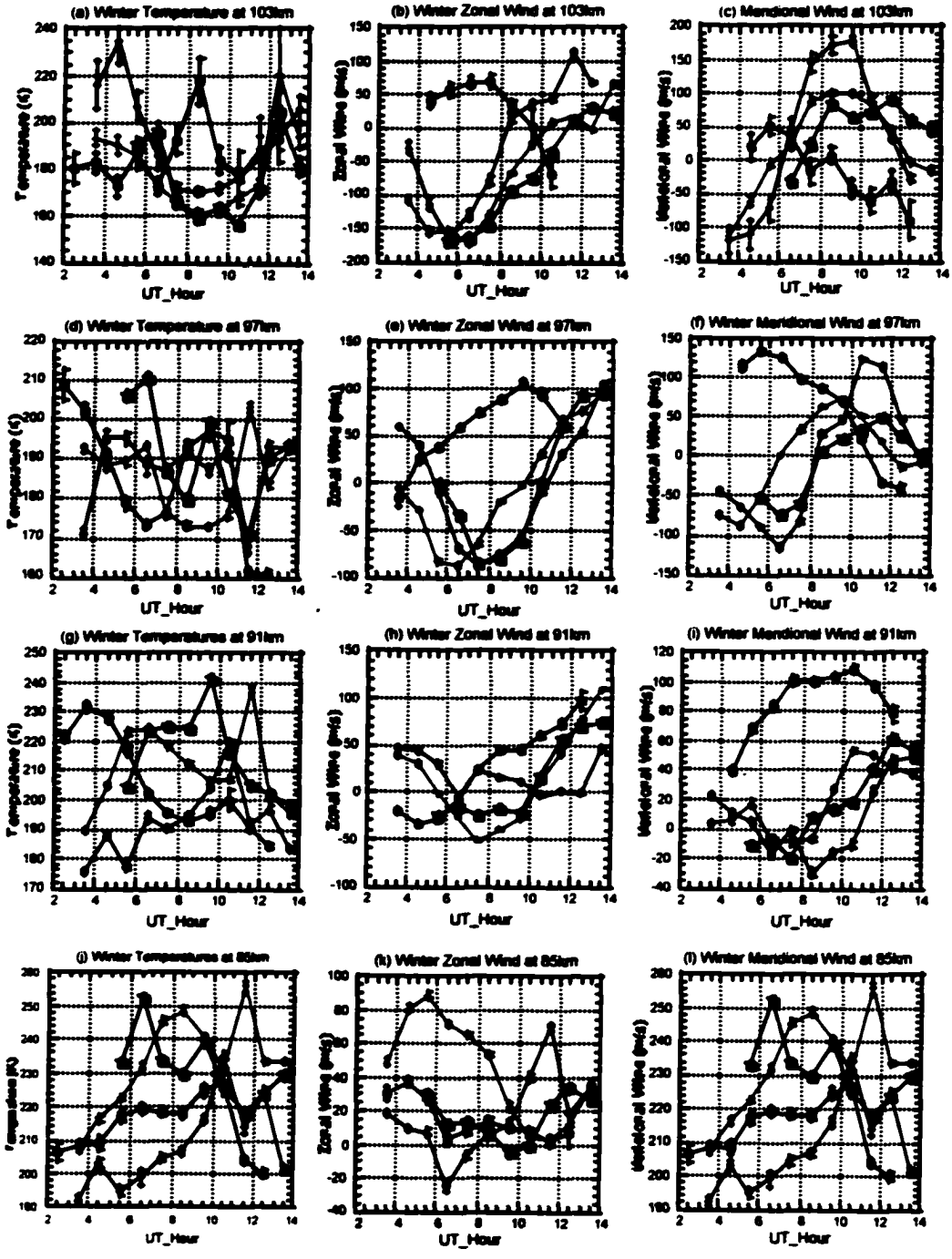

Figure 6.3 Plots of winter temperatures, zonal, and meridional winds at 85km, 91km, 97km, and 103km for nights 2027(black-circles), 2032 (blue-diamonds), 2034 (red-triangles), and 2035 (green squares).

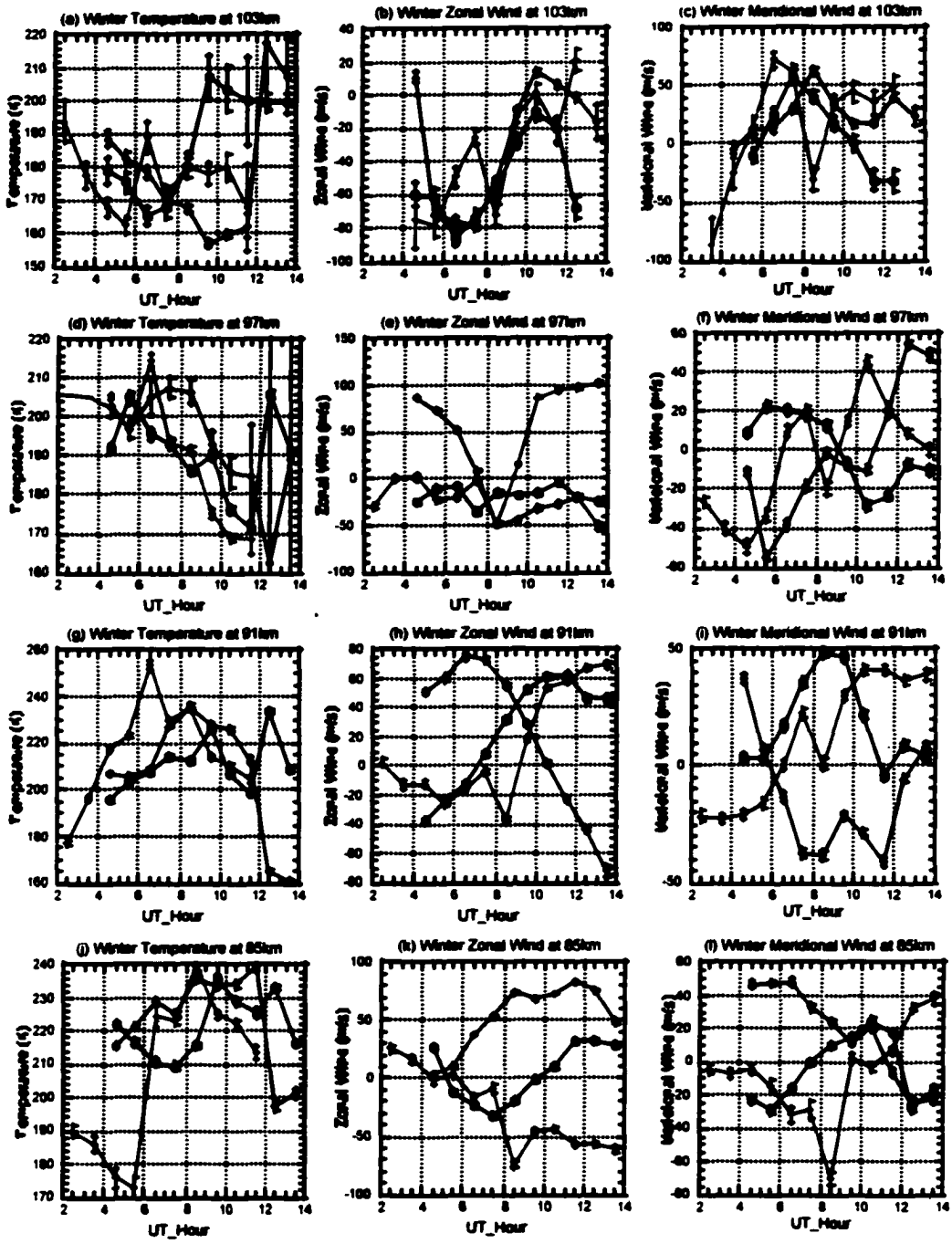

Figure 6.4 Plots of winter temperatures, zonal, and meridional winds at 85km, 91km, 97km, and 103km for nights 2037 (black-circles), 2038 (blue-diamonds), and 2046 (red-triangles).

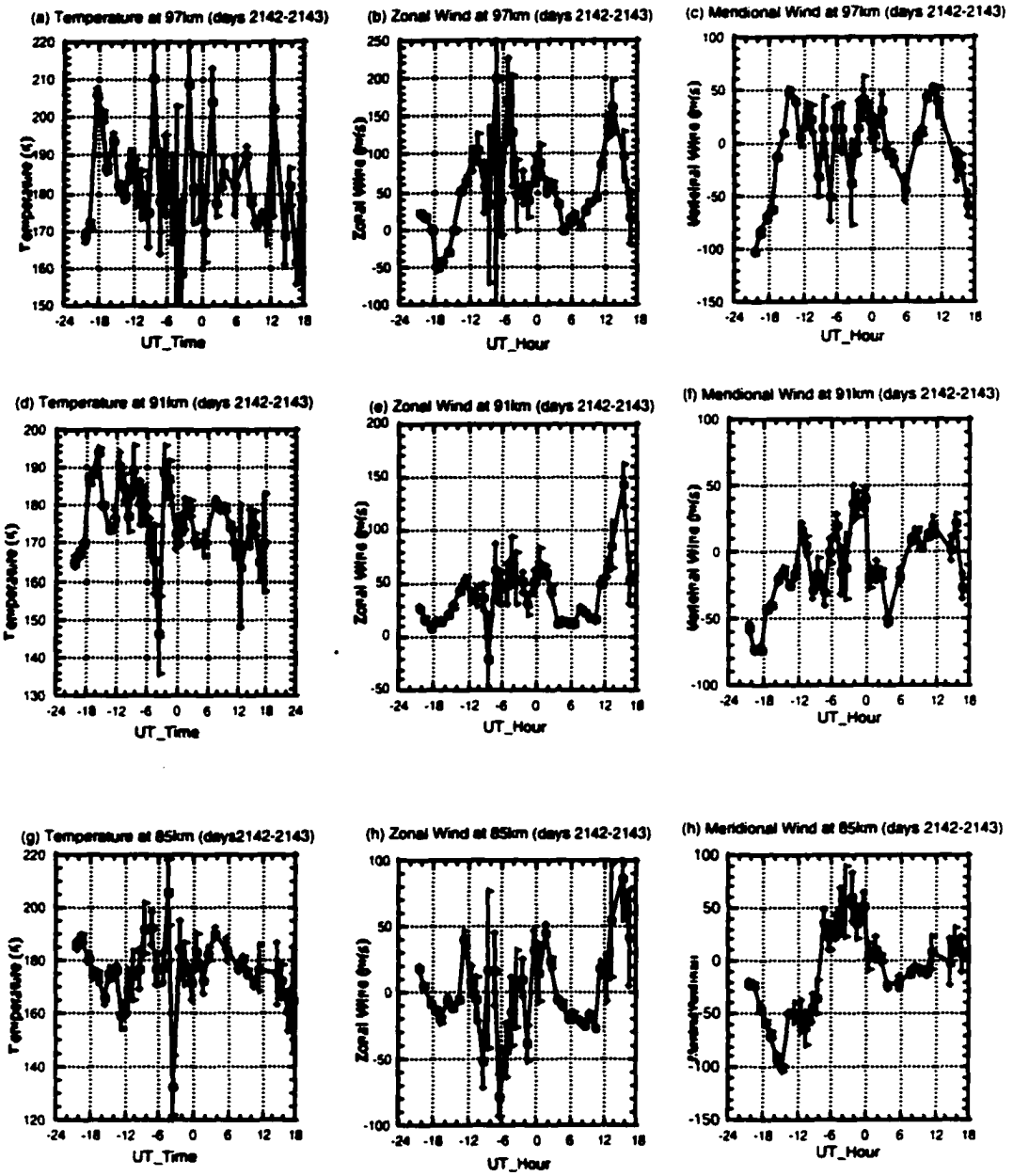

Figure 6.5 Plots of temperature, meridional, and zonal winds at 85km, 91km, and 97km for days 142 and 143 of the year 2002. Horizontal axis is in UT hours (MDT+6hours for this data period). Times are wrapped around 24-hours in order to continuously plot the data. For example, hour -6 is the same as hour 18.

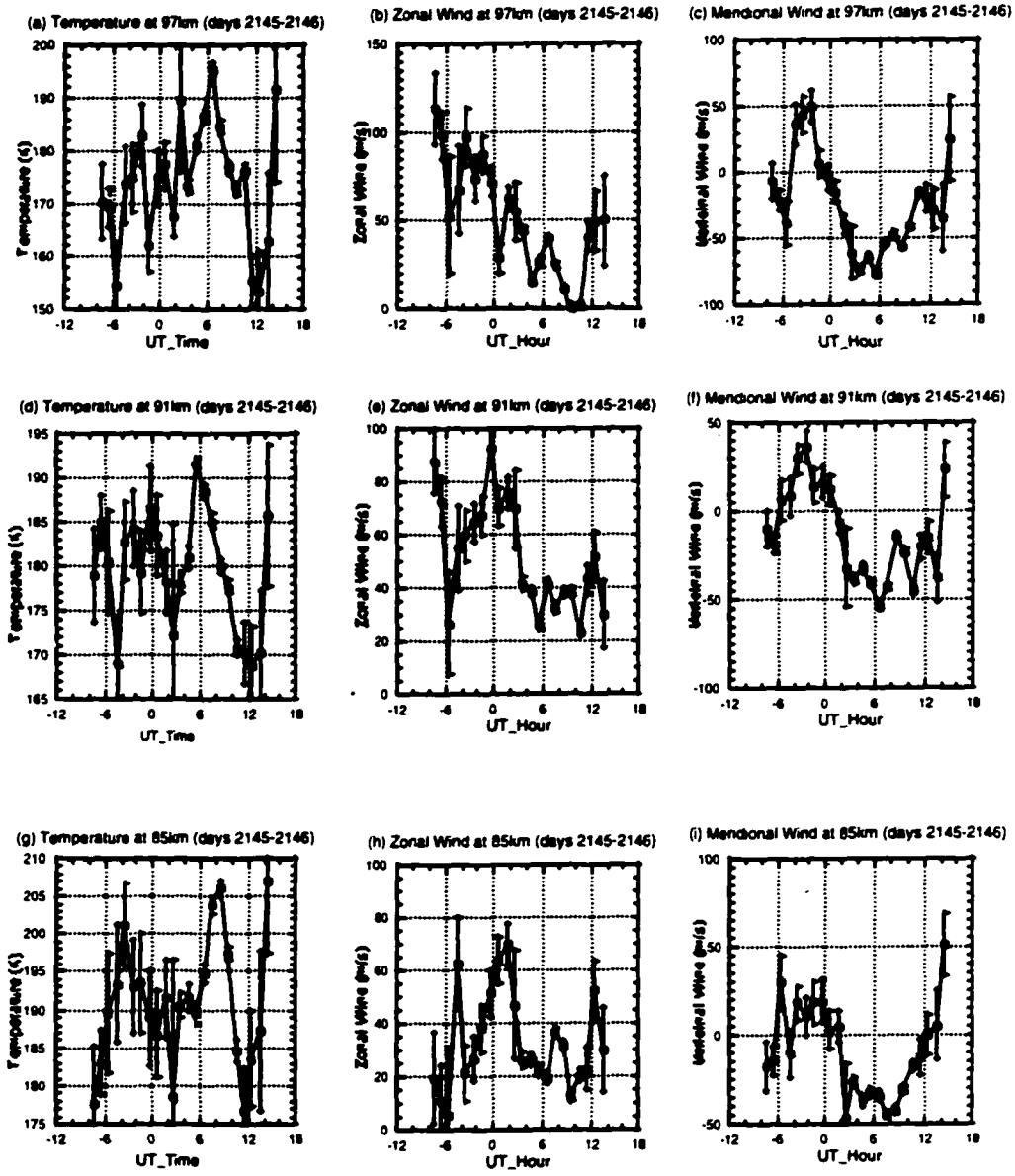

Figure 6.6 Plots of temperature, meridional, and zonal winds at 85km, 91km, and 97km for days 145 and 146 of the year 2002. Horizontal axis is in UT hours (MDT+6hours for this data period). Times are wrapped around 24-hours in order to continuously plot the data. For example, hour -6 is the same as hour 18.

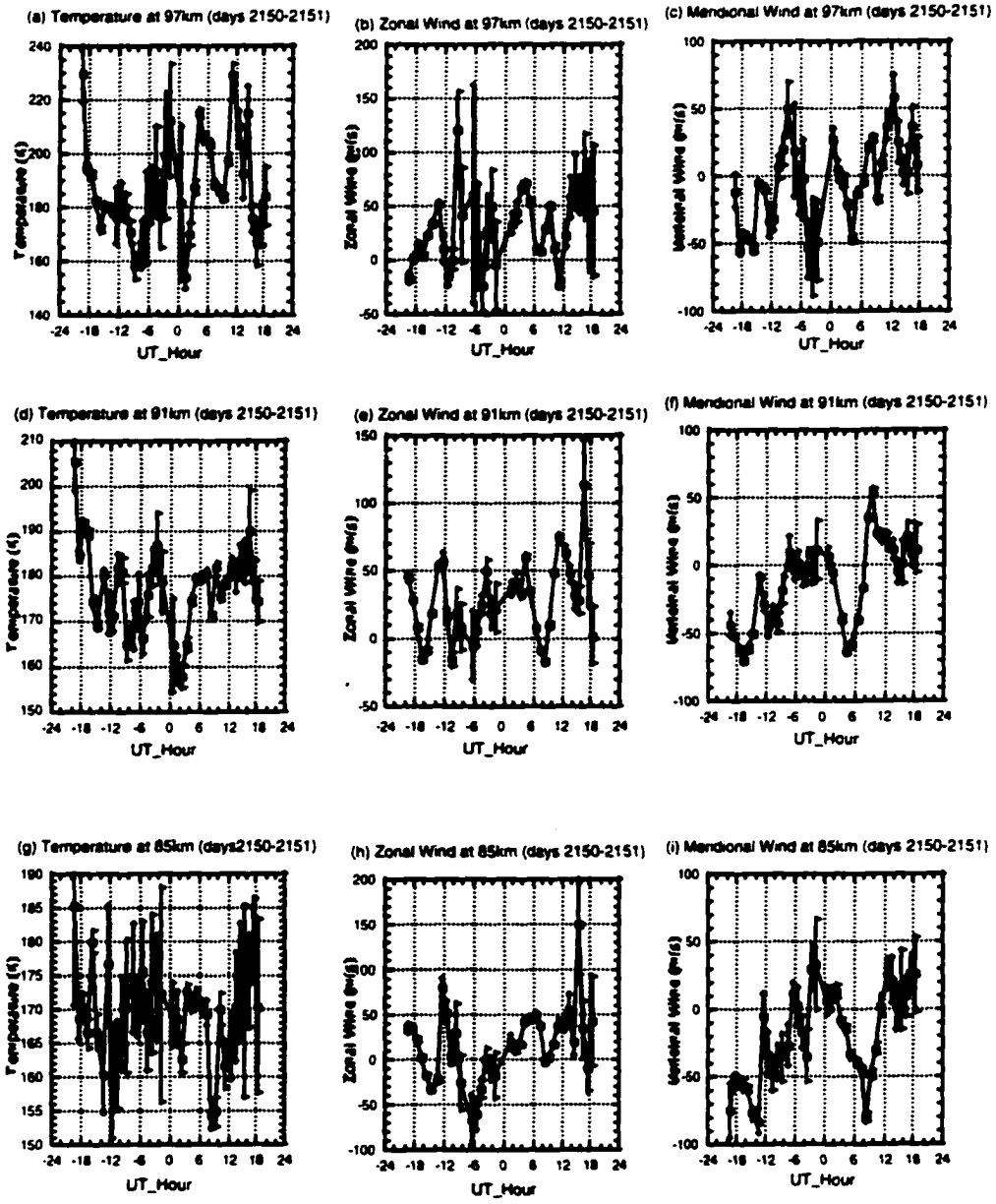

Figure 6.7 Plots of temperature, meridional, and zonal winds at 85km, 91km, and 97km for days 150 and 151 of the year 2002. Horizontal axis is in UT hours (MDT+6hours for this data period). Times are wrapped around 24-hours in order to continuously plot the data. For example, hour -6 is the same as hour 18.

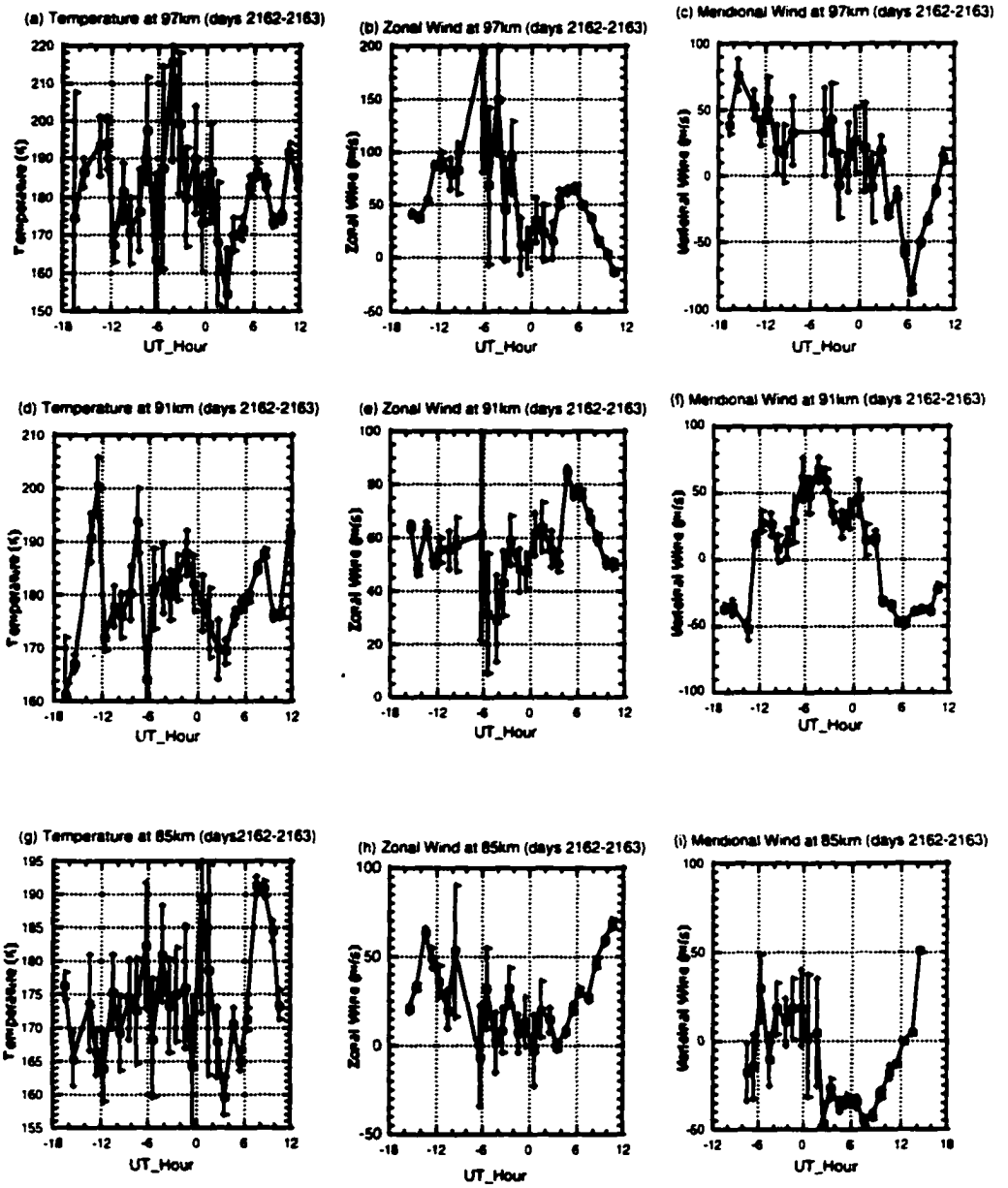

Figure 6.8 Plots of temperature, meridional, and zonal winds at 85km, 91km, and 97km for days 162 and 163 of the year 2002. Horizontal axis is in UT hours (MDT+6hours for this data period). Times are wrapped around 24-hours in order to continuously plot the data. For example, hour -6 is the same as hour 18.

Chapter 7 - Geophysical Parameters Obtained from Two Seasons of Simultaneous Temperature, Zonal, and Meridional Wind Measurements

Many geophysically-significant parameters can be derived from simultaneous measurement of temperature and horizontal winds. This chapter examines some of the results from 172 hours of nighttime observations and four campaigns over full diurnal (24-hour) cycles. The nighttime results, composed of 70 observation hours during the period January 26-Feb 15, 2002 and 102 hours during the period May 22-June 12, 2002, will be presented in the first three sections. The two periods will be referred to as winter and summer, despite the fact that these data sets cover only partial seasons. Long-term mesopause region temperatures, as well as temperature and wind climatology studies are an important part of CSU lidar research. Mean temperature and wind results from these nighttime data sets will be presented in section 7.1 and compared with those predicted by the TIME-GCM (Thermosphere, Ionosphere, Mesosphere, and Exosphere Global Climate Model; Roble et.al. 1988) and with the eight-year temperature climatology above Fort Collins, CO (She et al., 2000). Since temperature and wind variability is often large (Fig. 6.1-Fig. 6.8), deviations from the mean are as important, if not more so, for research and study. These deviations occur on a variety of time and spatial scales. For this study, we concentrate on time scales of one hour or longer and vertical scales between 2 and 20 km. The data is processed with 1-hour and 2km resolution. Low summer sodium densities limit the region that can accurately be probed with this resolution to 85-100km. The entire 80-105km region can be probed using this resolution, with temperature and radial wind uncertainties (due to photon-counting statistics) of less than 3K and 5m/s for non-summer months (Figs.5.9 and5.11). Thus, winter data will be analyzed in terms of hour-to-hour variability as well as night-to-night variability while summer data will be analyzed only in terms of night-to-night variability. (i.e. integration over several hours is necessary in order to accurately measure summer temperatures and winds with the above-mentioned resolution and uncertainties). Hour-to-hour variability, at each altitude, can be quantified by the standard deviation of the hourly profiles (one-hour integration period) forming the data set. Night-to-

night variability can be quantified by the standard deviation of the nightly profiles (one-night integration period) forming the data set. These variations will be discussed in section 7.2.

Atmospheric stability was discussed in section 2.2 in the context of whether a perturbation would continue to propagate upward with increasing amplitude or become damped, depositing energy and momentum and altering the local atmosphere. This has important implications for atmospheric waves (gravity and planetary) and solar tides, which dominate the dynamic meteorology of the mesopause region. Section 7.3 discusses statistics of static and dynamic stability, derived from winter observation of temperature and winds. Winds and wind shears observed in this data set are larger than those predicted by models and comparable to those derived from four decades of rocket and chemical release observations (Larson, 2001). These shears were often large enough to cause regions of dynamic instability. Statistics of these strong winds and shears will be discussed in section 7.3 and compared with those compiled by Larson, whenever possible.

During the period May 22-June 12, 2002, the CSU lidar measured mesopause region temperatures, zonal, and meridional winds over four full diurnal cycles. These measurements were part of a 22-day campaign yielding 232 hours of useful data[1]. Harmonic analysis was performed on the measured temperature and winds and the resulting 12 and 24-hour amplitudes and phases were compared with those from the Global-Scale Wave Model (GWSM00) created by Hagan (1995). These results are presented in section 7.4.

7.1) Winter and Summer Seasonal Mean Temperatures and Winds

Seasonal mean temperature and winds were computed by integrating backscattered photons over one-hour (winter) and one-night (summer and winter) periods at each altitude and using eq. 6.2.3 to obtain hourly (winter) and nightly (summer and winter) averaged temperatures and wind profiles such as those presented in section

[1] Days and hour comprising the winter and summer data sets are tabulated in Appendix B.

6.4. Profiles used in sections 7.1 to 7.3 were smoothed with a 2km FWHM Hanning window, resulting in 2km vertical resolution. These profiles were then combined with those obtained from other nights (hours) to yield nightly averaged (hourly averaged) seasonal profiles of mean temperatures, winds, as well as standard deviations from the mean. These deviations will be referred to as night-to-night variability and hour-to-hour-variability. The altitude range was limited by the imposed requirement of <3K and <5 m/s photon-noise uncertainty in the temperature and radial wind profiles, respectively. This restricts the range of hourly profiles to 80-105km for non-summer months and 83-100km for summer months (Fig. 5.9 and 5.11). Nightly-averaged summer profiles typically range from 81-104km. For comparisons with climatology, only nightly-averaged profiles are presented in Fig. 7.1(a)-(c).

Winter and Summer Mean Temperatures:

Nightly-averaged winter and summer temperature profiles are compared with the eight-year mesopause temperature climatology measured by the CSU lidar between 1992-1999 (She et al., 2000) for February 4 and June 1. The results are shown in Fig. 7.1(a). The mean summer profile is similar to that of the corresponding climatology. Both reveal a summer mesopause (altitude of minimum temperature) at around 86km, followed by a steep positive lapse rate (dT/dz) from 87-105km. Mesopause temperatures are comparable (~180K) in both cases. Minor deviations of the summer mean from climatology represent the mean wave perturbations that exist in the present data. Comparing to the Fort Collins June 1st climatology, the TIME-GCM shows comparable temperatures throughout, except for a cooler mesopause (by ~10K), located at a lower altitude (~80km). The winter profiles show fewer similarities. The current winter profile exhibits larger temperature extremes at the top and bottom of the layer and possesses a much steeper negative lapse rate, particularly between 90-100km. As in the February 4th climatology, the winter mesopause occurs at 102km, although the current winter mesopause temperature is ~5K cooler. This difference is within one standard deviation of the mean.

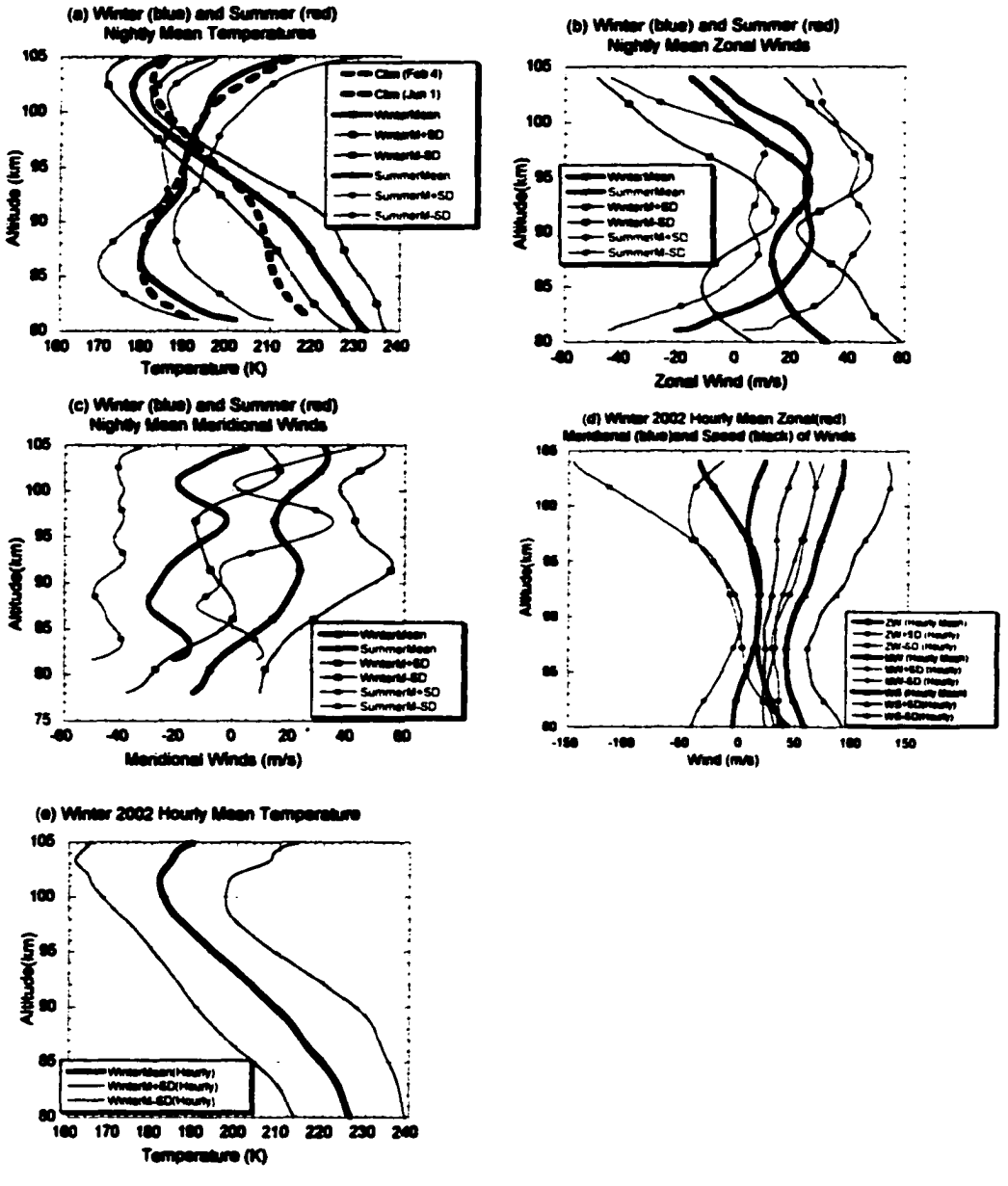

Figure 7.1 Winter and summer 2002 seasonal average (and standard deviations) temperature and winds above Fort Collins, CO, calculated from nightly averages (a)-(c) and from hourly averages (d)-(e). Temperatures (a) are compared with Feb 4 (green dashed) and June 1(black dashed) 8-year climatologies. In plots (a)-(c), winter temperatures and winds are denoted by blue-squares and summer by red-circles. Mean profiles are represented by thick lines and ± 1 std dev from mean by thin lines. In plot (d), hourly-mean seasonal zonal winds (red-circle), meridional winds (blue-square), and speeds (black-triangle) are plotted together.

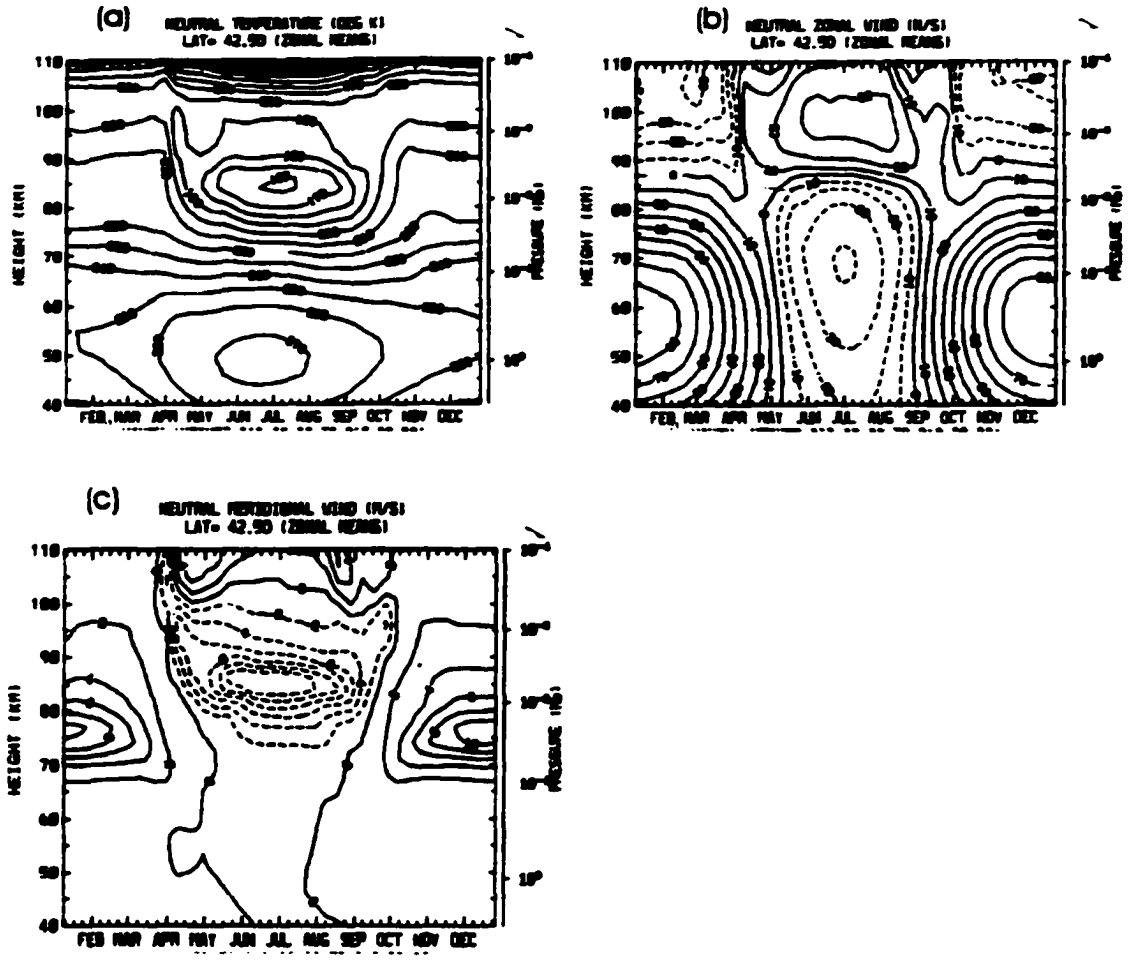

Figure 7.2 TIME-GCM temperature (a), zonal wind (b), and meridional wind (c) outputs for atmosphere above Fort Collins, CO. (Roble, 1999). Dashed lines indicate negative values.

Unlike the climatology, the current winter mean profile does not show a secondary temperature minimum at 85km. This could result from the masking effect of enhanced wave activity observed during the period. The colder mesopause and much warmer (by 12K) at 85 km reflects high wave activities during this winter period, as often is the case in winter months. No February model temperatures exist below 200K (Fig. 7.2(c)), as compared to the lidar-derived 180K mesopause temperature. The Fort Collins Feb. 4th temperature climatology is similar to that predicted by the TIME-GCM near 87 km. The model predicts a warmer mesopause temperature

(~200K), than those observed in climatology studies (~182K) and in the current winter data (~177K).

Winter and Summer Mean Zonal Winds:

For winter (summer), the TIME_GCM model predicts monotonically descreasing (increasing) winds, changing sign at ~87km and ranging from 30m/s (-30m/s) at 80km to -30m/s (30m/s) at 105km (Fig. 7.2(b)). Winter shears appear approximately uniform in the model. Lidar data exhibits larger summer shears below 85km and above 97km (Fig. 7.1(b)). Lidar summer winds change sign (to positive) at ~83km and both summer and winter winds change sign (to negative) near 100km. This feature is absent in the model output but is a common feature of the data obtained from four decades of chemical release measurements (Larson, 2001).

Winter and Summer Mean Meridional Wind:

The model predicts a small (<10m/s) flow from summer pole toward winter pole (i.e negative winds in summer and positive winds in winter), with magnitudes approaching zero near 100km (Fig. 7.2(c)). Observed winds are negative in summer and positive in winter for most altitudes, consistent with circulation from summer pole toward winter pole (Fig. 7.1(c)). The magnitudes of both summer and winter means are larger than those predicted by the model, although the differences are well within one standard deviation of the data.

Winter and Summer Mean Wind Speeds

Winter hourly mean wind speeds increase rapidly with height above 90km., reaching 90m/s at 103km (Fig. 7.1(d)). Rapid increase in wind speeds at 90km is consistent with chemical release data compiled by Larson (2001) but is not statistically significant, since the increase in mean wind speed with altitude is within one standard deviation of the mean. This increase is more likely a result of increased wind variability above 90km, as can be seen from Fig. 6.1(b)-(c) and the standard deviations shown in Fig. 7.1(d). Large wind variability is examined in section 7.2.

7.2) Temperature and Wind Deviations from the Mean

Large vertical oscillations present in the hourly temperature and horizontal wind profiles (Fig. 6.1-Fig. 6.8) suggests that mean values alone do not paint a true picture of thermal and dynamical mesopause region structure. Standard deviations from the mean are also necessary. This section examines these deviations. As mentioned in section 7.1, hourly variations for the entire 80-105km region cannot be accurately determined from the summer data. Only night-to-night deviations within this altitude range will be discussed for the summer data set. This inevitably results in the loss of some information. Both hour-to-hour and night-to-night deviations will be examined for the winter data.

Temperature Variability:

Hourly and nightly temperature variations from previous (1992-1999) CSU lidar data have not yet been systematically evaluated. Current year data shows night-to-night standard deviation of 4-10K for both the summer and winter profiles (Fig. 7.1(a)). These variations are smallest near 92km in summer and near 100km in winter. Hour-to-hour variations of up to ~23K are seen in the winter data (Fig. 7.1(e)).

Wind Variability

Summer nightly zonal wind variability is comparable to winter variability Fig. 7.1(b). Summer nightly meridional wind variability is considerably larger (40-50m/s) than winter variability at all altitudes Fig. 7.1(c). Hour-to-hour winter variations for both wind components and wind speed increase rapidly above 90km. Variations in hourly zonal winds are especially noticeable, increasing from 15m/s at 90km to 100m/s at 103km. (Fig. 7.1(d)). In order to examine the source of these variations, plots of both wind components and temperature are shown for the seven winter nights as a function of time at four different altitudes (Fig. 6.3 and Fig. 6.4) Oscillations with 12-hour periods are clearly evident in several of these profiles. The amplitudes of these oscillations increase with height. This evidence, when coupled with the periods, suggests the importance of tidal contributions. To further

investigate this, theoretical amplitudes and phases (hour of maximum amplitude) for the 12 and 24-hour February tides based on GSWM00 are given in table 7.1 for comparison. Temperature and both horizontal wind tidal components, in particular the 12-hour component, are predicted to be very large in February (see table 7.1).

Table 7.1 Theoretical 12-Hour (not in parenthesis) and 24-Hour (in parenthesis) Tidal Amplitudes and Phases for February (from Hagan, 1995).

Height (km)	Temp(T) Amp(K)	Temp(T) Phase(hr)	Zonal(U) Amp (m/s)	Zonal (U) Phase (hr)	Merid(U) Amp (m/s)	Merid(U) Phase(hr)
82.13	3.04 (2.58)	16.2 (9.8)	7.67(11.6)	11.1(14.9)	7.44(11.8)	8.2(9.4)
86.29	3.95(1.62)	15.6(6.5)	11.7(10.2)	10.5(11.8)	12.1 (9.96)	7.5 (7.1)
90.57	5.17(2.72)	14.7(1.6)	17.5 (10.4)	9.9(7.6)	18.0(7.67)	6.9 (2.9)
94.58	7.09(4.01)	13.7(23.2)	24.7 (14.4)	9.2(3.9)	24.9(10.1)	6.3(10.1)
98.74	11.0(4.89)	12.4(20.2)	33.7 (19.8)	8.4(0.7)	33.5(16.2)	5.5(6.5)
103.08	16.9(5.76)	10.9(15.9)	44.8(23.9)	7.3(21.2)	43.1(22.3)	4.4(3.2)

By constructing 12 and 24-hour period sine waves with crests at the times indicated (at a particular altitude) in table 7.1, it can be seen that these components are predicted to exhibit partial constructive interference, resulting in a wave bigger than each of the component waves. Inspection of Fig. 6.3 and Fig. 6.4 reveals that the phase of the meridional wind oscillation (at a particular altitude) often leads the

zonal wind phase by approximately 2 to 3 hours, in agreement with that of semi-diurnal tides (table 7.1). Furthermore, oscillations on a particular night usually show downward phase progression[2] (the crest appears at later times with decreasing altitude), implicating upward propagating buoyancy waves and tides in February (Table 7.1). It is thus apparent from Fig. 6.3, Fig. 6.4, and Table 7.1 that tides propagating upward with increasing amplitude are at least partially responsible for the hour-to-hour variability in the winter wind and temperature data (Fig. 7.1(e)-(f))

7.3) Statistics of Large Winter Winds and Regions of Instability

This section presents statistics of static and dynamic instability derived from winter temperature and wind measurements. Recall from section 2.3 that static (convective) instabilities result from a lapse rate (dT/dz) more negative than the adiabatic lapse rate (9.5 K /km in the mesopause region). This results in the square of the Brunt-Vaisala frequency (N^2) becoming negative. Note from eq.2.3.3 that static instability necessarily implies dynamic instability (Ri < 1/4). Dynamic instabilities can also result from a statically-stable atmosphere with values of N^2 greater than zero but small enough that large wind shears can force the local atmosphere into instability. This was often the case in the winter data set under investigation and will be discussed in section 7.3.1. Section 7.3.2 investigates statistical distributions of observed winter winds. Statistics of wind speed distributions agree well with chemical release data (Larson, 2001). Features of these large winds typically occur on vertical scales of 5-10km (Fig. 6.1) resulting in large vertical shears. Statistical distributions of these wind shears will be discussed in section 7.3.2. Knowledge of N^2 and the vertical shears of the horizontal wind components permits determination of the Richardson number via eq.2.3.3. These results are given in section 7.3.4. All temperature and wind profiles were analyzed with one-hour integration times and 2km vertical resolution (Hanning window FWHM=2km).

[2] This is more difficult to see at 85km, perhaps due to competing influences of similar magnitudes. The effect is more apparent at 91km, 97km, and 103km.

7.3.1) Static Stability of the Winter Mesopause Region above Fort Collins

From each hourly temperature profile T(z), the derivative dT/dz was computed and used in eq.2.3.2 to determine $N^2(z)$. Seventy hourly profiles of N^2 are superimposed in Fig. 7.3. It is seen from these profiles that N^2 is rarely less than zero (i.e the current winter mesopause was convectively stable during most hours measured). However, N^2 is often small enough that portions of the mesopause region can be forced into dynamic instability by strong wind shears. To assess how large these shears need be, eq.2.3.3 was invoked by setting Richardson number to 1/4 to relate the minimum wind shear to N^2:

$$\left(\left(\frac{dU}{dz}\right)^2+\left(\frac{dV}{dz}\right)^2\right)^{1/2}_{\min}=2N^2$$

For N^2 values of 1×10^{-4} sec^{-2} to 5×10^{-4} sec^{-2}, the minimum wind shear magnitude required to meet this necessary condition of dynamic instability is 20 to 100m/(s-km). N^2 values of 1×10^{-4} sec^{-2} to 2×10^{-4} sec^{-2} are often present in Fig. 7.3. Small values and observed wind shears presented in section 7.3.3 indicate the presence of regions of instability in many hourly profiles, as discussed in section 7.3.4.

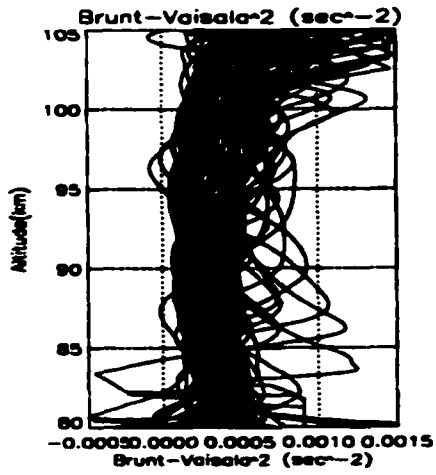

Figure 7.3 Winter 2002 hourly profiles of $N^2(z)$

7.3.2) Winter Wind Distributions

Distributions of large observed winter winds will be discussed in this section. Whenever possible, results will be compared with 350 wind profiles, derived from four decades of chemical release measurements. These profiles were carried out at latitudes ranging from 0 to 58° at several longitudes and under various geophysical conditions. (Larson, 2001). For each profile, a chemical vapor[3] trail was emitted from a falling rocket. This vapor, emitted in the 80-140km altitude range, was transported by the mean wind and the trajectory tracked by ground-based cameras. Dividing distance travelled by time for vapor at each altitude, wind profiles were derived. Distributions of maximum winter wind amplitudes derived from 70 hours of lidar observation are displayed in Fig 7.4 and Fig 7.5.

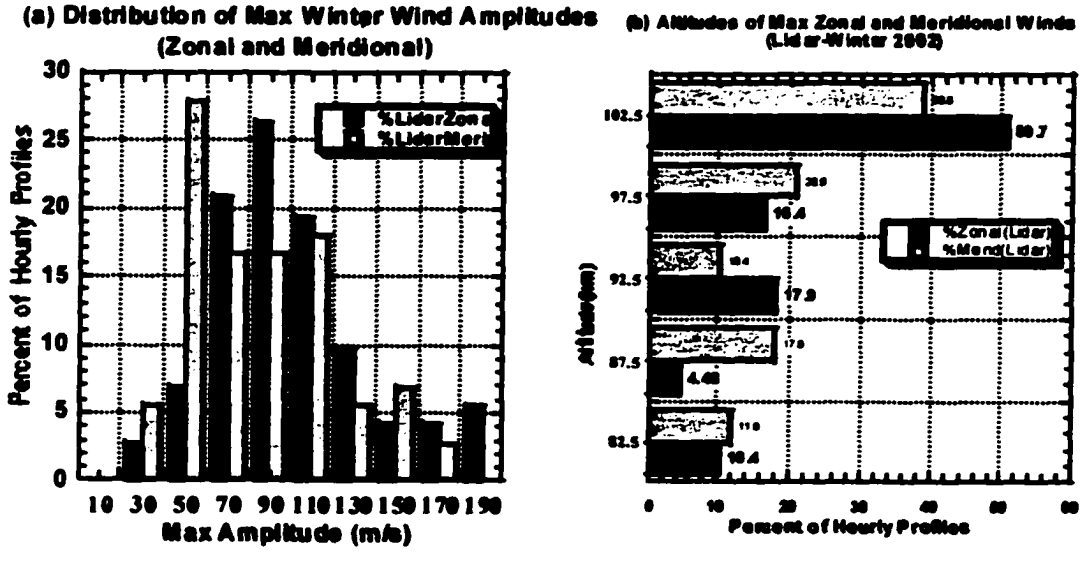

Figure 7.4 Distributions of (a) maximum winter 2002 zonal (black) and meridional (white cross-hatched) wind amplitudes and (b) altitudes of maximum zonal and meridional winds), measured by CSU lidar. The bin sizes are 20m/s (a) and 5km(b) centered at the numbers on horizontal axis (a) and vertical axis (b).

[3] Usually Trimethyl Aluminum (TMA), which reacts on contact with oxygen to produce chemiluminescence. This permits nighttime measurements. (Larson, 2001)

Amplitudes of at least 60m/s were measured in 90% of hourly zonal wind profiles and 43% of the profiles contained a zonal velocity of at least 100m/s (Fig 7.4(a)). Sixty-seven percent of the corresponding meridional wind profiles contained a velocity of at least 60m/s and 33% contained a velocity of at least 100m/s. Distributions of individual wind components are not given in Larson's study. Lidar-measured altitudes of maximum zonal wind were concentrated at higher altitudes, relative to those of meridional winds (Fig. 6.1(b)-(c) and Fig 7.4(b)). Maximum zonal wind amplitude occurred at altitudes greater than 95km in 67% of the profiles, as compared to 59% of the meridional wind profiles.

The distribution of maximum wind speeds for lidar and chemical release data are comparable (Fig 7.5(a)). The profiles might be expected to differ some, due to the fact that the distribution of amplitudes given for chemical release data covers the 95-115km altitude range (as compared to 80-105km for the lidar data). Both data sets contain wind speeds of at least 100m/s in roughly 60% of the profiles, with maximum wind speeds of 100-120m/s occurring most often. Some differences, such as the larger percentage of 150-200m/s speeds observed by lidar, may be due to lidar observations during a period of large wave activity, and could possibly become more comparable when long-term lidar wind statistics are compiled. Both data sets show maximum wind speeds occurring most often between 100-105km (Fig 7.5(b)-(c)), although the two data sets are not exactly on equal footing due to the fact that our data only ranges from 80-105km, while data compiled by Larson extends up to 140km. Both data sets show poor agreement with the Horizontal Wind Model (Hedin, 1991) shown in Fig 7.5(d). The model predicts lower wind speeds and a smaller tendency for the maximum wind speeds to occur in the 100-105km range.

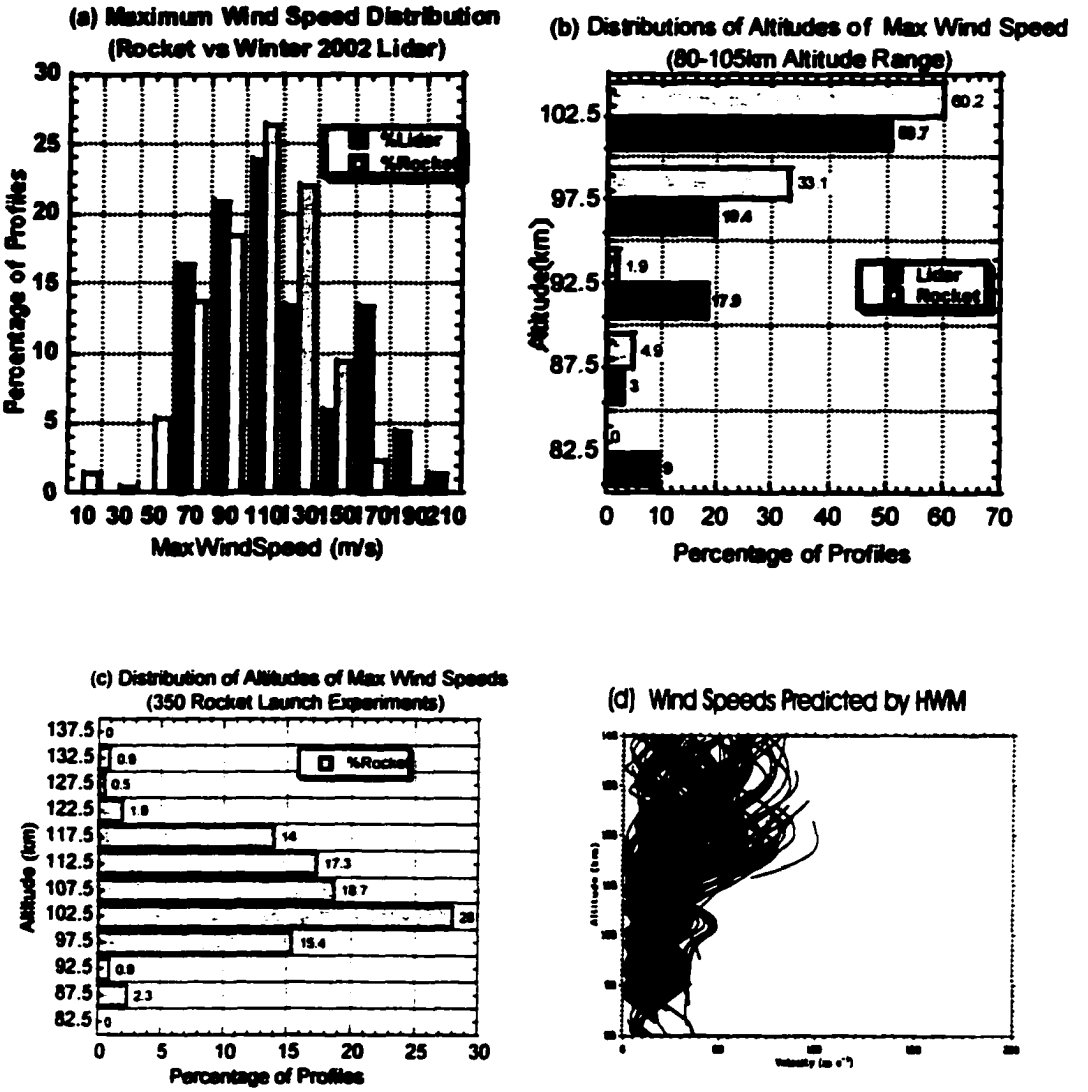

Figure 7.5 Distributions of observed maximum wind speeds (a) and altitudes of maximum wind speeds (b) for lidar(black) and chemical release (white cross-hatched) measurements. Since the chemical release data extends to 140km, the percentages in (c) were normalized to 100%[4] for the 80-105km range to facilitate comparisons with lidar-derived wind speeds (b). Wind speeds predicted by the Horizontal Wave Model (Hedin, 1991) for conditions corresponding to the measurements in (c) are given in (d). Bin sizes for these histograms are the same as those used in Fig 7.4.

[4] Normalizing the data in Fig. 7.5(c) simply involves neglecting all altitudes above 105km and rescaling the distribution below 105km by the factor (100/45.7) to add up to 100%. The rescaled distribution is compared in Fig. 7.5(b) with that derived from lidar data.

7.3.3) Wind Shear Profiles and Distributions

Hourly wind shear profiles for the 70 winter hours are superimposed in Fig. 7.6 and compared to corresponding chemical release shear profiles.

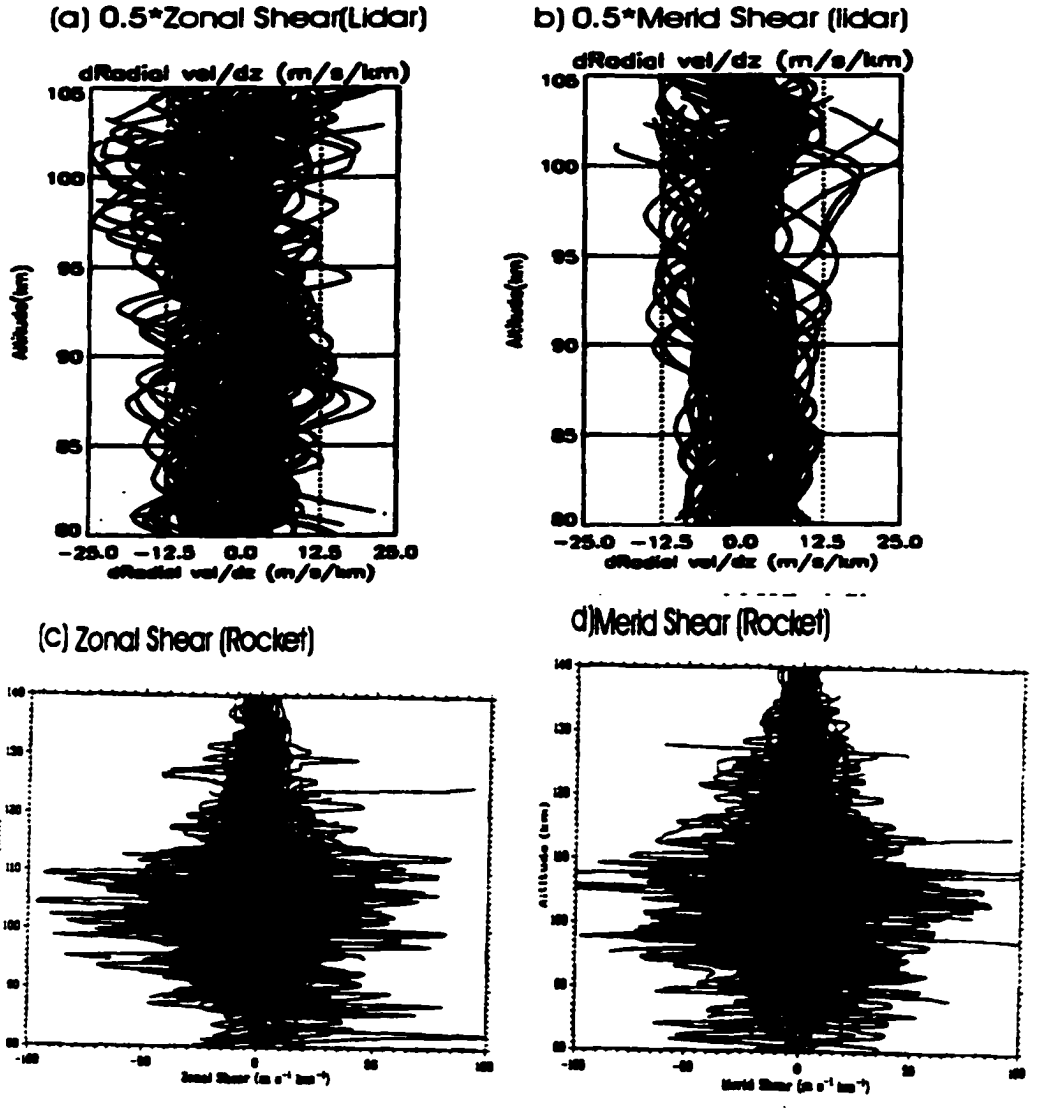

Figure 7.6 Composite profiles of lidar winter (a) and (b) and chemical release (c) and (d) wind shear measurements. Due to program output, plotted lidar shears need to be multiplied by two to obtain correct zonal and meridional shear magnitudes. Parts (c) and (d) reproduced from Larson (2001).

Wind shears in the chemical release data set increase with altitude for both wind components, with maximum shears most often occurring between 100-110km. Shears

in the chemical release data set are similar for both wind components. Lidar-derived zonal wind shears increase with altitude above ~97km (Fig. 7.6(a)). It is not easy to conclude from Fig. 7.6(b) that meridional wind shears also increase with altitude. Statistical distributions (Fig. 7.7(b)), however, reveal that maximum wind shears for both components occur most often above 100km.

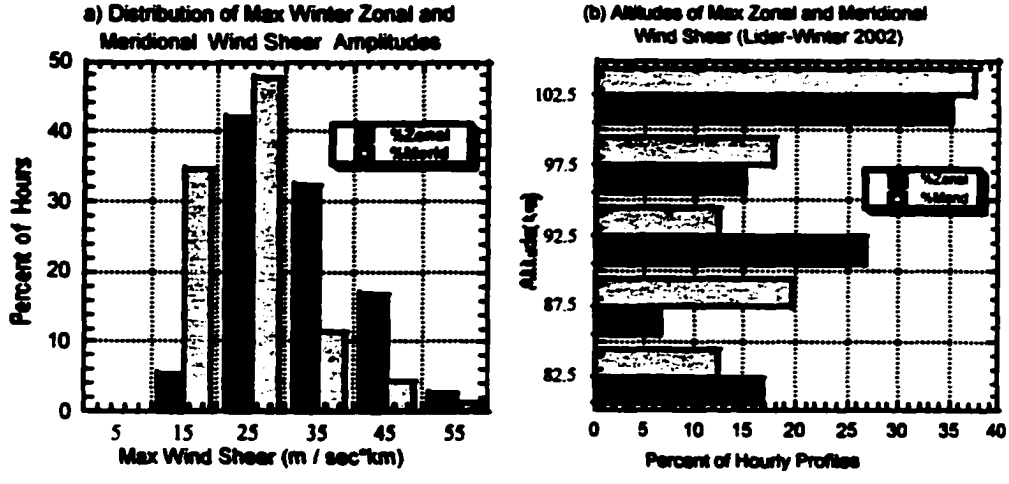

Figure 7.7 Distributions of maximum winter 2002 zonal (black) and meridional (white cross-hatched) wind shear amplitudes (a) and altitudes of maximum zonal and meridional wind shear (b) measured by CSU lidar. Bin sizes are 10m/(sec-km) (a) and 5km (b) centered at the numbers on horizontal axis (a) and vertical axis (b).

Distributions of lidar-measured wind shears are shown in Fig. 7.7. Twenty percent of the hourly profiles contained a zonal wind shear of at least 40 m/sec-km, as compared to only 6 % for the meridional wind shear profiles (Fig. 7.7(a)). Maximum wind shears of 20-30 m/ sec-km were most common in both zonal and meridional wind shear profiles. Inspection of Fig. 7.7(a) and Fig. 7.6(a)-(b) reveals that zonal wind shears were typically slightly larger than meridional wind shears. From the plots of N^2 (Fig. 7.3), it can be seen that measured wind shears are often sufficient to produce regions of instability in many hourly data profiles. Maximum wind shears (for both components) occurred between 100-105km, with comparable frequency.

This altitude range (Fig. 7.8) contained the most instances of dynamic instability, as will be discussed in Section 7.3.4.

7.3.4) Static and Dynamic Instability Distributions

Values for N^2, dU/dz, and dV/dz were derived from the hourly temperature and wind profiles and used in eq.2.3.3 to compute the Richardson number (Ri) as a function of altitude for each hour from 80-105km. This altitude range was then partitioned into five 5km bins. Instances of static (N^2<0) and dynamic (Ri<1/4) instability were identified and placed into one of the five altitude bins. Results are shown in Fig. 7.8. Since both lidar beams (east-pointing and north-pointing) measure temperature, the average value of $N^2(z)$ derived from the two channels was used in eq.2.3.3.

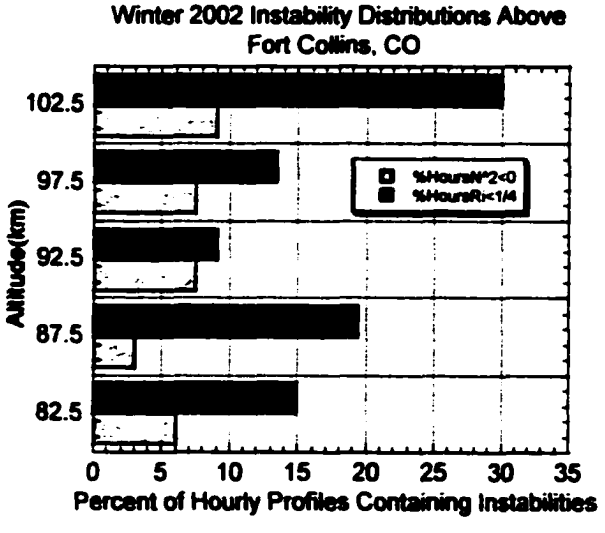

Figure 7.8

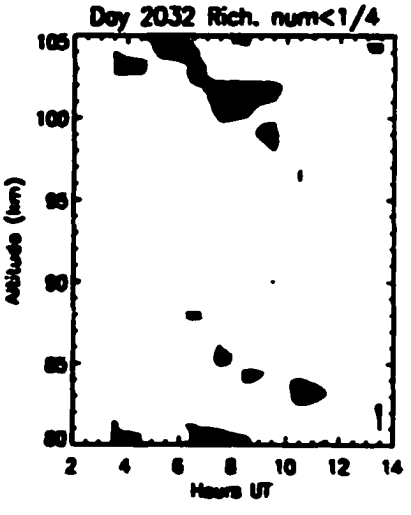

Figure 7.9

Figure 7.8 Percentage of winter 2002 hours that bins of size 5km centered at 82.5km +5km*j (j=0,1,2,3,4) above Fort Collins, CO contained regions of static ($N^2 < 0$, denoted by white cross-hatched bars) or dynamic (Ri<1/4, denoted by solid black bars) instability.

Figure 7.9 Regions of dynamic instability (black) measured during the night of Jan 31, 2002 (UT day 32 of the year 2002) above Fort Collins, CO

From Fig. 7.8, it is seen that instances of dynamic instability significantly outnumber instances of static instability, particularly in the 100-105km range, where instabilities were most often observed. This indicates that most observed instabilities were shear-induced and is consistent with Fig. 7.6 and Fig.7.7, which show that this is most often the region of largest shears. A plot of regions of instability occurring on January 31, 2002 is shown in Fig.7.9. For most other observed winter nights, instabilities were only observed for one hour. On this night, however, a region between 100-105km remained unstable (black regions denote dynamic instability) for six consecutive hours. Though it is not clear what mechanism was responsible for maintaining this long shear, this case deserves careful study to assess possible breaking of gravity waves.

7.4) Tidal Studies of the Mesopause Region Above Fort Collins, CO

As mentioned in chapter 2, tides are global oscillation with periods of one day or its sub-harmonics. Migrating solar tides must have a westward phase velocity equal to the earth's rotational velocity. These waves oscillate with the local sun time. Global oscillations which do not travel with the sun are referred to as non-migrating tides. At a single station, local variations with periods that are harmonics of diurnal oscillation may also be observed. From measurements made only at this station, it is not possible to determine whether the oscillations are global (migrating or non-migrating), local or a combination of the two. Characteristics of westward traveling solar tidal waves in the mesopause region, which can impact thermal and dynamical structure in the region, are of considerable interest and may be deduced from zonal averaged local time observations that cover full diurnal cycles. Short of providing complete global coverage, satellite observations provide partial local time global coverage. Ground-based local time observations at a fixed location provide complementary information, revealing properties of migrating and non-migrating tidal oscillations, which are essential for the testing of dynamics and chemistry imbedded in global models. Only recently has lidar observation of temperature tides in the mesopause region with full diurnal coverage been realized (States and Gardner. 2000; Chen et al., 2002). Since solar atmospheric tidal forcing affects both

temperature and wind fields, simultaneous observation of temperatures, zonal and meridional winds covering complete diurnal cycles is of obvious interest. The results below represent the first observations of this type. Measured oscillations with 24 and 12-hour periods may be compared to the output of the GSWM (Hagen et al., 1995) tidal model. Because the current version of the GSWM contains only migrating tidal forcing, our Fort Collins observations, which include the effect of non-migrating tidal forcing as well as local perturbations of the same periods, are not expected to agree with the GSWM completely. Nonetheless, the extent of agreement in tidal phases between model and observation will shed light on the importance of migrating tidal contributions at a mid-latitude site. Observations at a number of local sites with radar, lidar and other optical instrumentation provide local-time coverage of relevant atmospheric parameters and will complement the on-going TIMED (thermosphere, ionosphere, mesosphere energy and dynamics) mission, launched on December 7, 2001, providing global coverage between 60 and 180 km. Together, longitudinal and latitudinal dependence of tidal oscillations can be investigated and the relevance of non-migrating tidal sources, due to the global distribution of such important sources as water vapor, may be assessed. This will hopefully lead to a solid understanding of large-scale wave structures in this important transition region between magnetosphere above and earth's atmosphere below, where both solar and terrestrial influences affect dynamics and energy transport.

An extensive observational campaign was conducted with the Colorado State two-beam sodium lidar during the period May 22 - June12, 2002. Included in this data set are four periods (Fig. 6.5-Fig. 6.8) of continuous observation over full diurnal cycles (24hours), leading to a total of 232 hours of high quality lidar data. The data set was analyzed using a 7.5km Hanning window for daytime hours (3.7km for night-time hours) and one-hour integration period. The larger window is used to analyze summer daytime data due to low sodium density and the 20-25% transmission of the unique narrowband Faraday filter, which is necessary to reduce sky background. Derived temperature and wind profiles were then fit to a harmonic expansion

$$A(z) = A_0(z) + A_{24}(z)\cos(\frac{2\pi}{24hrs}(t - q_{24}(z))) + A_{12}(z)\cos(\frac{2\pi}{12hrs}(t - q_{12}(z))) + A_8(z)\cos(\frac{2\pi}{8hrs}(t - q_8(z))) + A_6(z)\cos(\frac{2\pi}{6hrs}(t - q_6(z))) \quad \text{eq.(7.4.1)}$$

where A's and q's are amplitudes and phases of the respective harmonic components for T, U, or V. The resulting amplitudes and phases are compared to the output of the Global Scale Wave Model (GSWM00) model. Since observed 6 and 8-hour components are typically much smaller, and due to the fact that GSWM00 only contains diurnal (24-hour) and semi-diurnal (12-hour) components, only observed diurnal and semi-diurnal oscillations are presented here for comparison. The GSWM00(Hagan, 1995) computes monthly diurnal and semi-diurnal amplitudes and tidal phases for altitudes 0 to 125km at 4 km intervals. At each altitude, results are given for latitudes spaced by 3°. Measured 12 and 24-hour amplitudes and phases are compared with those of GSWM00 (at 42°N) in this section. The results are shown in figures 7.10 to 7.12. Error-bars accounting for both measurement uncertainty and estimated geophysical variability, which should be included in the harmonic fits, are also plotted. The geophysical variability of a typical measurement was estimated as the standard deviation of observed values (temperatures and horizontal winds) at 91km (Na layer peak) and local midnight, where measurement uncertainty is minimum. By taking values at the same local time, contributions to the standard deviation from 12 and 24-hour oscillations are minimized, under the assumption that amplitudes and phases of these oscillations change little from night to night. The GSWM seems to indicate that these oscillations change on a time scale of months. Estimated uncertainties due to geophysical variability are 6K for temperature, 10m/s for zonal wind, and 15m/s for meridional wind. These uncertainties were then added in quadrature to instrumental uncertainties (due to photon noise) and propagated through the harmonic fit program to produce amplitude and phase uncertainties. Inspection of Fig. 7.10-7.12 (at 91km) reveals that estimated geophysical variability contributions to temperature and wind harmonic amplitude uncertainties are small (~1K and 1m/s) and that contributions to phase uncertainties are ~1 hour. By comparing these amounts to the total uncertainties at other altitudes,

one can deduce that geophysical variability dominates the error-bar between 84 and 98 km, while measurement uncertainty dictates the error-bar above and below this altitude range.

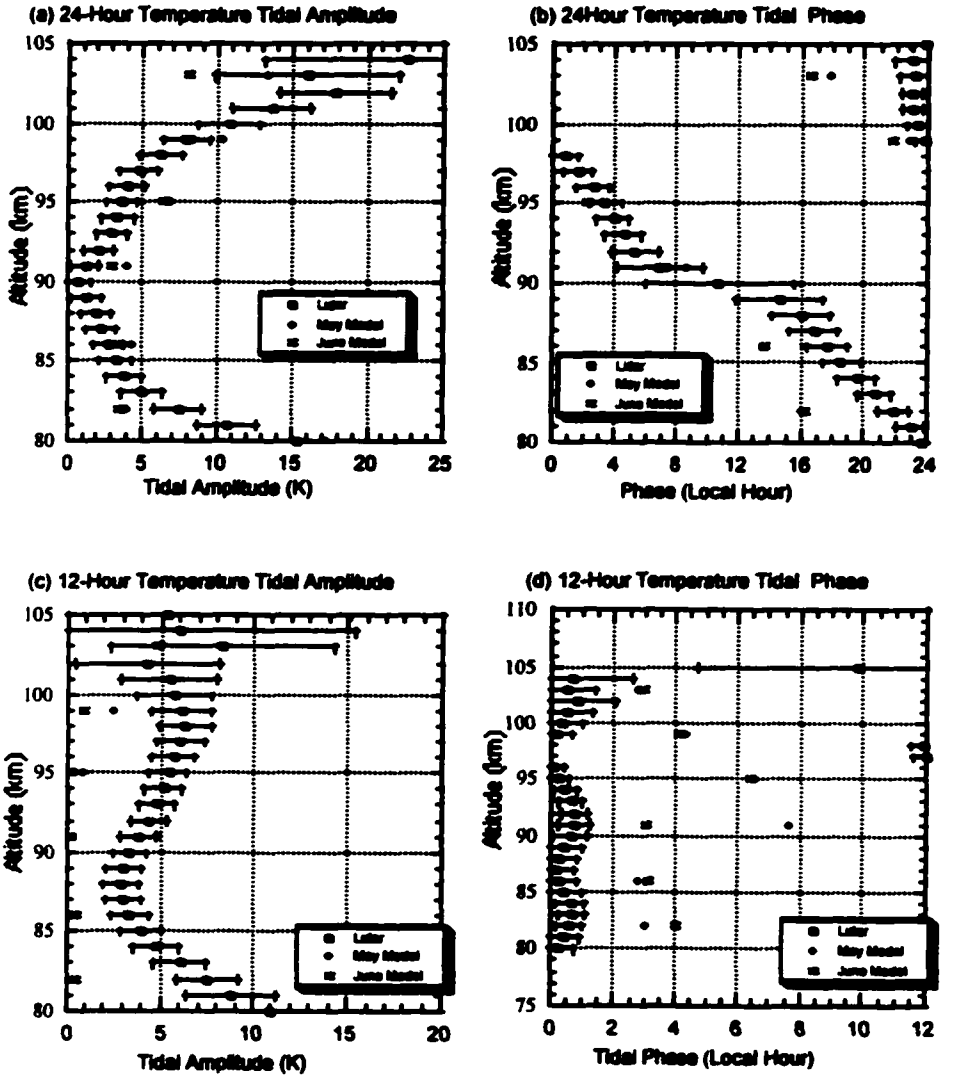

Figure 7.10 Diurnal (24hour) and semi-diurnal (12-hour) temperature amplitudes and phases for 232 hours of lidar data (circles with error bars), covering the period May 22-June 12, 2002. Comparisons are made with the GSWM (Hagan, 1995). Error bars due to photon noise and geophysical variability are included. May model values denoted by diamond and June model values by 'x's.

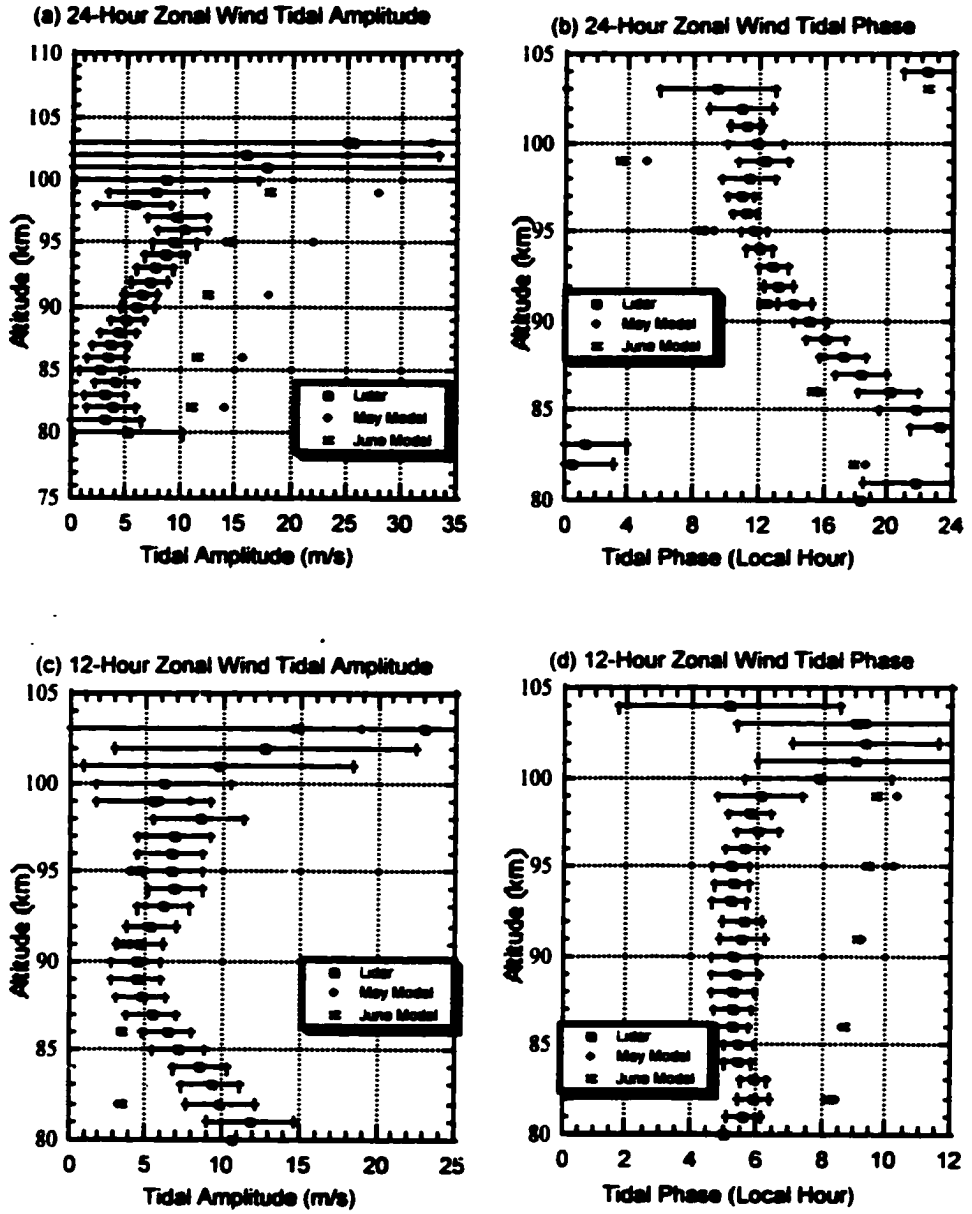

Figure 7.11 Diurnal (24hour) and semi-diurnal (12-hour) zonal wind amplitudes and phases for 232 hours of lidar data, covering the period May 22-June 12, 2002 (circles with error bars),. Comparisons are made with the GSWM (Hagan, 1995). Error bars due to photon noise and geophysical variability are included. May model values are denoted by diamonds and June model values by 'x' s.

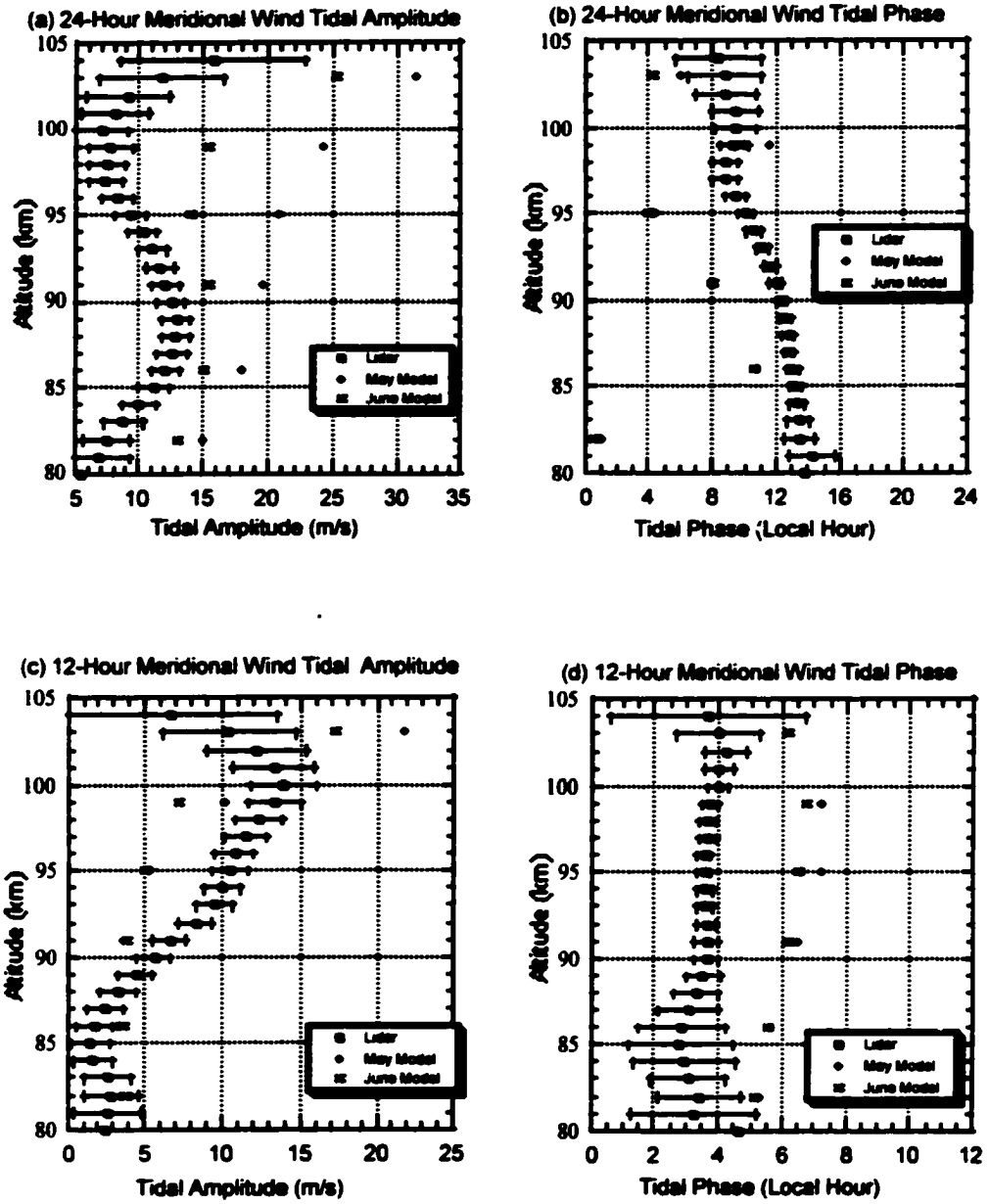

Figure 7.12 Diurnal (24hour) and semi-diurnal (12-hour) meridional wind amplitudes and phases for 232 hours of lidar data, covering the period May 22-June 12, 2002 (circles with error bars). Comparisons are made with the GSWM (Hagan, 1995). Error bars due to photon noise and geophysical variability are included. May model values are denoted by diamonds and June model values by 'x' s.

Amplitudes:

Lidar-derived diurnal temperature amplitudes showed good agreement with those of GSWM00, to within 3K up to 99km (Fig. 7.10(a)). Semi-diurnal temperature agreement was only to within 3-7K between 82-100km (Fig. 7.10(c)). Measured diurnal zonal wind amplitudes differed by a factor of 2-3 from those predicted by GSWM (Fig. 7.11(a)). Semi-diurnal zonal wind amplitude agreement was somewhat better, on the order of 1-3m/s from 86-100km (Fig. 7.11(c)). Measured meridional amplitudes (diurnal and semi-diurnal) differed by a factor of 1.5 to 2 with respect to the model (Fig. 7.12(a) and (c)). Diurnal meridional amplitudes showed better agreement with the June model than with the May model. Where differences existed, lidar-measured diurnal amplitudes were less than model outputs and measured semi-diurnal amplitudes were larger than those predicted by the model.

Phases:

In Chapter 2, the concept of vertical wavelength was introduced, mainly to develop an intuitive understanding of tides. In practice, vertical wavelengths are functions of altitude, since dT/dz (eq.2.4.5b) changes with altitude. This is analogous to the case of a light-wave traveling through a material possessing a varying refractive index. Equation 2.4.10 can be used along with the phase velocity (the slope of the plot of phase versus time, as measured between two points) to estimate λ_z at a given altitude but the concept of a single wavelength cannot be invoked. Accurate wavelength determination is somewhat limited by the 20-25km (from 82-100km during daylight and 80-105km at night) lidar vertical range and by the 7.4km daytime vertical smoothing of lidar data. Nevertheless, qualitative comparisons can be made.

Both lidar and theoretical diurnal phases exhibit downward phase progression with time for temperature and both wind components, consistent with upward energy propagation from a source at lower altitudes (section 2.4). Theoretical diurnal tidal wavelengths are generally 20-35km for May and June in the mesopause region at 42°

North. Local wavelengths computed from the measured 24-hour oscillation[5] agreed with theory to within 25% in most cases. Experimentally-derived phases in general exhibited a 2-5 hour offset from those calculated with the GSWM00. The general agreement in the shape of diurnal phases, especially for temperature and zonal wind component, suggests the importance of migrating tide contribution to the observed 24-hour oscillation. Several radar stations in the mid-latitudes are capable of measuring zonal and meridional winds, notably in nearby Platteville, in Illinois, near Boston, in Wales, in France, in Wuhan, China, and near Kyoto, Japan. Comparisons with their observed diurnal phases during the same observation periods and examination of their phase coherence would reveal the migrating tidal contribution and exhibit the longitude dependence of diurnal oscillations as well.

Semi-diurnal phases generally showed worse agreement between experiment and theory(Fig. 7.10(b)-7.12(b)). Both observed and modeled semi-diurnal phases show little time dependence, suggesting long vertical wavelengths (>100km). The difference between theory and experiment varied (depending on the pair of points used to calculate wavelength). Lidar-derived semi-diurnal wind phases exhibited less change with altitude than those computed by GSWM. In general one would expect the phase of the smaller summer semi-diurnal tide to be more difficult to measure than that of the larger diurnal tide. The small semi-diurnal amplitudes in the GSWM00 would make model determination of their phases difficult. Quantitative agreement in semi-diurnal phases is thus not expected.

[5] Vertical wavelengths at a given altitude were estimated by taking the slope of phase vs time between two points in Fig. 7.10-Fig.7.12 (b) and (d) and multiplying this by the oscillation period (eq.2.4.10).

Chapter 8-Conclusion

Continued hardware upgrades have permitted the Colorado State University (CSU) lidar to operate in two-beam mode, capable of simultaneously measuring temperature, zonal winds, meridional winds, and sodium density in the mesopause region (80-105km) above Fort Collins, CO. Lidar transmitter upgrades, which represent a portion of this thesis, include:

1) Improvement in the sodium D_2 Doppler-free spectrum (Chapter 4) to which the cw ring laser is locked, permitting more accurate frequency locking.

2) Improved mode-matching (Chapter 4) of the cw laser beam to the pulsed-dye amplifier (PDA).

3) Improved stability and sensitivity of the wind-bias correction instrument (Chapter 5) has been demonstrated. The instrument has consistently corrected radial wind-biases of -7m/s to +4m/s down to magnitudes of 1m/s or less, as determined by several nights of vertical wind measurements (Section 5.6).

The first two items above are believed to be contributing factors in the reduction of uncorrected radial wind bias from magnitudes of 10-15 m/s down to 1-3m/s. The small residual wind bias has resulted in the wind-bias instrument being used as a diagnostic tool (as opposed to a tool of necessity) during many data campaigns.

The unique capability of the Na fluorescence lidar to simultaneously measure temperature and both horizontal wind components permits real-time measurement of important atmospheric parameters such as Brunt-Vaisala frequency, wind shears, and Richardson number. From these three quantities, static and dynamic stability of the mesopause region can be assessed. This information, along with temperature and wind climatology above Fort Collins, CO, can be combined with other CEDAR data to provide valuable insight into the dynamics of the mesopause region, helping quantify the elusive gravity wave forcings required for General Circulation Models of the Atmosphere.

A total of 172 hours of nightly observation and four campaigns over full diurnal cycles from the two-beam configuration have been used for this study. The nightly results, composed of 70 observation hours in the period Jan 26-Feb 15 and 102 hours in the period May 22-June 12, were presented in sections 7.1-7.3. The two periods were referred to as summer and winter despite the fact that only data over partial seasons was presented. Large winter winds and shears and the resulting instabilities (in the Richardson sense) can be inferred from the data. These winds are larger than those predicted in models (Hedin, 1991; Roble, 1999) and are comparable to those observed during four decades of chemical release data (Larson, 2001). Hourly winter wind speeds and variations in both winter wind components increased rapidly above 90km. A majority of measured winter instabilities appear to result from large wind shears, as compared to convective instabilities. Both the recent study of Larsen (2001) based on four decades of sparse chemical release experiments and lidar data presented in this dissertaion point to the existence of dynamical instabilities, caused by high winds and high wind gradients, in an otherwise convectively stable mesopause region. The implications of this, thus far un-accounted for in exisiting models, may be intriguing. More data is necessary to determine if this is a regular feature of mesopause measurements above Fort Collins and elsewhere. Lower summer sodium density limits accurate hourly temperature and wind variation determinations over the entire 85-100km. Unless the receiver aperture (35 cm in diameter) of the CSU lidar is increased, accurate stability measurements over the entire 80-105km layer are only possible for non-summer months.

Much effort into improving the stability of the Faraday filters (Yuan) has resulted in temperature and wind measurements being extended to include daylight hours. During the period May 22-June 12, 2002, the CSU lidar measured mesopause region temperatures, zonal, and meridional winds over four full diurnal cycles, representing the first such simultaneous measurements over complete diurnal cycles. These measurements were part of a 22-day (232-hour) data-taking campaign. Harmonic analysis was performed on the resulting temperature and wind measurements and the resulting 12 and 24-hour amplitudes and phases were compared with those from the

Global-Scale Wave Model (GWSM00) created (1995) and upgraded by Hagan. These results were presented in section 7.4. Diurnal amplitudes and phases showed good agreement with the GSWM. Semi-diurnal amplitudes and phases were not in good agreement with the GSWM. The usefulness of these measurements covering full diurnal cycles will be greatly enhanced by continued monthly measurements and by comparisons with tides simultaneously measured by radar and optical instruments at other location and by the observation of TIMED satellite, when this data becomes available. The broad horizontal coverage of the satellite measurement, complemented by the excellent local-time vertical coverage of the lidar, can provide a great deal of information on the propagation characteristics of solar migrating and non-migrating tides. The GSWM is being upgraded at this moment to include regional heating sources such as water vapor that provides forcing for the non-migrating components. Continued lidar observations during summer months will be highly relevant in assessing the impact of global water vapor distribution on atmospheric tides. It is indeed exciting times for the investigation of solar-terrestrial relations and their impact, as coordinated global observations and ever expending numerical models converge (or clash) together.

In the tradition of departing CSU lidar group members, it is now my turn to make the transition from lidar researcher to lidar philosopher. In what direction would I steer the lidar ship, given new grant money and hard-working graduate students eager to make their imprint on the ever-expending universe of physics? One look at the lidar equation (6.1.1) begs the answer: MORE PHOTONS! Photon noise limits the altitude range over which accurate temperature and wind measurements can be performed with high temporal and spatial resolution. The purchase of a 1.8meter telescope, similar to that used by the CSU lidar located at the Alomar site in Norway, would increase the number of counted photons by a factor of 25, all other things being equal. This would increase the signal-to-noise (the principle source of uncertainty outside of the altitude range 85-98km for most measurements) by a factor of 5, enabling night and daytime temperature and winds to be accurately measured (<3K and 5m/s) at altitudes 80-105 km for all months, with 1-hour integration times

and 2km resolution. This would also permit integration times as low as five minutes for non-summer nights, enabling the determination of gravity wave parameters on a routine basis.

Appendix A: Lidar Calibration Spectroscopy-Experimental Procedure and Software Algorithm

This appendix details the basic experimental setup and software used to calibrate the CSU Na lidar. Cw beam spectroscopy is used to measure relative cw transmission spectra for the iodine cell (used to correct for instrument-induced wind bias) and for the Faraday filter (used for sky background reduction during daytime operation). Pulsed-beam spectroscopy is used to measure the pulsed dye amplifier (PDA) frequency lineshape. The experimental procedure and software processing are first discussed for cw spectroscopy and then for pulsed spectroscopy.

A.1) CW Spectroscopy

A.1.1) Experimental Procedure

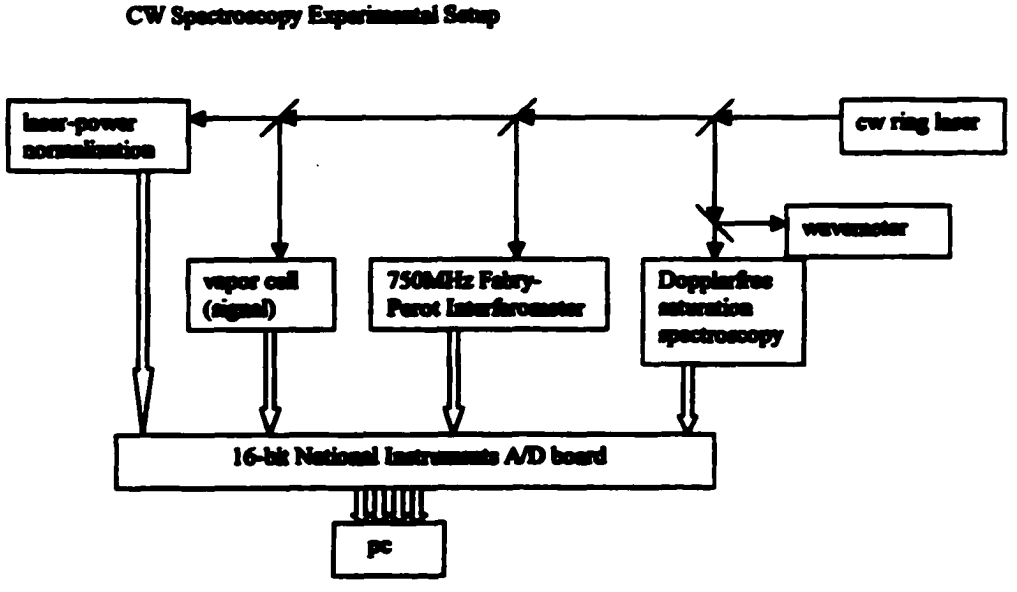

Fig. A.1 Experimental arrangement used for cw lidar spectroscopy. Thin black arrows denote light propagation and thick white arrows denote propagation of electrical signals.

The experimental setup for cw spectroscopy is shown in Fig.A.1. For simplicity, beam-steering mirrors, focusing optics, and photodiodes have been omitted. The single-mode cw ring dye laser's frequency is scanned by applying a ramp voltage (applied either externally by the Labview program which acquires the data or by applying a single-sweep ramp, internal to the ring laser) to a galvonometer-mounted Brewster plate, located near the output-coupling mirror of the ring laser. The Brewster plate is rotated through a small angle, changing the effective laser cavity length, and hence laser frequency, as the applied voltage ramp amplitude increases from -5V to +5V. A wavemeter is used to set the ring laser to the desired starting frequency. The cw ring dye laser is scanned roughly 5.5GHz for iodine scans and 14GHZ for Faraday filter scans. These ranges are chosen so as to a) include all of the important spectral features in the scan and b) assure that at least one Fabry-Perot interferometer fringe (separated at 750MHz) appears before and after any important spectral features (Fig.A.2). This assures better frequency scaling by the analysis software. The experimenter also aims to place the important spectral features in the middle of the scan, where the ring-laser scan is most linear. Each of the four data channel voltages (to be discussed below) are digitized by a National Instruments A/D board (AT-MIO-16XE-10), read by custom Labview software, and then stored in binary format to conserve disk space. A channel terminated with 50 ohms is used between each channel and read by the software to eliminate discharge of voltage into adjacent channels, a peculiarity of the multi-plexing scheme used by our A/D board (section 5.4). These 'dummy' channels are discarded by the analysis program (section A.2). Short scans (~3.5min) are chosen to minimize the effects of interferometer drift. These scans typically consist of around 20,000 data points (user-specified), which gives a resolution of roughly 250KHz for iodine scans (5.5GHz) and 700KHz for Faraday filter scans (14GHz).

Ring laser frequency scanning is only approximately linear, in the sense that the change in laser frequency is not exactly proportional to the change in applied voltage. Small non-linearities (0.5-2%) have been measured over a 5GHz scan width. Non-linearities are measured by determining the differences in the number of

datapoints (which is proportional to applied ramp voltage) between theoretically-determined (She and Yu, 1995) features in the sodium Doppler-free fluorescence spectrum. These nonlinearities are expected to be larger for the wider scans employed by the Faraday filter measurement but Dopplerfree features are absent over a large portion of this scan range, prohibiting the knowledge of scan non-linearities.

To account for the effect of laser scanning non-linearities, a confocal Burleigh Fabry-Perot interferometer (750MHz free-spectral range) is used as a high-resolution (finesse ~100, resulting in fringe FWHM ~7.5MHz) frequency marker. Although temperature-controlled, the interferometer does exhibit small (a few MHz for a scan duration of ~ 4min) frequency drifts on occasion. The effect of frequency drift is minimized by taking more (20-40), short-duration (<4min) scans. Sodium D_2 Dopplerfree fluorescence spectroscopy (section 4.2) is used to account for these small drifts and to provide an absolute frequency reference, which is necessary for both the measured iodine and Faraday filter transmission spectra.

In addition to the Fabry-Perot interferometer and Dopplerfree channels used for frequency-scaling, the A/D converter digitizes voltages from the vapor cell whose transmission spectrum is measured, and from an additional channel used to normalize vapor-cell transmission to incident laser power. These will be referred to as Signal and Intensity channels. Neutral-density filters are placed in the channel paths in order to achieve diode signal levels of 1-3V for the signal and intensity channels, 3-7V for the Fabry-Perot channel, and an input laser power of 120-160μW into the Dopplerfree cell. The currently-used cw amplified photodiodes (Thorlabs model 255) possess a small (5-20mV) , non-varying bias voltage, which is measured by the operator (before or after the measuring the transmission spectrum) and entered into the analysis program. The fast diodes used to measure the PDA lineshape possess larger and more variable bias voltages, which must be measured during each scan (section A.2).

A.1.2) CW Spectroscopy Software Algorithm

The cw spectroscopy software is contained in the program AnalyzeCwScan.vi. The software was written in National Instuments Labview G programming language. The output of a typical cw scan (iodine transimission in this case) is shown in Fig. A.2

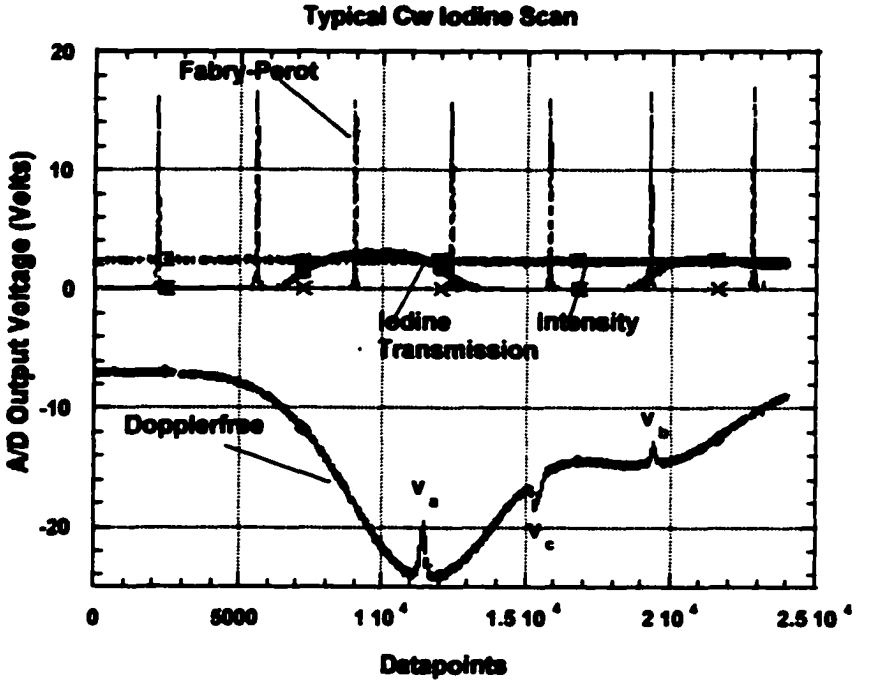

Figure A.2 Result from a typical cw iodine transmission scan (before software processing). The voltage outputs (from A/D board) are shown for the signal, intensity, Fabry-Perot interferometer and Dopplerfree channels.

The program performs three functions in converting the raw data for a given scan into a frequency-scaled, power-normalized output spectrum:

i) Preliminary diode-bias subtraction and smoothing of the data channels.

ii) Frequency-scaling the data channels.

iii) Final processing of the data. This involves interpolating the data channels, normalizing the spectrum to maximum transmission and writing the frequency-scaled data to a tab-delimited text file (readable by any spreadsheet program).

i) Preliminary Processing

The preliminary processing stage involves five steps:

1) Read the raw scan data, which is in binary format, and extract the four data channel columns into arrays (discarding the data from the four 'dummy channels').

2) Subtract the diode bias voltages (user-input) from the signal and intensity channels.

3) Take the absolute values of signal, intensity, and Fabry-Perot channels, accounting for the possible future use of negative-polarity photodiodes.

4) Divide the signal channel data by the intensity channel data, resulting in signal normalized to laser power.

5) Smooth the four data channels and the power-normalized signal by the user-defined number of smooth points(default=0), using a median filter.

ii) Frequency-Scaling the Data:

The software performs the following steps in creating a frequency scale for the measured cw spectrum

1) Find the locations of the 750MHz-spaced Fabry Perot interferometer fringe peaks.

2) Scale the frequency axis to these peaks, arbitrarily assigning zero frequency to the first data point. Points before the first Fabry-Perot peak and after the last peak are scaled by the average peak separation. For example, suppose that a scan has 10,000 data points and that Fabry-Perot peaks were found at data points 1000, 4000, and 7100. The average peak separation is (3000+3100) / 2 = 3050 data points. The first

data point is assigned the frequency v=0. Data points 1 to 1000 and 7100 to 10,000 are spaced by 750MHz/3050points=0.2459MHz / point. Data points 1000 to 4000 are spaced by 750MHz / 3000points=0.25MHz/point. Data points 4000 to 7100 are spaced by 750MHz/3100points=0.2419MHz/point.

3) Locate positions of the main Dopplerfree features (the D_{2a} peak, crossover resonance, and D_{2b} peak). The theoretical frequencies of these features, referenced to the D_{2a} peak, are located at 0, 839.2MHz, and 1719.4MHz, respectively.

4) Rescale the Fabry-Perot scaled data (obtained in step 2 above) to the theoretically-determined (She and Yu, 1995) separation of the three main Dopplerfree features. For example, suppose that the Fabry-Perot scaled array gives a separation of 843MHz between the D_{2a} peak and the crossover resonance. The entire frequency array is then rescaled by the factor 839.2MHz / 843MHz. This gives the correct spacing between the D_{2a} and crossover features. The program then outputs the rescaled separation between the D_{2b} and D_{2a} peaks. To verify that rescaling is correct over a larger frequency interval, the user should compare this value to the theoretically-determined separation of 1719.4MHz and discard the scan if the values differ by more than a few MHz.

The rescaling method basically assumes a uniform interferometer frequency drift over the course of the short (~3.5min) scan. Justification for this method lies in the fact that, after rescaling by the known $\nu_c - \nu_a = 839.2MHz$, the resulting separation $\nu_b - \nu_a$ is nearly always within 2-3MHz of the theoretical 1719.4 MHz value (this then forms a criteria by which bad scans can be discarded).

5) Set the zero of frequency to the user-defined set point. For iodine scans, the D_{2a} peak is assigned the frequency v=0. For Faraday filter scans, the D_{2a} peak is assigned the frequency v= -651.4MHz, which is the frequency of the D_{2a} peak relative to the centroid frequency of the sodium D_2 fluorescence spectrum.

iii) Final Processing

The final processing stage involves three steps:

1) Interpolate (cubic-spline method) the signal, intensity, and power-normalized signal arrays at the user-defined frequency limits and spacing. Default frequency spacing is 2MHz (in accordance with the program used to form the lidar calibration curve-Fig. 2.3). The frequency range is typically chosen as -1500MHz to 1000MHz for iodine scans and -4000MHz to 4000MHz for Faraday filter scans.

2) Normalize the power-normalized transmission spectrum to maximum transmission. This simply involves assigning the maximum transmission the value 1 and rescaling the spectrum by this amount.

3) Write the following columns to a tab-delimited text file (name is user-specified):

a) Frequency (GHz)

b) Signal (V)

c) Intensity (V). This is the power-normalization channel.

d) Signal / Intensity, normalized to maximum transmission.

e) Dopplerfree spectrum (V)

A.2) Pulsed-Dye Amplifier (PDA) Frequency Lineshape Measurement

A.2.1) Experimental Procedure

The PDA lineshape measurement entails scanning the single-mode cw ring dye laser over an approximately 4GHz range while directing the resulting PDA pulse of width ~ 120MHz through the stationary 750MHz Fabry-Perot interferometer. If the stationary Fabry-Perot peaks are thought of as thin spikes, then one PDA lineshape

emerges from the interferometer for each 750MHz that the ring laser is scanned through. The experimental setup is shown in Fig. A.3.

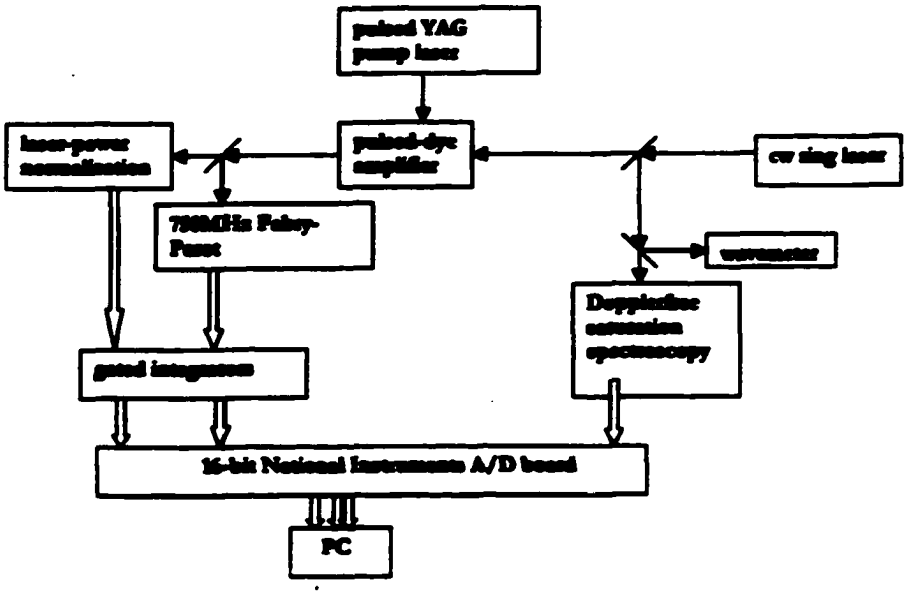

Fig. A.3 Experimental arrangement used for PDA lineshape measurement. Thin black arrows denote light propagation and thick white arrows denote propagation of electrical signals. For simplicity, turning mirrors, lenses, diffusers, and photodiodes are omitted.

The Dopplerfree spectrum is the only frequency scale used in this experiment. This is because the Fabry-Perot interferometer is used to trace out the asymmetric pulse lineshape (Fig. 5.2). In addition, considerable noise is introduced by the measurement itself, as pulses multiply-reflected from the interferometer mirrors partially superimpose. Another source of noise is movement of pulsed beam's center of energy, resulting from turbulence in the third PDA dye stage. This produces large fluctuations in the light focused onto the small fast photodiodes (section 5.4). The effect is reduced by inserting diffusers in front of each photodiode. This smoothes the intensity profiles incident on the diodes, reducing fluctuations. Due to these noise sources, it is virtually impossible to produce accurate frequency scaling from the interferometer in this experiment. The laser-power normalization channel serves the same purpose as in cw spectroscopy experiments: namely to normalize the signal (in this case the pulsed lineshape from the interferometer) to incident laser power. The

fast photodiode pulses from both channels are routed to gated integrators, which integrate the pulses to produce dc voltages proportional to the amplitude of the pulse (section 5.4). The integration times are typically 30-40ns for the signal channel and around 15ns for the power normalization channel. The difference is due to the fact that the multiply-reflected interferometer pulses introduce considerable time broadening of the Fabry-Perot output (roughly 60ns FWHM for the 7ns input pulse). This results in a somewhat noisy output from the integrators. As a consequence, the integrator outputs need to be averaged over three pulses (to improve signal-to-noise, resulting in a resolution of 1MHz) and software smoothing is necessary. The integrators are triggered by the Q-switch synchronization TTL pulse from the pulsed 50Hz YAG laser. This synchronization pulse arrives at the integrators approximately 100ns before the laser pulse. Scan durations are typically four minutes, producing data files of size 12000 data points (240seconds*50Hz). The user blocks the beam for the last few hundred data points of each file (Fig. A.4) so that the software can subtract the non-negligible pulsed-diode bias voltages. The integrator outputs are read by the PC and processed by Labview software (as described in section A.1.1). The inherent difficulties associated with this measurement would seem to imply that large calibration errors are possible from using the resulting PDA lineshape measurement. Surprisingly, routine measurements are repeatable to within 10% in both width and asymmetry (provided that a sufficient number of scans, usually at least 30, are taken to minimize the effects of random errors), contributing uncertainties of less than 0.5m/s to radial wind measurements (section 5.5). The unprocessed output of a typical scan is shown in Fig. A.4.

A.2.2) PDA Lineshape Software Algorithm:

The pulsed-spectroscopy software is contained in the Labview program AnalyzePulseLineshape.vi. Results from a typical PDA lineshape scan (before software processing) are shown in Fig. A4.

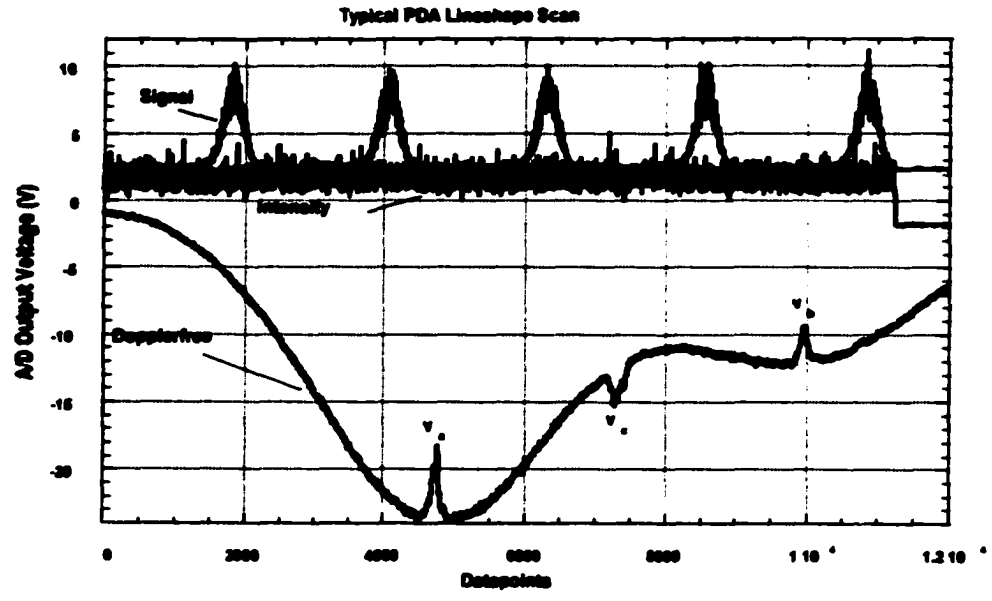

Figure A.4 Result from a typical PDA lineshape scan (before software processing). The beam was blocked at the end of the scan so that analysis software could later subtract the photodiode bias voltages. The voltage outputs (from A/D board) are shown for the signal, intensity, and Dopplerfree channels.

The program performs four functions in converting the raw data for a given scan into a frequency-scaled, power-normalized output spectrum:

i) Preliminary processing: This includes reading in the data channel arrays, subtracting fast photodiode bias voltages, and smoothing the data channels.

ii) Frequency-Scale the data channels.

iii) Extract and average the valid lineshapes (criteria discussed below). Interpolate each valid lineshape and combine them to obtain a file-averaged experimental lineshape.

iv) Final processing: This involves flipping the file-averagedexperimental lineshape (rationale to be discussed) to obtain the true lineshape. The data columns are then written to a tab-delimited text file.

i) Preliminary Processing:

The preliminary processing stage involves five steps:

1) Read in the raw scan data, which is in binary format. Extract the three data channel columns (signal, intensity, Dopplerfree) into arrays.

2) Subtract the diode bias voltages from the signal and intensity (power-normalization) channel arrays.

3) Take the absolute values of the signal and intensity channel arrays, accounting for the possible future use of negative-polarity photodiodes.

4) Normalize the signal channel to the power normalization channel, thus forming a new array. (signal / intensity)

5) Smooth (median filter) the three data channels and the power-normalized signal (formed in step 4) by the user-defined number of smooth points(default=0).

ii) Frequency-Scale the Scan Data

This stage involves three steps:

1) Produce a linear frequency scale: This step is necessary for PDA lineshape measurements because the Fabry-Perot interferometer is used for pulsed beam measurement and thus cannot be used for frequency scaling. Since the scans are linear to better than 2% over the short (GHz) scan width (section A.1.1) used in PDA lineshape measurements, a linear scale provides a rough frequency scale. This scale is later rescaled by the Dopplerfree features. The *i*th data point is assigned the frequency

$$\nu(i) = \frac{i}{\#datapoints} \cdot scanwidth(GHZ)$$

where i=0,1,2.....#datapoints-1

2) Find locations of the Dopplerfree features and set the zero of frequency to the D_{2a} peak. Setting the zero of frequency to the D_{2a} peak is not necessary but is done for convenience in using some of the functions initially written for the cw spectroscopy program.

3) Rescale the frequency scale to the Dopplerfree features. Because no Fabry-Perot interferometer is used for scaling in this experiment, this step is different from that used to rescale cw scans. It involves the following scaling process.

a) Frequencies between the D_{2a} peak and the crossover resonance are rescaled according to the known separation of 839.2MHz between the features.

b) Frequencies between the crossover resonance and the D_{2b} peak are rescaled according to the known separation of 880.2MHz between the features.

iii) Extract and average the valid lineshapes to obtain a file-averaged lineshape.

This stage involves three steps:

1) Find the pulse centroid locations for each lineshape.

2) Pulsed lineshapes with centroids located between the D_{2a} and D_{2b} Dopplerfree features are used in forming a file-averaged lineshape. This results in the use of two lineshapes per file (Fig.A.4) The lineshapes with centroids located outside of this interval are not used because their inclusion introduces the potential of frequency scaling errors (because no Dopplerfree features exist in these regions to correct for any scan non-linearities)

3) The centroid frequency of each extracted lineshape is set to zero. The extracted lineshapes are then interpolated with step size 2MHz from -300MHz to +300MHz and added point by point to yield a file-averaged lineshape, which is then normalized to unit area (Fig. 5.2). The interpolation range and steps are performed so that the

processed lineshape is consistent with the frequency range and step size used in the lidar calibration program.

iv) Final Processing:

This stage involves reflecting the file-averaged lineshape with respect to the frequency origin (center of 'mass') and then writing the following file-averaged columns to a tab-delimited text file:

1) Frequency column (-300MHz to 300MHz in 2MHz steps)

2) Signal channel data (pulsed lineshape not normalized to laser intensity)

3) Intensity channel data (power normalization channel)

4) Power-normalized PDA lineshape, normalized to unit area.

The experimental lineshape needs to be reflected about the origin in order to obtain the true PDA lineshape. The rationale for this is the following: The laser is scanned from lower frequency to higher frequency. Thus the first part of the ~120MHz pulse transmitted through the stationary Fabry-Perot interferometer fringe is the high-frequency part. This causes the high-frequency part of the pulse to be mapped by the interferometer into the low frequency part and vice versa. The pulsed lineshape therefore needs to be flipped in order to produce the true PDA lineshape, which is used in the lidar temperature and wind calibration curve (viz eq.3.2.2).

Appendix B - Dates and Hours of Lidar Observation

Tables listing the days and hours of winter (night only) and summer (day and night) lidar observation used in this dissertation are shown below. Each table contains four columns. The first column is the UT day. For example, the UT day 2034 is the 34th day of the year 2002. Starting and ending UT hours are given in column two. The hour is referenced by the center value. For example, the UT hour 3.5 represents the hour between 3.00 and 4.00. The fourth column contains the number of observation hours[1]. Due to clouds or hardware problems, data gaps sometimes exist.

Table B.1 Winter 2002 Observation Hours

UT Day	Start Hour	End Hour	Observation Hours
2027	4.50	12.50	7
2032	3.50	13.50	10
2034	3.50	13.50	11
2035	5.50	13.50	9
2037	4.50	13.50	10
2038	4.50	13.50	10
2046	2.50	13.50	12

[1] The number of summer hours is less than this (by ~15hours) for the east-pointing beam, due to excessive sky background present for that beam between 10am-noon. This background is sometimes large enough to potentially damage telescope fiber or pmt. As a result, this channel is blocked during these periods.

Table B2 Summer 2002 Observation Hours

UT Day	Start Hour	End Hour	Observation Hours
2142	3.50	23.50	21
2143	0.50	17.50	15
2145	2.50	23.50	17
2146	0.50	14.50	15
2150	4.50	22.50	19
2151	0.50	18.50	19
2152	4.50	11.50	8
2153	3.50	22.50	20
2157	23.50	23.50	1
2158	0.50	17.50	14
2159	5.50	23.50	18
2160	0.50	22.50	19
2161	3.50	22.50	19
2162	7.50	23.50	16
2163	0.50	10.50	11

REFERENCES

Andrews, D.G, J.R Holton, and C.B Leovy, Middle Atmospheric Dynamics, Academic Press, Inc. (1987).

Arimondo, E., M. Inguscio, and P. Violino, "Experimental Determination of the Hyperfine Structure in the Alkali Atoms", *Rev. Mod. Phys.*, 49, 31-75 (1977).

Chen, H., M. A. White, D. A. Krueger and C. Y. She, "Daytime Mesopause Temperature Measurements Using a Sodium-Vapor Dispersive Faraday Filter in Lidar Receiver", *Opt. Lett.*, 21, 1093-1095 (1996).

Chen H., C. Y. She and Eric Korevaar, "Na Vapor Dispersive Faraday Filter", *Opt. Lett.* 18, 1019-1021 (1993).

Chen, H., "A Sodium Fluorescence Lidar for Daytime Operation Using Dispersive Faraday Vapor Filter", PhD thesis, Colorado State University (1997).

Chen, S. S., Z. L. Hu, M. A. White, D. A. Krueger and C. Y. She, "Lidar Observations of Seasonal Variation of Diurnal Mean Temperature in the Mesopause Region over Fort Collins, CO (41°N, 105°W)", *J. Geophys. Res.* 105, 12,371-12,379 (2000).

Chen, S.S., "24 Hour Lidar Campaigns and Tidal Analysis", PhD thesis, Colorado State University (1999).

Dutton, J.A, Dynamics of Atmospheric Motion, Dover Publication, (1986).

Forbes, J. M., "Tidal and Planetarty Waves", in The Upper Mesosphere and Lower Thermosphere: A Review of Experiment and Theory, Ed. Johnson and Killeen, p.p. 67-87, *Geophys. Monogr.* 87, American Geophysical Union (1995).

Fricke K.H., U. von Zahn, "Mesopause Temperatures Derived from Probing the Hyperfine Structure of the D2 Resonance Line of Sodium by Lidar", *J. Atmos. Terr. Phys.*, 47, 499 (1985).

Fritts, D.C., "Gravity Wave-Tidal Interactions in the Middle Atmosphere: Observations and Theory", in The Upper Mesosphere and Lower Thermosphere: A Review of Experiment and Theory, Ed. Johnson and Killeen, p.p. 121-129, *Geophys. Monogr.* 87, American Geophysical Union (1995).

Fuller-Rowell, T.J., "The Dynamics of the Lower Atmosphere". in The Upper Mesosphere and Lower Thermosphere: A Review of Experiment and Theory, Ed. Johnson and Killeen, p.p. 23-36, *Geophys. Monogr.* 87, American Geophysical Union (1995).

Hagan M.E., J.M. Forbes, F.Vial, "On Modeling Migrating Solar Tides", *Geophys. Res. Lett.*, 22, 893-896 (1995).

Hedin A.E, M.A Biondi, R.G. Burnside, G. Hernandez , R.M Johnson, T.L Killeen, C. Mazaudier, J.W. Meriwether, J.E Salah, R.J. Sica, R.W Smith, N.W Spencer, V.B Wickwar, T.S. Virdi, "Revised Global Model of Thermosphere Winds Using Satellite and Ground-Based Observations", *Journal Geophys. Res*, 96, 7657-7688 (1991).

Holton, J.R., An Introduction to Dynamic Meteorology, Academic Press, (1972).

Houghton, J.T., The Physics of Atmospheres, Cambridge Unversity Press, (1986).

Larson M.F., "Winds and Shears in the Mesosphere and Lower Thermosphere: Results from Four Decades of Chemical Release Wind Measurements", Submitted to *Journal Geophys. Res*,. July 20, (2001).

Lieberman, R.S., "The Gradient Wind in the Mesosphere and Lower Thermosphere", *Earth Planets Space*, 51, 751-761 (1999).

Lindzen, R.S., "Turbulence and Stress Owing to Gravity Waves and Tidal Breakdown", *J.Geophys.Res*, 86, 9707-9714 (1981).

Roble, R.G., E.C. Ridley, A.D. Richmond, R.E. Dickinson, "A Coupled Thermosphere/Ionosphere General Circulation Model", *Geophys. Res. Lett*, 15, 1325-1328 (1988).

Roble, R.G, NCAR, private communications, (1999).

Schubert, W., Atmospheric Science Dept, Colorado State Univ, private communications, (2002).

She, C. Y., S. S. Chen, Z. L. Hu, J. Sherman, J. D. Vance, V. Vasoli, M. A. White, J. R. Yu, and D. A. Krueger, "Eight-year Climatology of Nocturnal Temperature and Sodium Density in the Mesopause Region (80 to 105 km) over Fort Collins, CO (41°N, 105°W)", *Geophys. Res. Lett.*, 27, 3289 - 3292 (2000).

She, C. Y., H. Latifi, J. R. Yu, R. J. Alvarez II, R. E. Bills, and C.S. Gardner, "Two-Frequency Lidar Technique for Mesospheric Na Temperature Measurements," *Geophys. Res. Lett.*17, 929-932 (1990).

She, C. Y., "Remote Measurement of Atmospheric Parameters: New Applications of Physics With Lasers," Invited Paper, *Contemp. Phys.* 31, 247-260 (1990).

She, C. Y., J. R. Yu, H. Latifi, and R. E. Bills, "High-Spectral-Resolution Fluorescence Lidar for Mesopheric Sodium Temperature Measurements," *Appl. Opt.* 31, 2095-2106 (1992).

She, C. Y., and J. R. Yu, "Doppler-Free Saturation Fluorescence Spectroscopy of Na Atoms for Atmospheric Applications", *Appl. Opt.*, 34, 1063-1075 (1995).

She, C. Y. and U. von Zahn, "The Concept of Two-Level Mesopause: Support through new Lidar Observation", *J. Geophys. Res.*, 103, 5855 - 5863 (1998).

She, C. Y., Songsheng Chen, B. P. Williams, Zhilin Hu, David A. Krueger and M. E. Hagan, "Tides in the Mesopause Region over Fort Collins, CO (41°N, 105°W) Based on Lidar Temperature Observations Covering Full Diurnal Cycles", JGR (in press).

Sherman, J.P., "Thermal Compensation of a Cw-Pumped Nd:YAG Laser", *Appl Opt*, Vol. 37, No. 33, 7789-7796 (1998).

Siegman, A.E., Lasers, University Science Books, (1986).

States, R. J. and C. S. Gardner, "Temperature Structure of the Mesopause Region (80-105km) at 40°N Latitude: 2. Diurnal Variations", *J. Atmos. Sci.*, 57, 78-92 (2000).

U.S. Standard Atmosphere, P.87, NOAA-S/T 76-1562, U.S. Government Printing Office

Waltersheid, R.L., "Gravity Wave Mean State Interactions in the Upper Mesosphere and Lower Thermosphere", in The Upper Mesosphere and Lower Thermosphere: A Review of Experiment and Theory, Ed. Johnson and Killeen, p.p. 133-143, *Geophys. Monogr.* 87, American Geophysical Union (1995).

White, M.A., "A Frequency-Agile Lidar for the Measurement of Temperature and Velocity in the Mesopause Region", PhD thesis, Colorado State University (1999).

Williams, B. P., C. Y. She, and R. G. Roble, "Seasonal Climatology of the Nighttime Tidal Perturbation of Temperature in the Midlatitude Mesopause Region", *Geophys. Res. Lett.*, 25, 3301 - 3304 (1998).

Yariv, A., Quantum Electronics, John Wiley and Sons, (1989).

Yu, J.R., "A Sodium Wind/Temperature Lidar and Observed Mesopause Thermal Structure over Fort Collins, CO", PhD thesis, Colorado State University (1994).